Deep 1.1 mm-wavelength imaging of the GOODS-S field by AzTEC/ASTE – II. Redshift distribution and nature of the submillimetre galaxy population

Min S. Yun,[1]★ K. S. Scott,[2] Yicheng Guo,[1] I. Aretxaga,[3] M. Giavalisco,[1]
J. E. Austermann,[4] P. Capak,[5] Yuxi Chen,[1] H. Ezawa,[6] B. Hatsukade,[7] D. H. Hughes,[3]
D. Iono,[8] S. Johnson,[1] R. Kawabe,[8] K. Kohno,[9] J. Lowenthal,[10] N. Miller,[11]
G. Morrison,[12,13] T. Oshima,[8] T. A. Perera,[14] M. Salvato,[15] J. Silverman,[16] Y. Tamura,[9]
C. C. Williams[1] and G. W. Wilson[1]

[1]*Department of Astronomy, University of Massachusetts, Amherst, MA 01003, USA*
[2]*Department of Physics & Astronomy, University of Pennsylvania, 209 South 33rd Street, Philadelphia, PA 19104, USA*
[3]*Instituto Nacional de Astrofísica, Óptica y Electrónica, Tonantzintla, Puebla 72000, Mexico*
[4]*Center for Astrophysics and Space Astronomy, University of Colorado, Boulder, CO 80309, USA*
[5]*Spitzer Science Center, 314-6 California Institute of Technology, 1200 East California Boulevard, Pasadena, CA 91125, USA*
[6]*ALMA Project Office, National Astronomical Observatory of Japan, 2-21-1 Osawa, Mitaka, Tokyo 181-8588, Japan*
[7]*Department of Astronomy, Kyoto University, Kyoto 606-8502, Japan*
[8]*Nobeyama Radio Observatory, National Astronomical Observatory of Japan, Minamimaki, Minamisaku, Nagano 384-1305, Japan*
[9]*Institute of Astronomy, University of Tokyo, 2-21-1 Osawa, Mitaka, Tokyo 181-0015, Japan*
[10]*Smith College, Northampton, MA 01063, USA*
[11]*Department of Astronomy, University of Maryland, College Park, MD 20742, USA*
[12]*Institute for Astronomy, University of Hawaii, Manoa, HI 96822, USA*
[13]*Canada–France–Hawaii Telescope Corp., Kamuela, HI 96743, USA*
[14]*Department of Physics, Illinois Wesleyan University, Bloomington, IL 61701, USA*
[15]*Max-Planck Institute for Plasma Physics & Cluster of Excellence, Boltzmann Strasse 2, 85748 Garching, Germany*
[16]*Institute for the Physics and Mathematics of the Universe (IPMU), University of Tokyo, Kashiwa 277-8582, Japan*

ABSTRACT

We report the results of the counterpart identification and a detailed analysis of the physical properties of the 48 sources discovered in our deep 1.1-mm wavelength imaging survey of the Great Observatories Origins Deep Survey-South (GOODS-S) field using the AzTEC instrument on the Atacama Submillimeter Telescope Experiment. One or more robust or tentative counterpart candidate is found for 27 and 14 AzTEC sources, respectively, by employing deep radio continuum, *Spitzer*/Multiband Imaging Photometer for *Spitzer* and Infrared Array Camera, and Large APEX Bolometer Camera 870 μm data. Five of the sources (10 per cent) have two robust counterparts each, supporting the idea that these galaxies are strongly clustered and/or heavily confused. Photometric redshifts and star formation rates (SFRs) are derived by analysing ultraviolet(UV)-to-optical and infrared(IR)-to-radio spectral energy distributions (SEDs). The median redshift of $z_{med} \sim 2.6$ is similar to other earlier estimates, but we show that 80 per cent of the AzTEC–GOODS sources are at $z \geq 2$, with a significant high-redshift tail (20 per cent at $z \geq 3.3$). Rest-frame UV and optical properties of AzTEC sources are extremely diverse, spanning 10 mag in the *i*- and *K*-band photometry (a factor of 10^4 in flux density) with median values of $i = 25.3$ and $K = 22.6$ and a broad range of red colour ($i - K = 0$–6) with an average value of $i - K \approx 3$. These AzTEC sources are some of the most

★E-mail: myun@astro.umass.edu

luminous galaxies in the rest-frame optical bands at $z \geq 2$, with inferred stellar masses $M_* = (1–30) \times 10^{10} \, \mathrm{M_\odot}$ and UV-derived SFRs of $\mathrm{SFR_{UV}} \gtrsim 10^{1-3} \, \mathrm{M_\odot \, yr^{-1}}$. The IR-derived SFR, $200–2000 \, \mathrm{M_\odot \, yr^{-1}}$, is independent of z or M_*. The resulting specific star formation rates, $\mathrm{SSFR} \approx 1–100 \, \mathrm{Gyr^{-1}}$, are 10–100 times higher than similar mass galaxies at $z = 0$, and they extend the previously observed rapid rise in the SSFR with redshift to $z = 2–5$. These galaxies have a SFR high enough to have built up their *entire* stellar mass within their Hubble time. We find only marginal evidence for an active galactic nucleus (AGN) contribution to the near-IR and mid-IR SEDs, even among the X-ray detected sources, and the derived M_* and SFR show little dependence on the presence of an X-ray bright AGN.

Key words: Galaxy: evolution – galaxies: high-redshift – galaxies: starburst – infrared: galaxies.

1 INTRODUCTION

Early studies of the far-infrared (FIR) cosmic background indicated that up to half of the cosmic energy density is generated by dusty starbursts and active galactic nuclei (AGN; Fixsen et al. 1998; Pei, Fall & Hauser 1999). Deep, wide field surveys at 850 µm (Smail, Ivison & Blain 1997; Barger et al. 1998; Hughes et al. 1998; Eales et al. 1999, 2000; Cowie, Barger & Kneib 2002; Scott et al. 2002; Serjeant et al. 2003; Webb et al. 2003a; Wang, Cowie & Barger 2004; Coppin et al. 2006) with the Submillimeter Common-User Bolometric Array (SCUBA; Holland et al. 1999) on the James Clerk Maxwell Telescope (JCMT), and later surveys at millimetre wavelengths (Borys et al. 2003; Greve et al. 2004, 2008; Laurent et al. 2005; Bertoldi et al. 2007; Perera et al. 2008; Scott et al. 2008, 2010, hereafter Paper I; Austermann et al. 2010), revealed that this IR background is resolved into a large population of discrete individual sources.

Identifying and understanding the nature of these discrete FIR sources ('submillimetre galaxies' or SMGs) has proven to be challenging because of the low angular resolution of these instruments and the faintness of counterparts in the rest-frame optical and ultraviolet (UV) bands (see review by Blain et al. 2002). Utilizing subarcsec astrometry of interferometric radio continuum data and sensitive spectroscopy using the Keck telescopes, Chapman et al. (2005) reported spectroscopic redshifts of 73 SMGs culled from earlier SCUBA surveys and concluded that they are massive, young objects seen during their formation epoch, with very high star formation rates (SFRs) at $z > 1$. Deep 24 µm band imaging using the Multiband Imaging Photometer for *Spitzer* (MIPS; Rieke et al. 2004) on the *Spitzer Space Telescope* and follow-up spectroscopy using the Infrared Spectrograph (IRS; Houck et al. 2004) have also provided useful insights on the nature and redshifts of additional SMGs (Lutz et al. 2005; Menéndez-Delmestre et al. 2007, 2009; Valiante et al. 2007; Pope et al. 2008a; Huang et al. 2009). However, the use of high resolution radio continuum and MIPS 24 µm images for the counterpart identification suffers from a well-known systematic bias against high-redshift ($z \gtrsim 3$) sources. Indeed, a large fraction of the counterpart sources identified using direct interferometric imaging in the mm/submm wavelengths are shown to be extremely faint in nearly all other wavelength bands ($r > 26$, $K > 24$) *with little or no radio or MIPS 24 µm emission* (Iono et al. 2006; Wang et al. 2007b; Younger et al. 2007, 2009), and high-redshift SMGs may have been missed or misidentified with a foreground source in the earlier studies.

Obtaining a more complete understanding of the SMG population requires a study of a larger, more uniform sample identified utilizing the deepest available multiwavelength complementary data and a robust counterpart identification method that is less prone to a redshift bias. In this paper we present the identification of the 48 AzTEC 1.1 mm sources found in the deepest survey at mm wavelengths ever carried out in the Great Observatories Origins Deep Survey-South (GOODS-S) field by Paper I. Several different identification methods are employed simultaneously to complement and to calibrate each other. A thorough analysis of the counterpart properties and redshift distribution is also carried out as the GOODS-S field represents one of the most widely studied regions of sky with some of the deepest multiwavelength data: X-ray data from *Chandra* (Luo et al. 2008; Johnson et al. 2011; Xue et al. 2011), optical to near-IR (NIR) photometry from the *Hubble Space Telescope* (*HST*; Giavalisco et al. 2004), *Spitzer* Infrared Array Camera (IRAC; Dickinson et al., in preparation) and MIPS (Chary et al., in preparation) imaging in the mid-IR, submm imaging at 250–500 µm with the Balloon-borne Large Aperture Submillimeter Telescope (BLAST; Devlin et al. 2009) and 1.4 GHz interferometric imaging with the Very Large Array (VLA; Kellermann et al. 2008; Miller et al. 2008). Extensive spectroscopy of optical sources in this field is also available (Le Fevre et al. 2004; Szokoly et al. 2004; Mignoli et al. 2005; Vanzella et al. 2005, 2006, 2008; Norris et al. 2006; Kriek et al. 2008; Popesso et al. 2009; Treister et al. 2009; Wuyts et al. 2009; Balestra et al. 2010; Silverman et al. 2010; Casey et al. 2011). Including the AzTEC GOODS-North field sources (Perera et al. 2008; Chapin et al. 2009), our combined AzTEC–GOODS sample includes ~80 SMGs identified using a uniform set of criteria and the deepest multiwavelength data available and offers the best opportunity yet to examine the nature of the SMGs as a population and to verify the conclusions of earlier studies of mostly smaller and often radio-selected samples (Lilly et al. 1999; Fox et al. 2002; Ivison et al. 2002, 2007; Webb et al. 2003b; Borys et al. 2004; Chapman et al. 2005; Clements et al. 2008).

2 COUNTERPART IDENTIFICATION

Here we describe the methods of identifying multiwavelength counterparts to the 48 AzTEC GOODS-S (AzTEC/GS hereafter) sources reported by Paper I. We adopt the updated AzTEC source positions and photometry derived using the improved point source kernel by Downes et al. (2011). Our counterpart identification relies primarily on three observed multiwavelength properties: (1) high-resolution radio continuum, (2) *Spitzer* MIPS 24 µm photometry and (3) red colours in the *Spitzer* IRAC bands. A robust counterpart is identified using a combination of these criteria for most AzTEC sources, and proposed identifications and multiwavelength photometry for each of the AzTEC 1.1 mm sources are summarized in Tables 1 and 2. A more detailed discussion of the individual identification and

Table 1. Radio and *Spitzer* identifications of AzTEC sources (procedure described in Section 2). The counterpart search radius R_S and the likelihood P values are described in detail in the text (Section 2), and robust counterparts are emphasized in boldface. Spectroscopic redshifts are given in the column labelled z_{spec} (references for these measurements are given in Appendix A).

AzTEC ID	R_S (arcsec)	Radio coordinate (J2000)	Dist. (arcsec)	*Spitzer* coordinate (J2000)	Dist. (arcsec)	$P_{1.4}$	$P_{24\mu m}$	P_{colour}	[3.6] − [4.5] (mag)	z_{spec}
GS1a	4.7	**J033211.37-275212.1**	4.8	J033211.36-275213.0	4.0	**0.045**	0.161	0.133	+0.37	...
GS2.1a	4.5	**J033219.06-275214.6**	0.8	**J033219.05-275214.3**	0.7	**0.001**	**0.006**	**0.005**	+0.38	...
GS2.1b		**J033219.14-275218.1**	3.9	...	...	**0.030**	...	...	...	...
GS2.1c		...	...	J033218.75-275212.7	3.9	...	0.154	...	−0.32	0.644
GS2.2a	8.7	...	...	J033216.62-275243.3	4.6	...	0.212	...	−0.23	1.046
GS2.2b		...	...	J033216.52-275246.5	7.4	...	0.457	0.390	+0.26	...
GS2.2c		...	...	J033216.75-275249.5	8.0	...	...	0.439	+0.10	...
GS3a	5.9	**J033247.99-275416.4**	4.8	J033247.96-275416.3	4.6	**0.045**[a]	0.211	0.174	+0.37	...
GS3b		...	...	J033247.70-275423.5	3.8	...	...	0.123	+0.14	...
GS4a	6.5	**J033248.97-274252.0**	3.2	J033248.96-274251.6	2.8	**0.021**[a]	...	0.070	+0.28	...
GS5a[d]	7.1	J033151.11-274437.5	6.4	J033151.08-274437.0	6.5	0.075	0.233[b]	0.274[c]	+0.23	**1.599**
GS5b		J033152.81-274430.3	17.4	J033152.80-274429.6	17.5	0.438	0.850[b]	0.903[c]	+0.43	...
GS6a[d]	7.5	J033225.27-275230.6	12.4	J033225.25-275230.2	12.2	0.268[a]	0.809	0.737	+0.45	...
GS6b		...	...	**J033225.76-275220.0**	0.4	...	**0.002**	...	−0.23	**1.102**
GS7a[d]	8.7	J033213.84-275600.2	8.4	J033213.85-275559.9	8.7	0.126	0.366[b]	0.439[c]	+0.46	**2.676**
GS7b		...	...	J033213.31-275611.5	4.9	...	0.151[b]	0.168[c]	+0.04	...
GS8a	8.7	**J033204.90-274647.4**	4.4	J033204.87-274647.3	4.5	**0.038**	0.203	0.168	+0.33	**2.252**
GS8b		...	...	J033205.35-274644.0	2.9	...	0.089	0.072	+0.17	...
GS9a	8.7	J033303.02-275146.5	6.2	J033302.99-275146.2	5.9	0.070	0.140[b]	0.232[c]	+0.52	...
GS9b		...	...	J033302.44-275145.3	3.5	...	0.090[b]	0.089[c]	+0.29	...
GS9c		...	...	J033302.90-275151.0	5.1	...	...	0.179[c]	+0.32	...
GS10a[d]	9.0	J033207.30-275120.8	5.3	J033207.27-275120.1	5.9	0.053	0.181[b]	0.233[c]	+0.14	**2.035**
GS10b		...	...	J033207.09-275128.9	3.2	...	...	0.077[c]	+0.04	...
GS11a	9.0	J033215.33-275037.6	6.5	J033215.29-275038.3	6.8	0.081	0.404	...	−0.02	...
GS12a	9.0	**J033229.30-275619.9**	4.0	J033229.29-275619.2	3.3	**0.032**[a]	0.113	0.092	+0.10	**4.762**
GS13a	9.0	**J033211.94-274615.3**	2.1	**J033211.92-274615.2**	2.2	**0.009**[a]	**0.050**	**0.041**	+0.24	...
GS13b		J033211.60-274613.0	5.7	J033211.56-274613.0	6.1	0.065[a]	0.338	0.283	+0.02	1.039
GS13c		J033212.23-274621.6	6.3	J033212.22-274620.6	5.5	0.076[a]	0.285	...	−0.25	1.033
GS14a[d]	9.0	...	...	J033234.73-275217.3	3.1	...	...	0.083	+0.04	**3.640**
GS15a[d]	9.0	J033151.61-274552.1	12.7	J033151.54-274553.1	11.3	0.264[a]	...	0.619[c]	+0.44	...
GS15b		...	...	J033151.36-274601.0	5.6	...	...	0.215[c]	+0.05	...
GS15c		...	...	J033150.97-274554.7	6.4	...	...	0.264[c]	+0.00	...
GS16a	10.5	J033238.00-274400.8	6.1	J033238.00-274400.6	6.2	0.072[a]	0.345	0.290	+0.53	1.719
GS16b		J033237.35-274407.8	7.9	J033237.40-274407.0	7.0	0.119[a]	0.419	...	−0.29	1.017
GS17a	10.5	**J033222.54-274818.2**	1.8	**J033222.54-274817.6**	1.2	**0.007**[a]	**0.017**	...	−0.27	...
GS17b		...	...	**J033222.54-274814.9**	1.5	...	**0.026**	**0.021**	+0.19	...
GS17c		...	...	J033222.15-274811.3	7.0	...	0.415	0.351	+0.36	...
GS17d		J033222.53-274804.6	11.8	J033222.51-274804.6	11.8	0.245	...	0.710	+0.23	...
GS17e		J033222.26-274804.8	12.1	J033222.26-274804.3	12.5	0.254[a]	0.824	0.755	+0.32	...
GS18a	9.3	**J033243.48-274639.5**	4.2	J033243.52-274639.1	3.7	**0.035**[a]	0.138	0.113	+0.47	...
GS18b		J033243.98-274635.9	5.2	J033244.01-274635.2	5.5	0.053[a]	0.288	0.240	+0.31	2.688
GS18c		...	...	J033243.45-274634.3	2.3	...	0.058	...	−0.39	...
GS19a	10.5	J033222.92-274125.4	7.3	J033222.87-274124.9	8.0	0.102	0.509	0.438	+0.22	...
GS19b		J033222.70-274126.7	8.7	J033222.70-274126.4	8.8	0.143	...	0.501	+0.36	...
GS19c		...	...	J033223.76-274131.5	6.6	...	0.181[b]	0.280[c]	+0.17	...
GS20a	10.5	**J033235.09-275532.6**	4.6	J033235.06-275532.7	4.5	**0.042**	0.200	...	−0.43	**0.0369**
GS21a	10.4	J033247.58-274452.4	7.5	J033247.59-274452.2	7.4	0.108	0.452	0.385	+0.24	1.910
GS21b		...	...	J033247.29-274444.3	2.5	...	0.065	0.053	+0.13	...
GS22a	13.0	J033212.56-274305.9	7.8	J033212.54-274306.1	7.9	0.116[a]	0.502	0.431	+0.30	1.794
GS22b		...	...	J033212.56-274252.9	5.4	...	...	0.231	+0.13	...
GS23a	12.2	**J033221.14-275626.6**	3.9	J033221.12-275626.5	4.2	**0.030**[a]	0.176	0.145	+0.45	...
GS23b[d]		J033221.61-275623.7	5.5	J033221.58-275623.5	5.4	0.058	0.274	0.228	+0.19	**2.277**
GS24a	12.2	J033234.29-274941.1	8.7	J033234.26-274940.1	9.7	0.141[a]	0.649	0.571	+0.35	...
GS25a[d]	13.6	J033246.84-275121.0	6.8	J033246.82-275120.8	7.0	0.089	0.416	0.352	+0.33	**2.292**
GS26a	12.2	...	...	J033215.56-274335.5	5.5	...	...	0.237	+0.22	...
GS26b		...	...	J033216.41-274341.1	7.1	...	...	0.366	+0.25	2.331
GS26c		...	...	J033215.42-274339.7	7.2	...	...	0.372	+0.10	...

Table 1 – *continued*

AzTEC ID	R_S (arcsec)	Radio coordinate (J2000)	Dist. (arcsec)	*Spitzer* coordinate (J2000)	Dist. (arcsec)	$P_{1.4}$	$P_{24\mu m}$	P_{colour}	$[3.6] - [4.5]$ (mag)	z_{spec}
GS27a	13.0	J033242.09-274141.7	13.0	J033242.06-274141.3	13.6	0.291^a	0.870	0.807	+0.38	2.577
GS28a	13.0	...	...	J033242.78-275212.6	2.9	...	0.089	0.073	+0.55	...
GS28b		...	...	J033242.53-275216.9	4.4	...	...	0.136^c	+0.07	...
GS29a	13.0	...	...	**J033158.67-274500.2**	3.8	...	0.050^b	...	−0.43	**0.577**
GS29b		...	...	J033159.30-274500.4	4.6	...	0.122^b	...	−0.10	2.340
GS30a	13.5	J033220.65-274235.3	6.5	J033220.66-274234.5	7.2	0.082^a	0.439	0.373	+0.19	...
GS30b		J033221.52-274242.5	9.0	J033221.48-274241.7	8.4	0.152^a	0.540	0.466	+0.26	...
GS30c		...	...	J033220.90-274236.9	4.4	...	...	0.160	+0.29	...
GS31a	13.6	**J033242.76-273927.4**	2.7	**J033242.81-273927.1**	2.1	0.015^a	**0.046**	...	−0.25	**1.843**
GS31b		J033243.47-273929.3	7.9	J033243.49-273929.1	7.9	0.118^a	0.502	...	−0.36	0.733
GS32a	13.5	J033308.60-275134.8	9.6	J033308.61-275134.4	9.2	0.162	0.421^b	...	−0.42	0.734
GS32b		J033309.93-275131.4	10.5	J033309.88-275131.0	9.8	0.191	0.456^b	...	−0.12	...
GS32c		J033310.13-275125.1	13.4	J033310.12-275124.7	13.3	0.291	0.683^b	0.741^c	+0.08	...
GS33a	13.0	J033248.78-275314.8	7.4	J033248.78-275314.4	7.4	0.104^a	0.457	0.390	+0.34	...
GS34a	13.5	J033229.94-274301.6	11.5	J033229.95-274301.7	11.5	0.235^a	0.768	0.693	+0.09	1.356
GS34b		...	...	J033229.85-274317.7	5.8	...	0.311	...	−0.15	1.097
GS34c		...	...	J033229.74-274306.7	6.0	...	0.326	0.273	+0.14	...
GS34d		...	...	J033230.07-274306.8	7.9	...	...	0.430	+0.12	...
GS34e		...	...	J033229.47-274322.2	9.9	...	0.664	0.586	+0.15	1.609
GS35a	13.0	**J033227.21-274052.1**	2.0	**J033227.17-274051.7**	1.6	**0.008**	**0.027**	**0.022**	+0.37	...
GS35b		...	...	J033226.84-274056.1	4.9	...	...	0.191	+0.37	...
GS36a	13.5	...	...	J033214.42-275515.1	6.4	...	...	0.304	+0.68	...
GS37a	15.0	J033256.83-274627.8	13.3	J033256.79-274626.8	12.2	0.285^a	0.631^b	0.675^c	+0.08	...
GS37b		...	...	J033256.79-274612.1	4.3	...	...	0.132^c	+0.15	...
GS38a	13.5	J033209.71-274248.6	7.8	J033209.70-274248.2	7.5	0.116	0.463	...	−0.55	0.735
GS38b		...	...	J033208.74-274248.6	7.4	...	0.453	0.386	+0.15	...
GS39a^d	15.0	J033154.44-274531.6	6.7	J033154.39-274530.3	7.9	0.083	...	0.379^c	+0.55	...
GS39b		...	...	J033154.54-274539.5	2.8	...	0.053^b	...	−0.10	...
GS40a	15.0	...	...	J033201.15-274635.9	10.2	...	0.479^b	...	−0.01	...
GS41a	6.7	J033302.78-275653.1	8.2	J033302.78-275652.8	8.0	0.120^a	...	0.386^c	+0.23	...
GS41b^d		J033302.71-275642.5	8.6	J033302.68-275642.6	8.3	0.132	0.348^b	0.408^c	+0.30	...
GS41c		...	...	J033302.23-275651.4	2.7	...	...	0.053^c	+0.23	...
GS41d		...	...	J033302.55-275644.8	5.5	...	0.173^b	0.208^c	+0.15	...
GS42a^d	6.9	...	...	J033314.16-275612.0	4.6	...	...	0.146^c	+0.04	...
GS43a^d	8.6	...	...	J033302.90-274432.9	4.7	...	...	0.157^c	+0.23	...
GS44a	10.4	J033240.84-273752.3	9.3	J033240.84-273752.6	8.9	0.151	0.389^b	...	−0.07	...
GS45a	12.2	J033218.65-273743.3	12.1	J033218.58-273742.3	12.0	0.244^a	0.620^b	...	−0.32	...
GS45b		...	...	**J033219.09-273733.5**	0.9	...	0.004^b	0.006^c	+0.18	...
GS45c		...	...	**J033219.21-273731.5**	1.9	...	0.016^b	0.026^c	+0.21	...
GS45d		...	...	J033218.94-273730.0	4.3	...	...	0.129^c	+0.20	...
GS46a	13.0	...	...	J033157.27-275656.2	6.2	...	0.226^b	0.255^c	+0.17	...
GS47a^d	12.2	J033208.27-275814.0	7.6	J033208.23-275813.9	7.8	0.105^a	0.280^b	0.371^c	+0.46	...

^{a}Radio sources identified with IRAC positions priors.
^{b}MIPS 24 μm flux and P statistic determined from the FIDEL catalogue.
^{c}IRAC fluxes and P statistic determined from SIMPLE catalogue.
^{d}Robust identification based on AzTEC+LABOCA analysis.

the nature of the individual counterpart candidates is discussed in Appendix A.

2.1 Methods

Since the origin of the millimetre continuum emission detected by the AzTEC instrument is likely reprocessed radiation from dust-obscured starburst or AGN activity, the main data sets we examine for the multiwavelength counterpart identification are mid-IR data from the *Spitzer* MIPS 24 μm [full width at half-maximum (FWHM) angular resolution of $\theta_{FWHM} \sim 6$ arcsec] and IRAC 3.6 to 8.0 μm band ($\theta_{FWHM} \sim 2$ arcsec) and deep radio continuum data obtained using the VLA ($\theta_{FWHM} \sim 2$ arcsec), exploiting the well-known radio–IR correlation for star-forming galaxies (see review by

Condon 1992). The *Spitzer* IRAC and MIPS images and catalogues used come from the *Spitzer* GOODS,[1] the Far-Infrared Deep Extragalactic Legacy (FIDEL)[2] and the *Spitzer* IRAC/MUSYC Public Legacy In E-CDFS (SIMPLE)[3] Legacy Surveys. The radio continuum data used come from the VLA 1.4 GHz deep imaging survey ($\sigma \sim 8$ μJy; Kellermann et al. 2008; Miller et al. 2008). Given their high resolution, the astrometric accuracy of these catalogues is sufficient to identify unique optical and NIR counterparts in the deep ground-based telescope or *Hubble Space Telescope* (*HST*) images

[1] http://www.stsci.edu/science/goods/
[2] http://ssc.spitzer.caltech.edu/legacy/abs/dickinson2.html
[3] http://www.astro.yale.edu/dokkum/simple/

Table 2. Photometry data listed in the same order as the identifications in Table 1. All upper limits are given at a significance of 3σ. De-boosted AzTEC 1.1 mm flux densities are taken from Downes et al. (2011). The LABOCA 870 μm photometry comes from Weiss et al. (2009).

AzTEC ID	1.4 GHz (μJy)	1.1 mm (mJy)	870 μm (mJy)	24 μm (μJy)	8 μm (μJy)	5.8 μm (μJy)	4.5 μm (μJy)	3.6 μm (μJy)	i (mag)	K (mag)
GS1a	32.0 ± 6.3	$6.7^{+0.6}_{-0.7}$	9.2 ± 1.2	122.0 ± 5.2	28.2 ± 0.7	20.0 ± 0.6	14.60 ± 0.09	10.39 ± 0.06	>25.3	>22.9
GS2.1a	50.7 ± 6.2	$6.4^{+0.7}_{-0.6}$	9.1 ± 1.2	148.0 ± 4.1	21.4 ± 0.5	14.0 ± 0.4	10.62 ± 0.06	7.50 ± 0.04	26.1	24.2
GS2.1b	44.1 ± 6.2	...	...	<13.9	<1.3	<1.2	<0.19	<0.11	>27.5	>24.5
GS2.1c	<18	...	...	16.0 ± 3.2	6.9 ± 0.5	7.8 ± 0.4	7.73 ± 0.06	10.36 ± 0.04	22.1	21.8
GS2.2a	<18	$4.0^{+0.6}_{-0.7}$	...	62.9 ± 3.9	16.2 ± 0.5	15.6 ± 0.4	17.98 ± 0.07	22.28 ± 0.04	22.9	21.1
GS2.2b	<18	...	...	83.2 ± 4.2	23.8 ± 0.5	24.8 ± 0.4	20.46 ± 0.07	16.10 ± 0.04	26.4	23.3
GS2.2c	<18	...	...	<12.8	14.3 ± 0.5	19.9 ± 0.4	16.75 ± 0.07	15.30 ± 0.04	26.6	21.3
GS3a	40.7 ± 6.5	$4.8^{+0.6}_{-0.5}$	8.8 ± 1.2	49.2 ± 2.8	13.0 ± 0.5	8.7 ± 0.4	6.17 ± 0.06	4.38 ± 0.04	>25.3	>22.9
GS3b	<19	...	...	<12.6	3.1 ± 0.5	4.2 ± 0.4	3.13 ± 0.07	2.76 ± 0.04	>25.3	>22.9
GS4a	25.4 ± 6.5	$5.1^{+0.6}_{-0.6}$	8.8 ± 1.2	<16.7	18.6 ± 0.9	13.6 ± 0.7	9.32 ± 0.13	7.21 ± 0.06	26.8	>24.5
GS5a	96.4 ± 6.7	$4.8^{+0.6}_{-0.7}$	3.9 ± 1.4	521.7 ± 10.9	58.2 ± 0.9	62.6 ± 0.9	73.70 ± 0.18	59.67 ± 0.11	23.1	20.7
GS5b	111.7 ± 6.7	...	...	282.3 ± 7.7	16.1 ± 0.9	17.9 ± 0.9	14.12 ± 0.18	9.50 ± 0.11	25.7	22.6
GS6a	31.0 ± 6.3	$3.6^{+0.5}_{-0.6}$	5.8 ± 1.4	141.0 ± 4.0	27.4 ± 0.5	25.6 ± 0.4	17.70 ± 0.06	11.72 ± 0.04	28.3	22.8
GS6b	<18	...	...	94.2 ± 3.7	11.4 ± 0.5	12.1 ± 0.4	17.00 ± 0.06	21.09 ± 0.04	23.5	21.1
GS7a	51.2 ± 6.4	$3.8^{+0.6}_{-0.7}$	9.1 ± 1.2	103.0 ± 9.3	22.4 ± 0.6	17.7 ± 0.6	12.03 ± 0.12	7.89 ± 0.08	>25.3	>22.9
GS7b	<19	...	...	60.0 ± 9.5	5.0 ± 0.9	7.6 ± 0.7	9.33 ± 0.23	9.03 ± 0.09	24.2	>22.9
GS8a	71.4 ± 6.6	$3.4^{+0.6}_{-0.6}$	7.5 ± 1.2	620.0 ± 6.5	42.9 ± 0.7	62.6 ± 0.6	50.07 ± 0.10	36.85 ± 0.06	24.7	21.6
GS8b	<19	...	...	164.0 ± 4.8	27.5 ± 0.6	20.6 ± 0.5	15.73 ± 0.09	13.44 ± 0.05	26.6	>22.9
GS9a	86.8 ± 6.6	$3.6^{+0.6}_{-0.6}$	...	228.9 ± 10.3	27.3 ± 0.9	14.9 ± 0.9	12.37 ± 0.17	7.69 ± 0.13	25.3	>22.9
GS9b	<19	...	...	117.4 ± 9.7	3.8 ± 0.9	6.3 ± 0.9	7.27 ± 0.17	5.58 ± 0.12	>27.5	22.6
GS9c	<19	...	...	<23.1	8.7 ± 0.9	8.0 ± 0.9	8.06 ± 0.17	5.99 ± 0.13	>25.3	>22.9
GS10a	89.3 ± 6.4	$3.8^{+0.7}_{-0.7}$	7.6 ± 1.3	214.0 ± 8.4	32.0 ± 0.7	40.5 ± 0.9	47.03 ± 0.22	41.21 ± 0.15	23.6	21.3
GS10b	<19	...	...	<22.7	4.8 ± 1.0	6.9 ± 1.2	5.73 ± 0.22	5.52 ± 0.15	26.8	>22.9
GS11a	46.0 ± 6.4	$3.3^{+0.6}_{-0.6}$	...	117.0 ± 4.5	32.5 ± 0.4	23.8 ± 0.3	22.45 ± 0.05	22.89 ± 0.04	>25.3	>22.9
GS12a	21.0 ± 6.5	$3.1^{+0.6}_{-0.6}$	5.1 ± 1.4	31.6 ± 5.1	12.2 ± 0.5	7.2 ± 0.5	3.89 ± 0.07	3.54 ± 0.04	25.2	>22.9
GS13a	22.8 ± 6.3	$3.1^{+0.6}_{-0.6}$	...	34.7 ± 3.6	6.2 ± 0.5	6.0 ± 0.4	5.32 ± 0.07	4.24 ± 0.04	26.8	22.5
GS13b	24.0 ± 6.3	...	...	112.0 ± 3.8	13.8 ± 0.5	14.5 ± 0.4	14.03 ± 0.07	13.72 ± 0.04	23.2	22.0
GS13c	23.7 ± 6.3	...	...	224.0 ± 3.7	31.9 ± 0.5	33.1 ± 0.4	42.70 ± 0.07	53.65 ± 0.05	22.5	20.2
GS14a	<18	$2.9^{+0.6}_{-0.5}$	3.3 ± 1.2	<12.8	<1.3	<1.2	1.24 ± 0.06	1.19 ± 0.04	25.2	23.9
GS15a	27.6 ± 6.5	$3.9^{+0.7}_{-0.8}$	4.2 ± 1.4	<24.2	16.0 ± 1.0	13.2 ± 0.9	9.29 ± 0.18	6.17 ± 0.12	>25.3	>22.9
GS15b	<19	...	...	<24.6	5.8 ± 1.0	5.7 ± 0.9	5.71 ± 0.18	5.47 ± 0.12	>25.3	>22.9
GS15c	<19	...	...	<25.0	<2.9	<2.6	1.12 ± 0.18	1.12 ± 0.12	>25.3	>22.9
GS16a	30.7 ± 6.4	$2.7^{+0.5}_{-0.6}$	...	46.4 ± 3.3	16.4 ± 0.5	10.9 ± 0.4	8.12 ± 0.07	4.98 ± 0.04	26.5	25.8
GS16b	22.1 ± 6.4	...	...	144.0 ± 3.5	15.7 ± 0.5	15.9 ± 0.4	21.74 ± 0.07	28.44 ± 0.04	23.0	20.6
GS17a	26.1 ± 6.3	$2.9^{+0.6}_{-0.6}$	...	71.3 ± 9.6	5.1 ± 0.4	4.6 ± 0.3	4.21 ± 0.05	5.42 ± 0.03	23.6	22.6
GS17b	<18	...	...	61.9 ± 7.2	21.2 ± 0.4	26.3 ± 0.3	20.19 ± 0.05	16.94 ± 0.03	26.0	22.8
GS17c	<18	...	...	200.0 ± 5.3	20.9 ± 0.4	23.9 ± 0.3	16.50 ± 0.05	11.79 ± 0.03	26.7	22.7
GS17d	42.1 ± 6.2	...	...	<12.3	11.3 ± 0.4	12.0 ± 0.3	9.07 ± 0.05	7.37 ± 0.03	25.2	23.6
GS17e	37.9 ± 6.2	...	...	23.5 ± 4.1	9.7 ± 0.4	7.1 ± 0.3	5.23 ± 0.05	3.88 ± 0.03	27.6	23.5
GS18a	25.1 ± 6.3	$3.1^{+0.6}_{-0.6}$	6.4 ± 1.3	84.6 ± 2.9	13.1 ± 0.4	11.7 ± 0.3	7.56 ± 0.05	4.91 ± 0.03	28.1	>24.5
GS18b	20.2 ± 6.3	...	...	126.0 ± 4.0	22.2 ± 0.4	16.0 ± 0.3	10.85 ± 0.05	8.19 ± 0.03	24.5	23.2
GS18c	<18	...	...	91.4 ± 2.8	11.2 ± 0.4	12.6 ± 0.3	11.84 ± 0.05	16.97 ± 0.04	22.8	20.8
GS19a	34.0 ± 6.5	$2.6^{+0.5}_{-0.6}$	...	317 ± 17	18.9 ± 0.5	25.8 ± 0.4	22.97 ± 0.07	18.74 ± 0.04	24.2	21.7
GS19b	40.0 ± 6.5	...	...	149 ± 17	15.9 ± 0.5	22.7 ± 0.4	17.67 ± 0.07	12.72 ± 0.04	26.6	21.7
GS19c	<19	...	...	105.1 ± 10.7	9.1 ± 0.3	12.3 ± 0.3	11.61 ± 0.06	9.97 ± 0.04	26.9	21.6
GS20a	793 ± 99	$2.7^{+0.6}_{-0.6}$	...	4030.0 ± 44.1	3499.5 ± 0.6	1113.8 ± 0.6	759.28 ± 0.11	1131.36 ± 0.16	16.1	15.0
GS21a	43.6 ± 6.3	$2.7^{+0.6}_{-0.7}$	...	299.0 ± 4.0	16.6 ± 0.5	24.0 ± 0.4	19.97 ± 0.08	15.98 ± 0.04	25.3	22.5
GS21b	<18	...	...	27.8 ± 2.6	4.8 ± 0.5	6.9 ± 0.4	8.44 ± 0.08	7.51 ± 0.04	25.9	>24.5
GS22a	34.6 ± 6.5	$2.1^{+0.6}_{-0.6}$	...	290.0 ± 4.4	13.7 ± 0.5	15.3 ± 0.4	13.23 ± 0.07	10.02 ± 0.04	26.4	21.5
GS22b	<19	...	...	<11.4	<1.4	2.7 ± 0.4	2.55 ± 0.07	2.26 ± 0.04	25.9	22.8
GS23a	23.4 ± 6.5	$2.3^{+0.6}_{-0.6}$	...	42.4 ± 5.9	19.7 ± 0.5	18.9 ± 0.5	12.19 ± 0.07	8.06 ± 0.05	24.5	>22.9
GS23b	35.2 ± 6.5	...	4.7 ± 1.4	586.0 ± 6.2	36.4 ± 0.5	47.1 ± 0.5	46.86 ± 0.07	39.37 ± 0.05	24.0	21.2
GS24a	18.5 ± 6.1	$2.3^{+0.6}_{-0.6}$	...	90.8 ± 3.8	16.4 ± 0.4	9.8 ± 0.3	6.61 ± 0.05	4.79 ± 0.03	25.5	24.1
GS25a	89.5 ± 6.2	$1.9^{+0.5}_{-0.6}$	5.9 ± 1.3	140.0 ± 3.6	32.2 ± 0.5	24.5 ± 0.4	18.81 ± 0.06	13.88 ± 0.04	23.9	22.6

Table 2 – *continued*

AzTEC ID	1.4 GHz (μJy)	1.1 mm (mJy)	870 μm (mJy)	24 μm (μJy)	8 μm (μJy)	5.8 μm (μJy)	4.5 μm (μJy)	3.6 μm (μJy)	i (mag)	K (mag)
GS26a	<18	$2.2^{+0.5}_{-0.6}$	...	<11.3	2.4 ± 0.5	2.7 ± 0.4	3.64 ± 0.07	2.98 ± 0.04	25.2	24.6
GS26b	<18	...	...	<12.1	9.0 ± 0.5	7.1 ± 0.4	6.71 ± 0.07	5.35 ± 0.04	24.9	23.3
GS26c	<18	...	...	<11.0	11.5 ± 0.5	18.5 ± 0.4	23.55 ± 0.07	21.52 ± 0.04	25.9	21.3
GS27a	23.6 ± 6.5	$2.2^{+0.6}_{-0.6}$	...	171.0 ± 5.6	25.3 ± 0.5	23.7 ± 0.5	16.57 ± 0.07	11.67 ± 0.04	24.8	24.2
GS28a	<18	$2.1^{+0.6}_{-0.5}$	...	17.3 ± 2.6	10.8 ± 0.5	6.9 ± 0.4	4.33 ± 0.06	2.62 ± 0.04	26.5	23.6
GS28b	<18	...	...	<26.4	<1.0	<1.0	1.12 ± 0.06	1.05 ± 0.04	26.0	24.6
GS29a	<19	$2.3^{+0.6}_{-0.6}$	...	54.4 ± 10.7	15.3 ± 1.0	27.4 ± 0.9	32.93 ± 0.20	49.07 ± 0.13	20.4	19.8
GS29b	<19	...	...	47.4 ± 10.1	5.2 ± 1.0	6.2 ± 1.0	5.51 ± 0.19	6.04 ± 0.13	23.8	22.5
GS30a	37.2 ± 6.2	$1.8^{+0.5}_{-0.6}$	...	459.0 ± 6.2	25.9 ± 0.5	35.4 ± 0.4	32.99 ± 0.07	27.57 ± 0.04	24.6	21.0
GS30b	24.2 ± 6.2	...	...	316.0 ± 4.2	27.6 ± 0.5	33.7 ± 0.4	34.14 ± 0.07	26.96 ± 0.04	26.3	21.2
GS30c	<18	...	...	<10.5	2.4 ± 0.5	2.7 ± 0.4	2.20 ± 0.07	1.69 ± 0.04	25.7	24.2
GS31a	25.1 ± 6.9	$2.2^{+0.7}_{-0.7}$	...	427.0 ± 5.6	31.5 ± 0.7	49.3 ± 0.7	51.71 ± 0.11	64.98 ± 0.07	21.6	19.8
GS31b	37.5 ± 6.9	...	...	521.0 ± 6.7	60.0 ± 0.8	75.4 ± 0.7	70.27 ± 0.11	97.45 ± 0.07	22.5	19.6
GS32a	30.3 ± 6.8	$2.3^{+0.8}_{-0.8}$	...	371.1 ± 11.7	32.4 ± 0.9	47.0 ± 0.9	45.47 ± 0.17	67.02 ± 0.12	21.6	19.8
GS32b	34.8 ± 6.9	...	...	265.6 ± 11.9	32.8 ± 0.9	35.8 ± 0.9	57.75 ± 0.17	64.39 ± 0.13	22.4	20.2
GS32c	46.3 ± 6.9	...	...	270.4 ± 12.2	12.4 ± 0.9	12.2 ± 0.9	11.06 ± 0.17	10.27 ± 0.13	25.4	>22.9
GS33a	28.6 ± 6.2	$2.0^{+0.5}_{-0.6}$	...	16.1 ± 3.7	5.1 ± 0.5	2.4 ± 0.4	1.70 ± 0.07	1.24 ± 0.04	26.9	24.1
GS34a	33.0 ± 6.3	$1.7^{+0.5}_{-0.6}$	...	173.0 ± 3.3	32.9 ± 0.5	28.8 ± 0.4	35.68 ± 0.07	32.72 ± 0.05	23.4	20.9
GS34b	<19	...	...	41.4 ± 3.7	14.3 ± 0.5	16.7 ± 0.4	20.34 ± 0.07	23.42 ± 0.04	23.5	21.2
GS34c	<18	...	...	56.8 ± 3.3	5.8 ± 0.5	8.1 ± 0.4	10.08 ± 0.07	8.83 ± 0.04	25.6	22.3
GS34d	<19	...	...	<10.5	3.5 ± 0.5	4.7 ± 0.4	4.54 ± 0.07	4.05 ± 0.04	24.3	23.4
GS34e	<19	...	...	70.1 ± 3.2	14.9 ± 0.5	17.2 ± 0.4	19.86 ± 0.07	17.31 ± 0.04	24.4	22.1
GS35a	41.3 ± 6.7	$2.1^{+0.6}_{-0.6}$	...	153.0 ± 3.8	22.2 ± 0.5	19.8 ± 0.4	14.72 ± 0.07	10.51 ± 0.04	24.7	23.1
GS35b	<19	...	...	<12.9	2.4 ± 0.5	3.1 ± 0.4	2.76 ± 0.07	1.96 ± 0.04	25.3	23.5
GS36a	<19	$2.0^{+0.6}_{-0.6}$	...	<17.4	7.6 ± 0.7	5.2 ± 0.6	2.84 ± 0.10	1.52 ± 0.06	>25.3	>22.9
GS37a	20.5 ± 6.4	$2.1^{+0.8}_{-0.8}$	...	112.9 ± 7.0	17.1 ± 1.0	16.1 ± 1.0	15.08 ± 0.20	13.95 ± 0.13	25.4	>22.9
GS37b	<19	...	...	<21.5	<3.0	3.6 ± 1.0	2.89 ± 0.19	2.52 ± 0.13	25.9	>22.9
GS38a	220.0 ± 6.5	$1.7^{+0.6}_{-0.6}$	...	39.2 ± 2.6	34.2 ± 0.5	58.1 ± 0.4	67.61 ± 0.08	112.41 ± 0.06	21.1	18.8
GS38b	<19	...	...	184.0 ± 4.9	15.8 ± 0.5	21.2 ± 0.4	16.86 ± 0.07	14.66 ± 0.04	>25.3	>22.9
GS39a	37.2 ± 6.6	$1.5^{+0.7}_{-0.7}$	3.8 ± 1.4	<26.9	8.4 ± 1.0	6.7 ± 0.9	4.91 ± 0.19	2.96 ± 0.12	>25.3	>22.9
GS39b	<19	...	...	48.4 ± 7.4	5.9 ± 1.0	8.5 ± 0.9	9.17 ± 0.18	10.04 ± 0.12	23.1	22.3
GS40a	<19	$1.8^{+0.6}_{-0.6}$	...	169.6 ± 8.3	7.9 ± 1.0	13.7 ± 1.1	13.45 ± 0.20	13.64 ± 0.13	25.1	22.0
GS41a	28.2 ± 7.0	$7.2^{+0.9}_{-1.0}$	...	<22.4	4.9 ± 0.9	6.5 ± 0.9	4.35 ± 0.17	3.52 ± 0.12	>25.3	23.3
GS41b	223.0 ± 7.0	...	12.0 ± 1.2	62.0 ± 6.0	4.7 ± 2.4	6.6 ± 2.6	5.35 ± 0.46	4.06 ± 0.34	>25.3	>22.9
GS41c	<21	...	...	<23.9	<2.7	<2.8	1.71 ± 0.17	1.39 ± 0.12	>25.3	>22.9
GS41d	<20	...	...	212.2 ± 6.8	17.1 ± 0.9	19.9 ± 0.9	18.94 ± 0.17	16.55 ± 0.12	24.3	22.0
GS42a	<21	$9.2^{+1.2}_{-1.4}$	14.5 ± 1.2	<26.6	5.7 ± 0.9	<2.7	2.50 ± 0.18	2.40 ± 0.13	25.4	>22.9
GS43a	<20	$6.1^{+1.0}_{-1.1}$	6.7 ± 1.3	<25.6	4.0 ± 0.9	<2.7	1.26 ± 0.16	1.02 ± 0.12	>25.3	>22.9
GS44a	43.5 ± 7.3	$3.2^{+0.8}_{-0.8}$	5.0 ± 1.4^a	143.1 ± 9.3	19.4 ± 1.0	17.9 ± 1.0	27.54 ± 0.19	29.39 ± 0.14	23.7	21.5
GS45a	33.7 ± 6.9	$4.0^{+1.2}_{-1.1}$	8.1 ± 1.2	446.3 ± 9.4	91.9 ± 1.1	106.6 ± 1.1	140.28 ± 0.21	188.72 ± 0.15	18.6	17.8
GS45b	<20	...	...	64.4 ± 9.3	4.3 ± 1.1	5.9 ± 1.1	5.02 ± 0.21	4.24 ± 0.15	>25.3	>22.9
GS45c	<20	...	...	48.9 ± 9.2	7.3 ± 1.1	5.8 ± 1.1	5.33 ± 0.22	4.41 ± 0.15	26.4	>22.9
GS45d	<20	...	...	<37.7	3.8 ± 1.1	<3.3	2.11 ± 0.22	1.75 ± 0.14	>25.3	>22.9
GS46a	<21	$4.8^{+1.4}_{-1.7}$	4.8 ± 1.4^a	74.6 ± 9.6	6.7 ± 0.8	9.0 ± 0.9	10.54 ± 0.16	9.01 ± 0.11	25.1	>22.9
GS47a	43.2 ± 7.0	$3.5^{+1.0}_{-1.0}$	7.3 ± 1.2	72.3 ± 10.6	9.7 ± 1.0	9.6 ± 0.9	6.88 ± 0.18	4.51 ± 0.12	>25.3	>22.9

^{a}The AzTEC and LABOCA centroid positions are offset by a significant amount ($\gtrsim 10$ arcsec).

when such a counterpart is present. The *i*- and *K*-band photometry of the counterpart candidates are also reported from the band-merged GOODS team photometry catalogue (Grogin et al., in preparation) constructed using a template fitting software package TFIT (Laidler et al. 2007) and the Multiwavelength Survey by Yale–Chile (Gawiser et al. 2006).

Unlike most previous works, we employed a variable search radius based on the beam size ($\theta_{FWHM} \sim 30$ arcsec) and the signal-to-noise ratio (S/N) of the AzTEC detection. Given the modest S/N (typically ≤ 10), the positional offset between an AzTEC source and its counterpart is expected to be dominated by the map noise.

This means we can exploit the measured S/N of each detection to constrain the counterpart identification. We derive the search radius, R_S, listed in Table 1 empirically through simulations by injecting artificial sources into the signal map one at a time and measuring the distribution in the input to output source positions as described in Paper I. For each AzTEC source we select R_S such that there is a 95 per cent probability that the true position of the source (assumed to be the position of the radio and/or *Spitzer* counterpart) will be within R_S of the AzTEC centroid.

The primary method of identifying AzTEC counterparts is the 'P statistic' described by Downes et al. (1986). This method computes

the likelihood of a chance coincidence for each source in the comparison catalogue from the measured catalogue source density and the distance to a given AzTEC source position. Following previous work, a counterpart with a *P* statistic less than 0.05 is deemed a 'robust' identification, while a counterpart with $0.05 < P < 0.20$ is considered a 'tentative' identification. Unlike most works, however, we compute all *P* statistics based on the number density of *all* sources in the comparison catalogue, rather than the number density of sources *brighter* than the candidate counterpart in question. This means that all candidate counterparts equidistant from the AzTEC centroid will have the same *P* statistic. This avoids biasing the identifications to the brightest radio and mid-IR sources, which could result in more misidentifications with low-redshift galaxies.

For the radio data, we created a $\geq 4\sigma$ catalogue using the SAD program in the Astronomical Image Processing System (AIPS).[4] This program builds a catalogue iteratively by first identifying bright pixels and then quantitatively testing their significance by fitting the point spread function (PSF) to the surrounding pixel brightness distribution. By allowing for a collection of connected sources as an acceptable model, this algorithm also provides a good estimate of the radio flux for extended objects as well. Submm/mm galaxies are almost always associated with IRAC galaxies with faint but visible radio emission. The extremely deep *Spitzer* data in these GOODS fields ensures that radio sources without an IRAC counterpart are rare as reported by Kellermann et al. (2008), who find that only three out of 266 catalogued radio sources have no apparent counterpart at any other wavelengths. Taking advantage of this fact, we probe deeper into the radio data by creating a combined IRAC+VLA radio catalogue by using the positions of IRAC sources detected with $(S/N)_{3.6} \geq 4$ as prior positions. For each IRAC source, we fit a 2D Gaussian to the radio map at the IRAC position, fixing the FWHM to 1.6 and 2.8 arcsec in RA and Dec., respectively, based on the best-fitting Gaussian to the synthesized beam (Miller et al. 2008). We limit the location of the peak to within 2 arcsec of the initial IRAC position. If the best-fitting 1.4 GHz peak emission is $>3\sigma$ of the rms noise in the surrounding region, we include this in our combined IRAC+VLA catalogue. This list is cross-checked with the $>4\sigma$ radio catalogue created by the SAD program, and we use the SAD catalogue flux estimates where available. The number density of IRAC+VLA sources in this catalogue is 8330 deg^{-2} for the GOODS-S+VLA catalogue, and 7860 deg^{-2} for the shallower SIMPLE+VLA catalogue.

For the MIPS 24 µm catalogues, we use the number density of $(S/N)_{24} \geq 4$ sources to compute the *P* statistics, which are 45 700 and 25 600 deg^{-2} for the GOODS-S and FIDEL 24 µm catalogues, respectively.

The third and an entirely new method we use for identifying SMG counterparts employs their characteristic red IRAC colour. Interferometric imaging studies of SMGs in submillimetre continuum (Iono et al. 2006; Wang et al. 2007b, 2011; Younger et al. 2007, 2008, 2009; Hatsukade et al. 2010; Tamura et al. 2010; Ikarashi et al. 2011) have shown that every source is detected in the IRAC 3.6 and 4.5 µm bands at the ≥ 1 µJy level, while their radio and MIPS 24 µm counterparts are not always detected in the best available data. By examining the spectral energy distribution (SED) of these IRAC counterparts, Yun et al. (2008) showed that SMGs as a population have characteristic red IRAC colours, similar to dust obscured AGN as proposed by Lacy et al. (2004) and Stern et al. (2005). These SMGs are systematically offset from the colour region associated

with power-law AGN, however. Citing theoretical colour tracks of dust obscured starbursts, Yun et al. advocated a dust-obscured young stellar population as the origin of the red IRAC colour (see their figs 1 and 2). Objects with red IRAC colour are rare (~ 1 arcmin^{-2} for $[3.6] - [4.5] \geq 0.0$) and distinct from the large number of foreground galaxies with characteristically *blue* IRAC colours. Both of these qualities can be successfully exploited for distinguishing the SMG counterpart candidates. Several colour combinations are proposed by Yun et al., and we adopt here the simplest form, $[3.6] - [4.5] \geq 0.0$, since these two bands are the most sensitive and the most robust among the four IRAC bands. In computing *P* statistics for the IRAC counterparts, we thus use the number density of IRAC sources with $[3.6] - [4.5] \geq 0.0$, $(S/N)_{3.6} > 4$ and $S_{3.6} > 1$ µJy. These are 36 900 and 31 400 deg^{-2} for the GOODS-S and SIMPLE IRAC catalogues, respectively.

Examining the *Spitzer* IRAC and MIPS properties of 73 radio-selected SMGs, Hainline et al. (2009) reported that an IRAC colour selection method similar to what we adopted is more successful in identifying correct counterparts than the IRAC colour–magnitude selection method described by Pope et al. (2006), but they caution that the density of sources meeting the Yun et al. (2008) colour selection criteria is high enough to diminish the utility of this method. We adopt a more selective limit of $[3.6] - [4.5] \geq 0.0$, which is more effective in reducing the foreground confusion. In addition, we also employ a *P* statistic analysis to give our method a more discriminative power.

2.2 Counterpart identification results

Finding charts for the 48 AzTEC/GS sources (GS2 is split into two) are shown in Fig. 1 in the order they appeared in Paper I. Sources meeting the radio, MIPS 24 µm and red IRAC colour selection criteria are identified in each 30×30 arcsec^2 image centred on the AzTEC source position. A unique counterpart is easily identifiable in about 50 per cent of the cases, while two or more candidates are present in others, requiring a more systematic and quantitative analysis.

Candidate radio and *Spitzer* counterparts and their computed *P* statistics are given in Table 1. All 'robust' counterparts satisfying $P \leq 0.05$ in any of the three bands are highlighted in boldface letters based on the analysis of the radio ($P_{1.4}$), MIPS 24 µm ($P_{24\,\mu m}$) or the IRAC colour (P_{colour}) properties. For 21 out of 48 cases, an 870 µm Large APEX Bolometer Camera (LABOCA) source (Weiss et al. 2009) is found within a 10-arcsec radius. Given the extremely low source density at 870 µm, the likelihood of a chance coincidence is essentially zero. Therefore, we elevate the status of the 13 AzTEC/GS sources initially classified as only as a 'tentative' identification based on the three bands analysis to 'robust' by folding in the astrometry of the 19 arcsec resolution 870 µm LABOCA Survey data (see Appendix A and Table 1) – the remaining AzTEC–LABOCA sources are already classified as 'robust'. We note that the low rate of coincidence between the LABOCA and AzTEC surveys (21/48 = 44 per cent) can be largely accounted by the low S/N detections of sources in both surveys, although the presence of high-redshift ($z > 3$) sources detected by AzTEC at 1.1 mm (e.g., Eales et al. 2003) may play a role. Taking advantage of the available rich multiwavelength data base, we provide complete photometry for each source in Table 2.

A robust counterpart is identified for 27 (56 per cent) out of 48 AzTEC/GS sources using the *P* statistic analysis combined with the LABOCA comparison. A total of 13, eight and five AzTEC sources have a robust counterpart based solely on the radio, MIPS
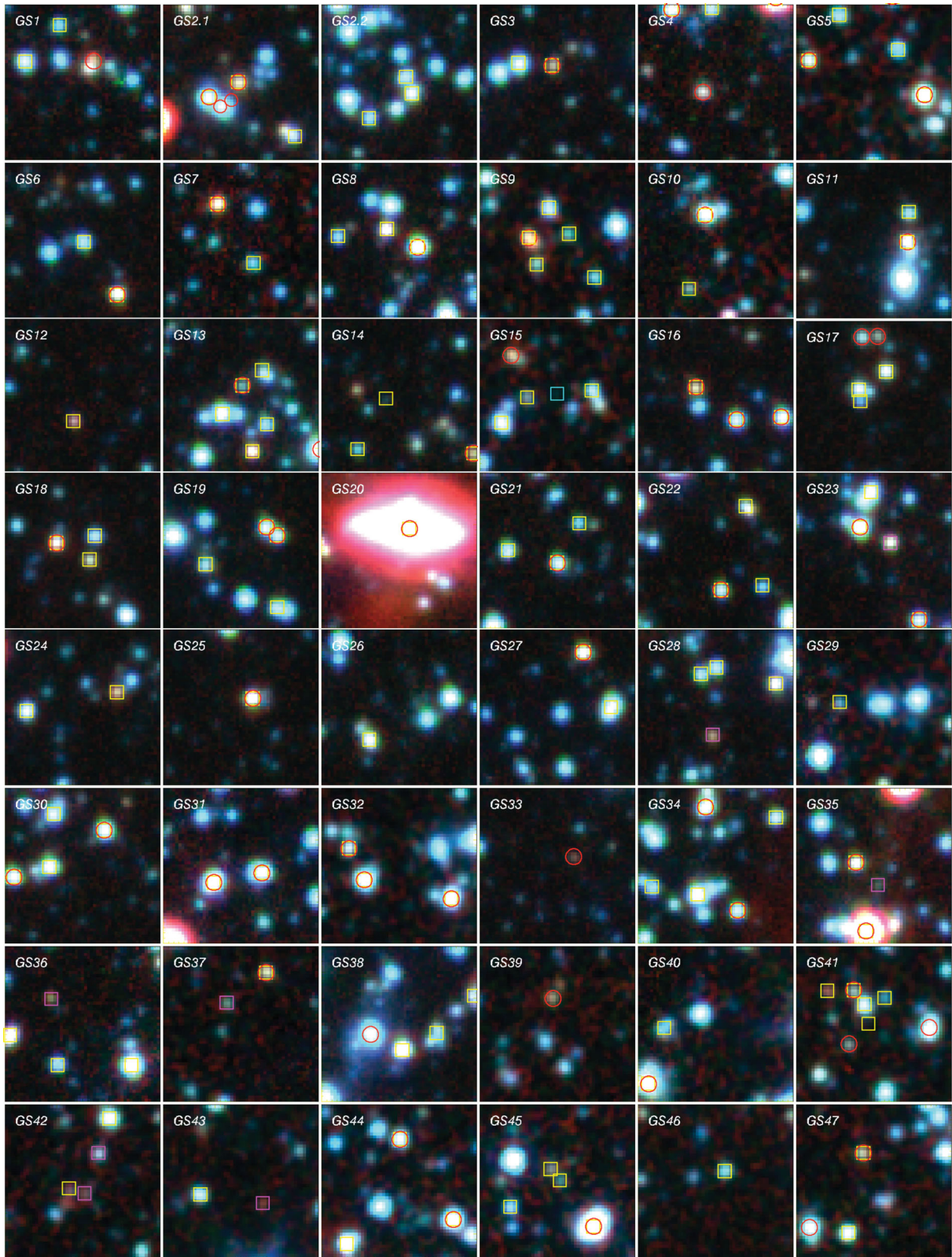
Figure 1. Finding charts for the 48 AzTEC/GS sources. These false colour images are 30×30 arcsec^2 in size and produced using the IRAC 3.6 μm (blue), 4.5 μm (green) and 8.0 μm (red) band images. Red circles mark the 1.4 GHz radio sources, while yellow squares are MIPS 24 μm sources. For sources without a plausible radio or MIPS 24 μm counterpart, IRAC sources with red IRAC colour ([3.6] − [4.5] > 0) are identified using magenta squares.

24 μm or IRAC colour analysis, respectively. An additional 19, 14 and 18 have tentative identifications with $0.05 < P < 0.20$, respectively. The robust radio and MIPS 24 μm identification rates of 13/48 (27 per cent) and 8/48 (17 per cent) are consistent with other similar studies. For example, using similar depth *Spitzer* data and slightly deeper radio data in the GOODS-North field, Pope et al. (2006) reported robust identification rates of 21/35 (60 per cent) and 6/35 (17 per cent) for the 1.4 GHz radio and MIPS 24 μm data and additional 10 and six tentative identifications, respectively. For the SCUBA Half Degree Extragalactic Survey (SHADES), Ivison et al. (2007) reported 56 and 54 per cent robust identification using much shallower MIPS 24 μm and comparable depth radio data.[5] The frequency of robust counterpart identification rate using red IRAC colour is similar to the MIPS 24 μm identification rate, indicating that their respective candidate source density is comparable.

Five AzTEC/GS sources (10 per cent) have two robust counterparts each. This multiple robust candidate identification rate is similar to those found in the GOODS-North field (Pope et al. 2006; Chapin et al. 2009) and the SHADES fields (Ivison et al. 2007; Clements et al. 2008). This multiple identification frequency is about 40 times higher than one would expect at random. A distinct possibility is that AzTEC counterpart sources are intrinsically strongly clustered (see Williams et al. 2011, and references therein), and the *P* statistic computes implicitly the likelihood that a particular candidate is *either the AzTEC counterpart or a close companion*. A strong clustering of SMGs is also expected if they represent a rapid build-up of stellar mass for $\geq M_*$ galaxies associated with a $\gtrsim 10^{12}$ M$_\odot$ dark matter halo – see discussions by Blain et al. (2004). Similar SEDs and redshifts of the multiple candidate counterparts for AzTEC/GS19, AzTEC/GS31 and GN19 (Pope et al. 2006) offer further anecdotal evidence for the clustering explanation. Wang et al. (2011) has reported two examples where a single SMG is broken up into multiple discrete components when observed at high angular resolution with an interferometer, further supporting the clustering scenario. Based on the simulations of two large gas-rich galaxies, Hayward et al. (2011) have suggested that some fraction of SMGs may be such closely interacting pairs just prior to a merger, and such a scenario would certainly boost the pair fraction. Uncertainties in the parameters chosen for the simulations, such as the details of the progenitors and the microphysics of star formation and gas consumption, make the comparison with the observed statistics difficult. These new observations should serve as important observational constraints for future modelling studies.

As shown in Table 2, only 22 out of 47 AzTEC/GS sources have an 870 μm LABOCA counterpart in the published catalogue by Weiss et al. (2009). Utilizing the radio and MIPS 24 μm *P* statistic and the IRAC 3.6 and 5.8 μm colour–magnitude selection by Pope et al. (2006), Biggs et al. (2011) identified 16 secure and three tentative counterparts among these 22 sources in common. In comparison, we identify 16 robust counterparts based on the *P* statistics alone, and all 19 individual candidates identified by Biggs et al. is either a robust (8) or tentative (11) counterpart in Table 1. The agreement between our results and theirs is very good mostly because both groups rely heavily on the radio continuum data for the counterpart identification.

2.3 Counterpart identification for SMGs in GOODS-North

To improve the statistics of the subsequent analysis, we also apply the same counterpart identification methods to the AzTEC 1.1 mm sources identified in the GOODS-North field (Perera et al. 2008), using the updated positions and photometry for these sources presented in Downes et al. (2011). Chapin et al. (2009) reported one or more robust counterpart to 21 out of 29 AzTEC sources and at least one tentative counterpart for the remainder. Our analysis, employing slightly different criteria, identifies 16 robust counterpart sources and one or more tentative counterpart to all but two of the remaining sources. The agreement between Chapin et al. and our work is quite good, as 13 out of 16 robust counterparts we identified were also identified as robust counterparts by Chapin et al.

3 REDSHIFTS AND SPECTRAL ENERGY DISTRIBUTIONS

Spectroscopic redshifts, $z_{\rm spec}$, are available for only a small subset (~30 per cent) of candidate counterparts despite the extensive redshift surveys that have been conducted in the GOODS-South field over the years (Le Fevre et al. 2004; Szokoly et al. 2004; Mignoli et al. 2005; Vanzella et al. 2005, 2006, 2008; Norris et al. 2006; Kriek et al. 2008; Popesso et al. 2009; Treister et al. 2009; Wuyts et al. 2009; Balestra et al. 2010; Silverman et al. 2010; Casey et al. 2011). The primary reason for this is that many of the candidate counterparts are extremely faint in the optical, with a median brightness of $i \sim 25.4$ among those listed in Table 2 (also see Fig. 6). Robustly identified AzTEC counterparts are even fainter as discussed below.

To learn more about the redshift distribution of these AzTEC sources and their nature, we rely on the extensive data base of extremely deep, multiwavelength broad-band photometry to analyse their SEDs using empirical and theoretical models. We first examine the optical/NIR photometry data using standard methods for estimating photometric redshift ('photo-z' hereafter), stellar mass (M_*) and SFR (SFR$_{\rm UV}$). We also employ an independent analysis of the IR-to-radio SEDs to derive photometric redshift, IR luminosity and dust-obscured SFR (SFR$_{\rm IR}$).

3.1 Optical/NIR SED analysis

The photometric redshift of each galaxy is computed by fitting the observed optical and NIR SED of the galaxies to stellar population synthesis models drawn from the PEGASE 2.0[6] library (Fioc & Rocca-Volmerange 1997). The models are shifted in the redshift range of $0 < z < 7$ with a step size of $\Delta z = 0.01$. For each galaxy, the weighted average photo-z is derived as

$$z_{\rm photo} = \frac{\int z P(z)\, {\rm d}z}{\int P(z)\, {\rm d}z}, \tag{1}$$

where $P(z)$ is the probability distribution function of redshift $P(z) \propto \exp(-\chi^2(z))$. To evaluate the reliability of our photo-z measurements, we compare the photo-zs with spectroscopic redshifts (spec-z) of GOODS galaxies with reliable emission-line redshifts in Fig. 2. We find that the relative error defined as $(z_{\rm phot} - z_{\rm spec})/(1 + z_{\rm spec})$ has a zero mean (0.0005) and a very small deviation of 0.036 after

---

[5] The MIPS 24 μm robust detection rate by Ivison et al. (2007) is significantly higher than ours or by Pope et al. (2006), despite their much shallower data, and this analysis may be in error. Although the majority of radio-identified sources in Table 1 as well as by Pope et al. have a MIPS 24 μm counterpart, the MIPS 24 μm source density is also much higher than the radio, leading to a greater chance-coincidence and thus a higher *P* value in general.

[6] http://www2.iap.fr/pegase/
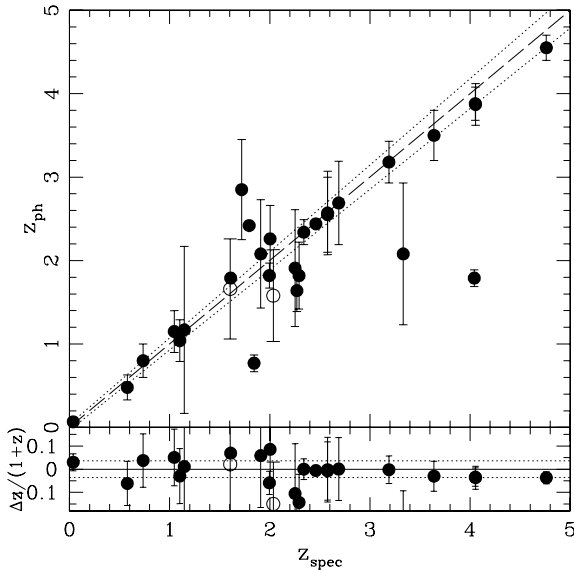
Figure 2. Comparison of spectroscopic and photometric redshifts for the candidate AzTEC counterpart sources in the GOODS-South (Table 1) field. Photometric redshifts based on the shallower MUSYC photometry (Gawiser et al. 2006) are shown in empty symbols. The two dotted curves represent redshift uncertainties of $\Delta z/(1 + z) = 0.036$ (see the text). The distribution of $\Delta z/(1 + z)$ is shown as a function of z in the bottom panel.

3σ clipping of the outliers. The fraction of outliers beyond 3σ is 9.9 per cent. The means of the relative errors have no significant offset from zero at all redshift bins, especially for our interested range of $1 < z < 5$. The demonstrated accuracy of our photo-z estimation is sufficient to justify a statistical study of the physical properties of our selected galaxies. Derived photometric redshifts of the AzTEC counterpart candidates are listed as z_{opt} in Table 3. A blank entry notes that the optical counterpart is undetected or too faint.

Physical properties (stellar mass, SFR, dust reddening) of the galaxies are measured by fitting the observed SEDs with the CB09 (Charlot & Bruzual, in preparation) theoretical stellar population synthesis models. The Salpeter initial mass function (IMF) with a lower and an upper mass cut-off of 0.1 and $100 \, M_\odot$ are adopted.[7] The galaxy redshift is fixed to its z_{spec} or z_{opt} in this step. A regular grid of models spanning a wide range of $E(B - V)$, star formation history (characterized by duration τ and age) and metallicity are examined. We apply the Calzetti law (Calzetti et al. 2000) for the internal dust extinction correction and follow the method described by Madau (1995) to account for the intergalactic medium opacity. The χ^2 value for each SED model fitting is computed as

$$\chi^2 = \Sigma_i \frac{(F_{obs,i} - \alpha F_{model,i})^2}{\sigma_i^2}, \quad (2)$$

where $F_{obs,i}$, $F_{model,i}$ and σ_i are the observed flux, model flux and observational uncertainty in the ith band. The normalization factor α is equal to stellar mass if $F_{model,i}$ is normalized to $1 \, M_\odot$ in our precomputed data base. The model with the smallest χ^2 is considered the best-fitting model, and its parameters are used to compute the stellar mass and SFR SFR$_{UV}$ – see Table 3.

We estimate the systematic uncertainties in the derived quantities using simulations. We generate theoretical SED templates with

[7] Adopting the Chabrier or Krupa IMF will lower the derived M_* and SFR by a factor of 1.7 – see Salimbeni et al. (2009).

different redshift, stellar mass, SFR, age and dust extinction. In each band, we randomly draw a photometric uncertainty from the error distribution of all sources with the same magnitude from the GOODS parent photometric catalogue and perturb the photometry of the template using a Gaussian random deviation with variance equal to the drawn photometric uncertainty. These steps are repeated 100 times for each template in each band to generate mock SEDs. Our SED-fitting code is applied to these mock SEDs to derive the systematic uncertainties in the derived quantities. If redshift and IMF are known, a typical uncertainty in stellar mass from the SED fitting is about 0.1–0.2 dex for all stellar masses. The uncertainty in SFR is about 0.1 dex for SFR $> 100 \, M_\odot \, yr^{-1}$. If a photo-$z$ is used, a typical redshift error of $\delta z/(1 + z) = 0.05$ translates to a 0.2 dex error in M_* and SFR. Excluding the uncertainty in the IMF, the overall typical uncertainties in M_* and SFR are 0.3 and 0.5 dex, respectively.

3.2 IR/mm/radio SED analysis

We derive an independent estimate of photometric redshift, IR luminosity and dust-obscured SFR (SFR$_{IR}$) by analysing the observed IR/mm/radio part of the SED. First, a photometric redshift is derived using an updated version of the photo-z analysis method described by Carilli & Yun (1999). Noting a remarkably tight correlation between radio and FIR luminosity for all star-forming galaxies (see review by Condon 1992) and the rapid change in the observed flux density ratio between the $850 \, \mu m$ band and the 20 cm radio continuum with redshift, Carilli & Yun (1999) proposed this observed flux density ratio as a robust redshift indicator. The success of this method rests on the fact that the Rayleigh–Jeans (R–J) part of the dust spectrum rises rapidly with frequency as $S \propto \nu^{3-4}$ while the radio part of the spectrum falls as $S \propto \nu^{-0.75}$, leading to more than two orders of magnitudes change in the observed flux density ratio between $z = 0$ and $z \geq 2$.

Subsequent analyses by Hughes et al. (2002) and Aretxaga et al. (2003) have shown that incorporating additional photometric measurements in the FIR to radio bands can improve the redshift estimate, but all of these methods are fundamentally limited by the intrinsic variation in the SED, arising from variations in the nature of the energy source and geometry of dust distribution. To improve the accuracy of the derived redshift and its uncertainty, we adopted a three times larger set of SED templates, adding 34 new sources with two or more photometry measurements in the R–J part ($150 < \lambda < 1500 \, \mu m$) of the dust SED and at least one radio continuum measurement, mostly from the new study by Clements, Dunne & Eales (2010). We opted to use empirical templates of observed SEDs rather than a library of theoretical templates because there is growing evidence, such as the tightness of the radio–IR correlation, suggesting that nature favours a certain subset of SEDs.

Another important addition is the use of Monte Carlo simulations to improve the handling of measurement errors, noise bias and the template variations. A notable outcome is that the derived redshift uncertainties, listed in Table 3, are asymmetric about the mean millimetre-to-radio photometric redshift (z_{MR}). Citing the flattening of the IR part of the SED with increasing redshift, Carilli & Yun (2000) have previously noted the asymmetry in the scatter of the 'mean galaxy model', but *in the opposite sense* from the uncertainties in the derived z_{MR}. This actually makes sense since the asymmetry in the mean template and the uncertainty in the derived z_{MR} should be in the opposite sense. This comparison thus shows that the common practice of quoting the redshift uncertainty using the (sub)mm–radio spectral index method based on the scatter in

Table 3. Redshifts and derived properties of the AzTEC GOODS-South sources.

AzTEC ID	z_{spec}^{a}	z_{opt}^{b}	log M_{*} ($M_{\odot}$)	SFR$_{\mathrm{UV}}$ ($M_{\odot}$ yr^{-1})	z_{MR}^{c}	SFR$_{\mathrm{IR}}$ ($M_{\odot}$ yr^{-1})
GS1a	...	2.96 ± 0.45	11.24	94	$3.56_{-1.20}^{+0.66}$	439
GS2.1a	...	2.13 ± 0.60	9.81	234	$3.20_{-1.10}^{+0.60}$	500
GS3a	...	...	...	...	$3.09_{-1.11}^{+0.55}$	
GS4a	...	3.37 ± 0.25	10.87	75	$3.53_{-1.27}^{+0.57}$	416
GS5a	1.599	1.66 ± 0.60	11.15	1632	$2.03_{-0.73}^{+0.37}$	646
GS6a	...	2.47 ± 0.65	11.37	37	$2.78_{-0.98}^{+0.60}$	220
GS7a	2.676	...	...	...	$2.56_{-0.92}^{+0.52}$	638
GS8a	2.252	1.91 ± 0.70	11.04	1553	$2.11_{-0.73}^{+0.41}$	466
GS9a	...	3.49 ± 0.35	11.01	285	$1.98_{-0.74}^{+0.38}$	
GS10a	2.035	1.58 ± 0.55	11.27	1555	$2.03_{-0.75}^{+0.41}$	350
GS11a	...	...	...	...	$2.50_{-0.88}^{+0.52}$	
GS12a	4.762	4.55 ± 0.15	11.28	87	$3.28_{-1.26}^{+0.70}$	803
GS13a	...	2.28 ± 0.90	10.20	3172	$2.92_{-1.10}^{+0.58}$	250
GS14a	3.640	3.50 ± 0.30	9.36	459	>3.0	600
GS15a	...	3.01 ± 0.45	10.00	1024	$3.23_{-1.13}^{+0.67}$	416
GS16a	1.719	2.85 ± 0.60	9.33	114	$2.67_{-0.95}^{+0.55}$	200
GS17a	...	1.01 ± 0.10	9.67	3.4	$2.94_{-1.08}^{+0.44}$	
GS17b	...	3.11 ± 0.20	11.41	14	>3.1	330
GS18a	...	...	...	...	$3.00_{-1.14}^{+0.56}$	
GS19a	...	1.83 ± 0.35	10.93	99	$2.74_{-1.04}^{+0.52}$	200
GS20a	0.037	0.069 ± 0.038	9.52	339	$0.57_{-0.41}^{+0.17}$	0.9
GS21a	1.910	2.08 ± 0.65	10.77	295	$2.28_{-0.90}^{+0.40}$	322
GS22a	1.794	2.42 ± 0.05	...	...	$2.39_{-0.93}^{+0.51}$	204
GS23a	...	...	...	...	$2.77_{-1.07}^{+0.47}$	
GS23b	2.277	1.64 ± 0.25	11.35	33	$2.36_{-0.90}^{+0.44}$	393
GS24a	...	1.94 ± 0.50	9.37	130	$3.04_{-1.10}^{+0.74}$	200
GS25a	2.292	1.82 ± 0.40	10.11	467	$1.52_{-0.68}^{+0.32}$	300
GS26a	...	3.64 ± 0.15	9.61	47	>2.6	150
GS27a	2.577	2.55 ± 0.45	10.02	383	$2.47_{-0.99}^{+0.57}$	322
GS28a	...	3.29 ± 0.65	9.95	1140	>2.6	177
GS29a	0.577	0.48 ± 0.15	10.45	4.0	>2.6	
GS29b	2.340	2.34 ± 0.15	10.36	75	>2.6	200
GS30a	...	1.51 ± 0.25	11.02	6.0	$2.29_{-0.88}^{+0.56}$	182
GS31a	1.843	0.77 ± 0.10	11.96	0.3	$2.68_{-1.00}^{+0.66}$	222
GS33a	...	2.45 ± 0.15	10.08	6.0	$2.46_{-0.96}^{+0.60}$	200
GS35a	...	2.96 ± 0.35	10.74	127	$2.27_{-0.91}^{+0.53}$	508
GS37c	...	...	...	...	>2.6	
GS39a	...	...	...	...	$2.01_{-0.85}^{+0.51}$	
GS42a	...	2.37 ± 0.15	9.56	4.1	>4.5	
GS43a	...	...	...	...	>4.0	
GS45b	...	2.07 ± 0.25	10.20	12	>3.4	
GS45c	...	2.91 ± 0.35	10.46	156	>3.4	
GS46a	...	1.67 ± 0.10	10.47	11	>3.5	
GS47a	...	...	...	...	$2.59_{-0.95}^{+0.55}$	

$^{a}z_{\mathrm{spec}}$ is a spectroscopic redshift. See Section A for the individual references.
$^{b}z_{\mathrm{opt}}$ is a photometric redshift derived from the analysis of the optical/NIR SED – see Section 3.1. $^{c}z_{\mathrm{rm}}$ is a new photometric redshift derived from the radio and AzTEC 1100 μm photometry – see Section 3.2. The listed uncertainty corresponds to a redshift range that includes 68 per cent of acceptable fits.
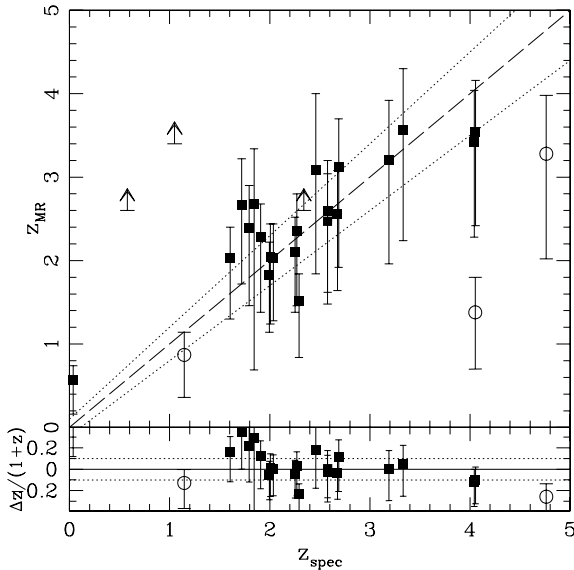
Figure 3. Comparison of spectroscopic and millimetre-to-radio (MR) photometric redshifts for the AzTEC sources with a robust counterpart in the GOODS-South (Table 1) and GOODS-North (Chapin et al. 2009) fields. Three objects with clear evidence for AGN activity are identified as empty circles. The two dotted curves represent redshift uncertainties of $\Delta z/(1 + z) = 0.10$. The distribution of $\Delta z/(1 + z)$ is shown as a function of z in the bottom panel.

the Carilli & Yun template (e.g. Aretxaga et al. 2007; Dannerbauer, Walter & Morrison 2008; Chapin et al. 2009) is in error.

The derived z_{MR} is in good agreement with z_{spec} in most cases as shown in Fig. 3 with $\Delta z/(1 + z) \sim 0.1$. This is not surprising given that the well-known radio–FIR correlation appears to hold among high-redshift IR-selected galaxies (see Ivison et al. 2010; Lacki & Thompson 2010). This estimator may be more accurate for starburst-dominated SMGs since two outliers at $z = 4.05$ and 4.76 are known AGN, and a similar 'radio-excess' due to an AGN contribution in the radio wavelength has been previously seen among other high-redshift quasi-stellar objects (QSOs; Yun et al. 2002; Yun & Carilli 2002). In some cases (e.g. GS2.2a, GS29a) the derived z_{MR} is completely inconsistent with their z_{spec}, primarily because of their radio non-detection. Given that the radio–FIR correlation holds for all other objects, a likely explanation is that their optical counterparts are misidentified, as is expected to happen in a small fraction (≤ 5 per cent) of cases (see Section 2.1).

Once the redshift of an AzTEC counterpart is determined, its IR luminosity L_{IR} can be estimated by adopting an SED template most consistent with the observed FIR/mm/radio photometry data. For the ease of a direct comparison with optically derived SFR_{UV}, we fix the redshift of each source to z_{spec} or z_{opt}. Then we use this L_{IR} to derive a dust-obscured SFR (SFR_{IR} – e.g. Kennicutt 1998). We adopt a set of theoretical SED templates for an ensemble of giant molecular clouds centrally illuminated by young star clusters by Efstathiou, Rowan-Robinson & Siebenmorgen (2000) that are shown to provide a good fit to a wide range of IR-selected sources at different redshifts (e.g. Efstathiou & Rowan-Robinson 2003; Clements et al. 2008; Rowan-Robinson 2010). SFRs derived from the IR SED fitting, SFR_{IR}, are computed directly from the best-fitting model star formation history (also assuming the Salpeter IMF) and are summarized in the last column of Table 3. Note that z_{opt} and z_{MR} do not always agree well, particularly for the cases where the counterpart is not secure.

Therefore SFR_{IR} is derived primarily for the securely identified AzTEC sources with a z_{spec} or a well determined z_{opt} only.

4 REDSHIFT DISTRIBUTION OF AzTEC–GOODS SOURCES

4.1 Derived redshift distribution

The deep multiwavelength data and the extensive spectroscopic redshift surveys covering the two GOODS fields offer the best opportunity to identify millimetre- and submillimetre-bright galaxies and to construct the most complete redshift distribution yet. By utilizing the analysis of AzTEC sources in both GOODS fields discussed in Section 3, we now have the opportunity to augment our understanding of the SMG redshift distribution with improved statistics.

In Figs 4 and 5, we show the redshift distributions for the robust AzTEC counterparts in both GOODS fields. We use spectroscopic redshifts when available (22 robustly identified sources) and photometric redshifts otherwise, and we plot separately the distributions determined using z_{opt} and z_{MR} in both figures. The redshift distributions based on optical photo-z (z_{opt}) and millimetric photo-z (z_{MR}) are qualitatively in a good agreement with each other, while the two methods are each subject to potentially significant systematic uncertainties. These redshift distributions show that 80 per cent of sources are at $z \gtrsim 2$, with 60 per cent just within the redshift range between $2.0 \lesssim z \lesssim 3.3$. The relatively small number of robust counterparts with only a lower redshift limit (nine out of 74) assures that the median value of $z_{med} \approx 2.6$ is a robust estimate. In comparison, using a different redshift estimator and analysing the properties of 29 AzTEC sources in the GOODS-North field only, Chapin et al. (2009) derived a median redshift of $z = 2.7$, in good agreement.

The asymmetric redshift distribution of the AzTEC sources in the two GOODS fields shown in Figs 4 and 5 can be described
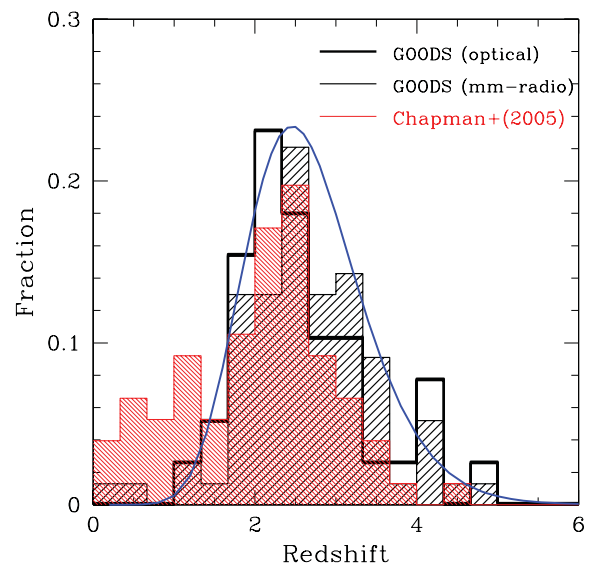
Figure 4. Redshift distributions of AzTEC sources in both GOODS fields based on the optical photo-z (z_{opt}, $N = 38$; blank histogram) and the millimetric photo-z (z_{MR}, $N = 74$; hatched histogram) are compared with that of the 76 radio-identified SCUBA sources with spectroscopic redshifts by Chapman et al. (2005, shaded histogram). The solid blue curve shown is a lognormal distribution as a function of $(1 + z)$ with a mean redshift of $z_{\mu m} = 2.6$ and $\sigma = 0.2$.
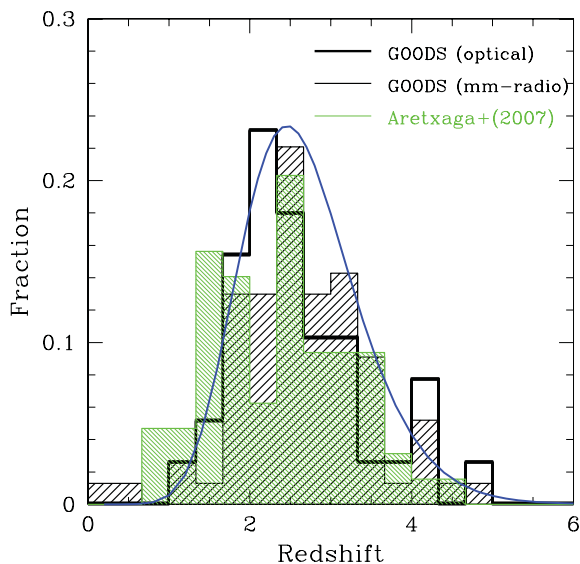
Figure 5. Redshift distribution of AzTEC sources in both GOODS fields based on the optical photo-z (z_{opt}; blank histogram) and the millimetric photo-z (z_{MR}; hatched histogram) are compared with that of the 64 robustly detected 850 μm sources in SHADES survey by Aretxaga et al. (2007, shaded histogram). Because of the shallow radio data in the Subaru/*XMM* Deep Field (SXDF), only the Lockman Hole sources are included for the Aretxaga et al. SHADES redshift distribution. The solid blue curve shown is a lognormal distribution as a function of $(1 + z)$ with a mean redshift of $z_{\mu m} = 2.6$ and $\sigma = 0.2$.

reasonably well as a lognormal distribution of the form

$$f(z) = \frac{1}{(1 + z)\sigma\sqrt{2\pi}} e^{-[\ln(1+z)-\ln(1+z_{\mu m})]^2/2\sigma^2}.$$

The solid curve shown in both figures corresponds to a lognormal distribution with $z_{\mu m} = 2.6$ and $\sigma = 0.2$ in $\ln(1 + z)$. No attempt is made to derive the best-fitting values of $z_{\mu m}$ and σ since some of the redshifts are only lower limits. Nevertheless, these nominal parameters simultaneously describe the rapid drop-off on the low-z side and the long tail on the high-z side.

4.2 Comparison with previous studies

The redshift distribution of the SMG population (and thus their cosmic evolution) is still poorly understood. A comparison of the redshift distribution derived from the AzTEC GOODS survey sources and those of previous studies further illustrates this point. A comparison of the AzTEC sources in the two GOODS fields with that of the radio-selected SCUBA 850 μm sources by Chapman et al. (2005, Fig. 4) gives an immediate impression that the two redshift distributions are substantially different. In particular, the population of $z \leq 1.5$ sources present in the Chapman sample is missing in our sample, while the AzTEC–GOODS sample shows a broader higher redshift tail. It is important to understand the underlying causes of this difference since many studies have assumed that the redshift distribution derived by Chapman et al. is consistent with that of the SMG population as a whole (e.g. Cooray et al. 2010; Davé et al. 2010; Narayanan et al. 2010a; Vieira et al. 2010; Almeida, Baugh & Lacey 2011; Williams et al. 2011). As noted by Chapman et al. and further discussed below (Section 4.3), these differences may be rooted in the use of radio selection for defining the Chapman sample.

Another insightful comparison is made in Fig. 5 by examining the redshift distribution of the GOODS–AzTEC sources with the photometric redshifts of the 64 robustly detected 850 μm sources in the SHADES survey by Aretxaga et al. (2007). The Aretxaga et al. redshift distribution is also largely missing the low-z population, and the agreement with our redshift distribution is better. If we take into account that 11 out 64 redshifts by Aretxaga et al. are only lower limits with $z_{lim} \leq 1.5$, the redshift distribution for the AzTEC–GOODS and the SHADES Lockman Hole sources is in fact very good.

A more quantitative comparison of the derived redshift distributions is made using the Astronomy Survival Analysis (ASURV; Feigelson & Nelson 1985) package, which properly takes into account lower redshift limits.[8] As summarized in Table 4, the only pairs of redshift distributions showing non-negligible probability of being drawn from the same parent sample are between z_{MR} and z_{opt} and between z_{MR} and the photometric redshifts of the 850 μm sources in the SHADES survey by Aretxaga et al. (2007). On the other hand, both Gehan's generalized Wilcoxon test and the logrank test suggest that there is *at most* 3 per cent probability that the Chapman et al. redshift distribution is consistent with those of the GOODS–AzTEC sources or the SHADES 850 μm sources in the Lockman Hole region as analysed by Aretxaga et al. The Kaplan–Meier estimator gives the mean redshifts of $\langle z_{MR} \rangle = 2.689 \pm 0.112$ and $\langle z_{opt} \rangle = 2.516 \pm 0.129$. The inclusion of lower limits in the redshift for radio-undetected sources appears to be the primary difference for these estimates (see below). The mean redshift of the Aretxaga et al. sample is 2.695 ± 0.098, in a good agreement with that of $\langle z_{MR} \rangle$. In contrast, the mean redshift of the Chapman et al. sample is 2.000 ± 0.104, significantly lower.

The robustness of these analyses is further tested by conducting a Kolmogorov–Smirnov (K–S) test for the same pairs of redshift distributions but excluding lower redshift limits. Again, as summarized in Table 5, the hypothesis that the Chapman et al. redshift distribution is identical to the z_{MR} or Aretxaga et al. redshift distribution can be rejected with better than 98 per cent confidence while the same hypothesis for the other combinations of pairs cannot be rejected. Nevertheless, both the survival analysis and the K–S tests are giving us consistent results in that the Chapman redshift distribution is substantially different from the SMG redshift distribution derived by us using the GOODS–AzTEC sources and that of the Lockman Hole 850 μm sources in SHADES survey by Aretxaga et al.

4.3 Wavelength-dependent selection bias

As discussed in some detail by Chapman et al. (2005), their radio selection for a spectroscopic redshift survey is intrinsically biased toward low-redshift galaxies and those with cold dust temperature. The observed radio flux density suffers from a strong *positive k-*correction, fading faster with increasing redshift than expected from the inverse square law. This means the majority of faint ($S_{1.4\,GHz} \geq$ 30–40 μJy) radio sources are at $z \leq 1$ and only extremely luminous ($P_{1.4\,GHz} \geq 10^{24}\,W\,Hz^{-1}$) radio sources are detectable at $z > 2$ (e.g. Smolcic et al. 2008; Strazzullo et al. 2010). Chapman et al. discussed this foreground confusion and removed about 10 per cent of the sources from their sample, but the significant number of $z \leq$ 1.5 sources remaining in their sample (but unseen in our sample

---

[8] This analysis assumes that the censored data follow a similar distribution to that of the measured population.

Table 4. Comparison of mean redshifts and probabilities that two redshift distributions are drawn from the same parent distribution derived using the ASURV, as described in Section 4. The first row shows the number of redshift data points (N_d) and lower limits (N_l) used. The second row shows the Kaplan–Meier estimator for the mean and standard deviation of the redshift distribution. The last three rows show, first, the Gehan's Generalized Wilcoxon test probability for each pair, and second, the Logrank test probability.

	z_{opt}	z_{MR}	Chapman05	Aretxaga07
(N_d, N_l)	(38, 0)	(74, 9)	(76, 0)	(64, 23)
$\langle z \rangle$	2.516 ± 0.129	2.689 ± 0.112	2.000 ± 0.104	2.695 ± 0.098
z_{opt}	–	0.19/0.21	0.030/0.026	0.06/0.30
z_{MR}		–	0.0001/0.0001	0.51/0.85
Chapman05			–	0.0000/0.0001

Table 5. The K–S test probability that two redshift distributions are drawn from the same distribution, derived using the cumulative distributions of the same samples as in Table 4 but excluding lower limits.

	z_{opt}	z_{MR}	Chapman05	Aretxaga07
z_{opt}	–	0.845	0.250	0.098
z_{MR}		–	0.014	0.362
Chapman05			–	0.0014

and Aretxaga et al. sample) suggests that they underestimated the foreground confusion. Chapman et al. also considered the effects of rapidly declining sensitivity of the radio data with redshift, but they focused mainly on the dust temperature dependence on radio–IR correlation, assuming that the majority of sources undetected in the radio bands are at the same redshifts as those detected. The significant high-redshift ($z > 3$) tail for the AzTEC and SCUBA sources seen in Figs 4 and 5 suggests that the highest redshift sources are missing in radio-selected samples like Chapman et al. because the depth of the available radio data is not sufficient to detect most SMGs at $z \gtrsim 3$. Mapping the true redshift distributions of SMGs will require future complete spectroscopic redshift surveys using instruments such as the Redshift Search Receiver (Erickson et al. 2007) on the Large Millimeter Telescope or the Atacama Large Millimeter Array.

These discussions of k-correction and dust temperature raise another important question as whether SMGs selected at 850 and 1100 μm [and as a natural extension at 250–500 μm by the *Herschel*/Spectral and Photometric Imaging Receiver (SPIRE) instrument] are systematically different. Since the dust peak passes through these bands at different redshifts, some wavelength-dependent selection effects are expected. For example, identification of 'drop-out' objects in these bands has been suggested as a means to identify the highest redshift SMG population (see Pope & Chary 2010). When we noted the low rate of coincidence between the LABOCA 870 μm sources and our AzTEC survey initially (see Section 2.2), this wavelength-dependent selection bias was one of the causes we explored, although we eventually concluded that the low completeness of the both surveys is the primary cause. The general agreement between the redshift distributions of SCUBA 850 μm selected sources by Aretxaga et al. (2007) and the AzTEC 1100 μm sources seen in Fig. 5 suggest that the redshift distribution and SEDs of the SMG population are such that the sources identified at these two wavelengths are indeed similar.

5 OPTICAL AND IR LUMINOSITY AND STAR FORMATION

5.1 Not all SMGs are faint and red in the rest-frame UV and optical bands

Although SMGs are a recently recognized class of galaxies, their relatively high density (0.1–0.5 arcmin^{-2}) and high luminosity ($L_{IR} \gtrsim 10^{12-13}$ L$_\odot$) suggest that they represent a significant component of the general galaxy population and should play an important role in the overall galaxy evolution scenario. In the 'down-sizing' scenario (Cowie et al. 1996), more massive galaxies are thought to have been assembled earlier in cosmic history, presumably with a higher SFR. Luminous infrared galaxies (LIRGs) and ultraluminous infrared galaxies (ULIRGs) with SFR $\gtrsim 10$–100 M$_\odot$ yr^{-1} are the dominant contributor to the cosmic star formation history at $z \sim 1$ (Le Floc'h et al. 2005; Magnelli et al. 2009, 2011), and a significant contribution by SMGs with SFR of $\gtrsim 10^{2-3}$ M$_\odot$ yr^{-1} would represent a natural progression at $z > 1$. Massive galaxies with stellar mass $M_* \gtrsim 10^{11}$ M$_\odot$ are thought to be already in place by $z \sim 2$ (van Dokkum et al. 2008). Galaxies with even higher SFR might be found at higher redshifts.

What would these SMGs look like in the rest-frame UV and optical bands? And how do they fit into the larger population of high-redshift galaxies identified in those more traditional bands? Optical/UV size, morphology and luminosity could provide an important test for their origin as merger-driven starbursts (e.g. Narayanan et al. 2010a) or large disc systems (Efstathiou & Rowan-Robinson 2003; Kaviani, Haehnelt & Kauffmann 2003; Hayward et al. 2011) fuelled by a high rate of cosmological gas accretion (Keres et al. 2005; Davé et al. 2010). Early studies in the optical and NIR suggested a diverse population of bright, modest redshift ($z \lesssim 1$) and faint, high-redshift ($z \sim 2$) galaxies, as reported by Lilly et al. (1999), Barger et al. (1999), Barger, Cowie & Richards (2000), Ivison et al. (2000), Fox et al. (2002) and Ivison et al. (2002). However, high-resolution interferometric imaging studies at millimetre wavelengths (Bertoldi et al. 2000; Frayer et al. 2000; Lutz et al. 2001; Dannerbauer et al. 2002) have shown that the SMG counterparts are often undetected in the optical bands. A study of a large sample of radio-identified SMGs using deeper optical data by Chapman et al. (2001) showed that their counterparts are indeed quite faint ($I > 25$), and Chapman et al. concluded that dust obscuration makes these galaxies essentially invisible in the ultraviolet bands. This conclusion is not universally accepted, however – see Ivison et al. (2002). Interestingly, Chapman et al. (2005) targeted their own sample for spectroscopy using the Keck telescopes and successfully obtained
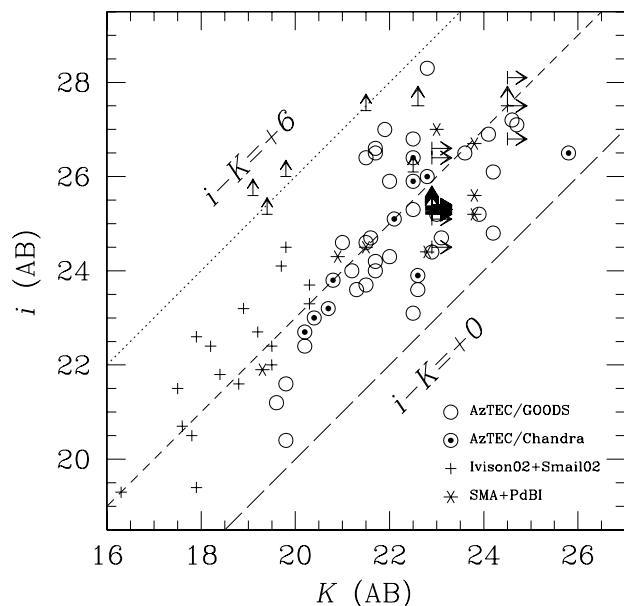
Figure 6. Measured K-band versus i-band magnitudes of the robustly identified AzTEC counterpart sources (circles). Lines of constant colours with $i - K = +0$, $+3$ and $+6$ are shown. Circles with filled dots are AzTEC sources with *Chandra* X-ray detection in the GOODS-North and GOODS-South fields while empty circles are the sources without X-ray detection. Crosses represent the 17 'securely' identified counterparts to the SCUBA 8-mJy survey (Ivison et al. 2002) and the SCUBA Lens Survey (Smail et al. 2002) sources. Asterisks are SMGs securely identified by interferometric measurements at millimetre and submillimetre wavelengths (Iono et al. 2006; Younger et al. 2007, 2008, 2009; Hatsukade et al. 2010).

emission and absorption line redshifts for about 50 per cent of their sample.

A major motivation for this work is to clear up the confusion about the rest-frame optical and UV properties of SMGs by examining a robustly identified large sample with significantly improved statistics by taking advantage of the deep multiwavelength data available in the GOODS fields. In Fig. 6 we examine the rest-frame UV and optical properties of SMGs by plotting the measured i- and K-band photometry of robustly identified AzTEC sources in the GOODS-South field (this work) and the GOODS-North field (Perera et al. 2008; Chapin et al. 2009) – also see Pope et al. (2006). Sources identified by the SCUBA 8-mJy survey (Ivison et al. 2002; Smail et al. 2004) and the SCUBA Lens Survey (Smail et al. 2002) are also shown for comparison. A remarkable result is that SMGs span a very broad range of brightness in both i- and K band (rest frame $\lambda = 240$ and 630 nm at $z = 2.5$), spreading over 10 mag, or a factor of 10^4 in flux density. The apparent brightness of the AzTEC–GOODS sources by themselves span over 7 mag with a median brightness of $i = 25.3$ and $K = 22.6$ when the upper limits are taken into account. Although there is some overlap with the sources identified by the earlier SCUBA 8-mJy survey and the SCUBA Lens Survey, the *AzTEC–GOODS counterpart sources are systematically fainter by ~3 mag on average*. Because earlier SMG identification studies relied on K-band data too shallow to detect the majority of the AzTEC counterparts in the GOODS-South field, this means earlier works may have missed or misidentified the counterparts in many cases. The few but highly secure SMG counterparts identified recently using deeper optical and NIR data and high-resolution interferometric imaging in the millimetre and submillimetre bands (shown as asterisks – Iono et al. 2006; Wang et al. 2007b, 2011; Younger

et al. 2007, 2008, 2009; Hatsukade et al. 2010) have a brightness distribution more closely matching that of the AzTEC sources in both GOODS fields.

We also deduce from the observed scatter in Fig. 6 that there is at least a factor of 10 variation in the intrinsic rest-frame optical luminosity among these SMGs. When viewed together with SCUBA-detected sources, these SMGs form a broad colour track centred roughly around the $i - K = +3$ line (short dashed line), which is quite red compared with field galaxies. Some sources show a relatively flat colour ($i - K = +1$) while there are others with extremely faint i-band upper limits and colours redder than $i - K = +6$. The scatter about the mean relation appears to increase at $K \gtrsim 22$, but the source density is also higher at these fainter magnitudes. The full range of the scatter perpendicular to the mean relation is about 4 mag in colour. This large spread in colour substantiates the earlier suggestion that optical properties of SMGs are quite diverse (e.g. Ivison et al. 2000, 2002). However, it cannot fully account for the up to ~10 mag spread in their apparent brightness as a population. In other words, there is an additional factor of $\gtrsim 100$ variation (or $\gtrsim 5$ mag) in the apparent brightness of SMGs on top of the apparent differences in colour, which may be due to variations in SED and extinction. Given their extreme luminosity, the SMG phase likely represents a brief, special moment during the rapid mass build-up phase (e.g. Narayanan et al. 2010a; Hayward et al. 2011). If the majority of SMGs are seen in the redshift range between 1.5 and 4.0 (see Section 4), then the spread in the luminosity distance can account for about a factor of 10 in the apparent brightness variation. Therefore, the remaining factor of $\gtrsim 10$ scatter in apparent brightness has to be accounted for by an intrinsic scatter in the rest-frame optical band luminosity.

In the broader context of understanding star-forming galaxies in the early universe, some of the AzTEC sources are bright in the rest-frame UV and optical bands and are already identified as star-forming galaxies by past surveys. For example, about 30 per cent are bright enough in the optical and NIR bands to be classified as 'BzK' galaxies (Daddi et al. 2004) using the existing photometry – see discussions in Appendix A. Some of the $z \sim 4$ SMGs have also been identified as 'Lyman break galaxies' (see Capak et al. 2008). On the other hand, the majority of the AzTEC GOODS sources are too faint and red to have been identified in previous surveys of star-forming galaxies and are likely to be entirely missed in the current accounting of the cosmic star formation history. Future millimetre wavelength surveys with higher angular resolution are needed to probe deeper into the lower flux density (and lower luminosity) regime in order to bridge these populations and obtain a complete census of star-forming galaxies.

5.2 SMGs as massive galaxies in a phase of rapid stellar mass build-up

5.2.1 Stellar luminosity of SMGs

One constant in the high-resolution interferometric millimetre and submillimetre observations of SMGs is the presence of a *Spitzer* IRAC counterpart in the 3.6–8.0 μm bands, and this is one of the key features we employ to identify AzTEC counterparts (see Section 2). A comparison of the apparent brightness in the 3.6 μm band (rest-frame optical or NIR) for the AzTEC counterparts and other K-band selected $z \sim 2$ star-forming galaxies with known spectroscopic redshifts in both GOODS fields is shown in Fig. 7(a). While there is some overlap between these two populations, the AzTEC counterparts are systematically brighter by $\gtrsim 1$ mag on average and
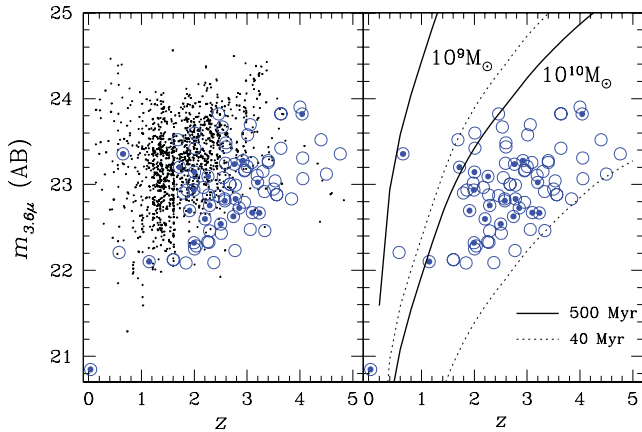
Figure 7. *Spitzer* IRAC 3.6 μm band 'Hubble diagram'. IRAC 3.6 μm band brightness ($m_{3.6\,\mu m}$) of the robust AzTEC counterparts is plotted as a function of redshift. Symbols are the same as in Fig. 6. Small dots in the left-hand panel are *K*-band selected star-forming galaxies with known spectroscopic redshifts in both GOODS fields. The apparent brightness of a 40 Myr starburst population with a stellar mass of 10^9 and 10^{10} M$_\odot$ is shown in dotted lines, while the same population after passively evolving for 500 Myr is shown in solid lines. An exponentially decaying starburst history with a 20 Myr e-folding time and solar metallicity is assumed for the models.

represent the most luminous galaxies at these redshifts. This intrinsically high luminosity in the rest-frame optical and NIR bands is clearly an important reason why these AzTEC sources are so readily detected by *Spitzer*.

Since AzTEC detection requires highly efficient dust processing of the UV radiation from young stars, the high inferred luminosity in the rest-frame optical/NIR bands seems surprising. After all, we just established in the previous section (Section 5.1) clear evidence for severe attenuation of UV radiation among many of these objects. A natural explanation for this apparent puzzle is found in the studies of the local ULIRG population. An imaging study of local ULIRGs in the near- and far-UV bands by Goldader et al. (2002) has shown that activity traced in the UV bands is distributed over kiloparsec scales and is heavily obscured, particularly in the regions of the most intense starburst activities. When observed at redshifts of $z \sim 2$ to ~ 4, these ULIRGs are expected to be extremely red and faint in the observed optical and NIR bands ($R - K = 4$–6, $K \approx 21$–24), similar to the observed values for the AzTEC sources shown in Fig. 6. At the same time, Chen, Lowenthal & Yun (2010) have shown that the stellar hosts of local ULIRGs are also extremely blue in rest-frame optical bands and are on average ~ 1 mag *brighter* than the field star-forming population, owing to distributed star formation activity and the high intrinsic luminosity of young stellar clusters. A *HST* NICMOS and ACS imaging study by Swinbank et al. (2010) has also found evidence for ongoing mergers and structured dust obscuration among $z \sim 2$ SMGs, further supporting the parallel in the observed source luminosity and structure between the local ULIRGs and high-*z* SMG population.

One cannot automatically conclude from their large observed luminosity that these SMGs are also the most massive galaxies at their observed epochs if their luminosity is powered by a large population of widely distributed young stellar clusters. The apparent 3.6 μm brightness of a single stellar population starburst model with a total accumulated stellar mass (M_*) of 10^9 and 10^{10} M$_\odot$ is shown in Fig. 7(b) for two different scenarios: 40 Myr (dotted lines) and 500 Myr (solid lines) after the initial burst. The observed brightnesses of AzTEC sources are well bounded by the 40 Myr old

starburst models with stellar masses of 10^9 and 10^{10} M$_\odot$, which are about *10 times smaller* than the stellar masses derived for the *K*-band selected star-forming galaxies shown in comparison ($M_* = 10^{10-11}$ M$_\odot$; Daddi et al. 2007). However, after just 500 Myr of passive evolution, the same starburst systems fade by ~ 2 mag at $z \sim 2$–4, bringing them back to a better agreement with the mass estimates for the *K*-band selected star-forming galaxies. Alternatively, accounting for the observed 3.6 μm band brightness of the AzTEC sources assuming a maturing stellar population would require stellar masses well in excess of 10^{11} M$_\odot$.

5.2.2 Stellar mass and star formation rate of SMGs

We can get a better handle on the stellar mass by modelling the observed rest-frame UV and optical SED as discussed in Section 3.1. The derived stellar masses from the modelling of the UV–optical SED, shown in Fig. 8, range between 10^9 and 10^{12} M$_\odot$. The majority of the derived stellar masses are between 1 and 30 times 10^{10} M$_\odot$, similar to those of the *K*-band selected massive star-forming galaxies at the same redshift, such as those discussed in Daddi et al. (2007). Similarly large stellar masses were found previously for SMGs (e.g. Dye et al. 2008; Tacconi et al. 2008; Daddi et al. 2009; Hainline et al. 2009; Michalowski, Hjorth & Watson 2010), and they are consistent with the idea that these submillimetre-bright galaxies are associated with the peak of the stellar mass function at $z = 2$–3.

Six out of 18 AzTEC counterparts with $M_* \geq 10^{11}$ M$_\odot$ are also X-ray sources detected in deep *Chandra* surveys. The frequency of the *Chandra* detected sources is about the same for the lower stellar mass galaxies (seven out of 25), and there is little evidence for any dependence on stellar mass. The low number of $z \geq 3$ sources detected by the 2–4 Ms *Chandra* surveys may reflect the limiting sensitivity of the X-ray data, and the observed X-ray fraction is
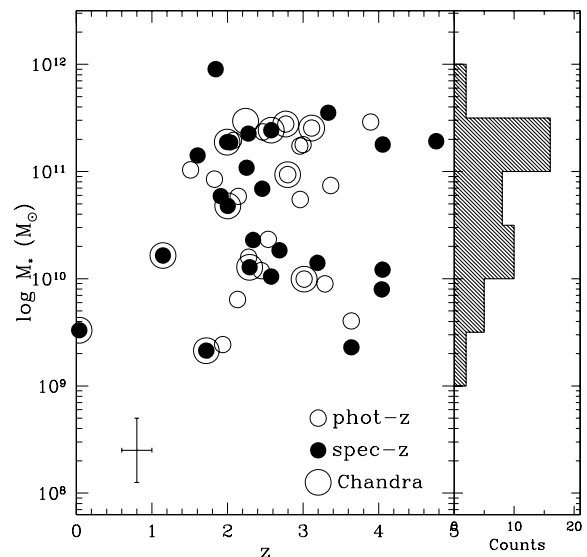
Figure 8. The stellar masses of AzTEC counterparts derived from optical and NIR photometry as a function of redshift. A histogram of stellar masses is shown in the right-hand panel. Sources with a spectroscopic redshift are shown as solid symbols, while the ones with a photometric redshift are shown as empty circles, and they represent similar ranges of stellar mass. Typical uncertainties for the M_* and photo-*z* estimates are shown on the bottom left-hand corner. Those detected by the *Chandra* in the X-ray are identified with a larger circle. Only GOODS TFIT catalogue sources with a proper stellar mass estimate are included.
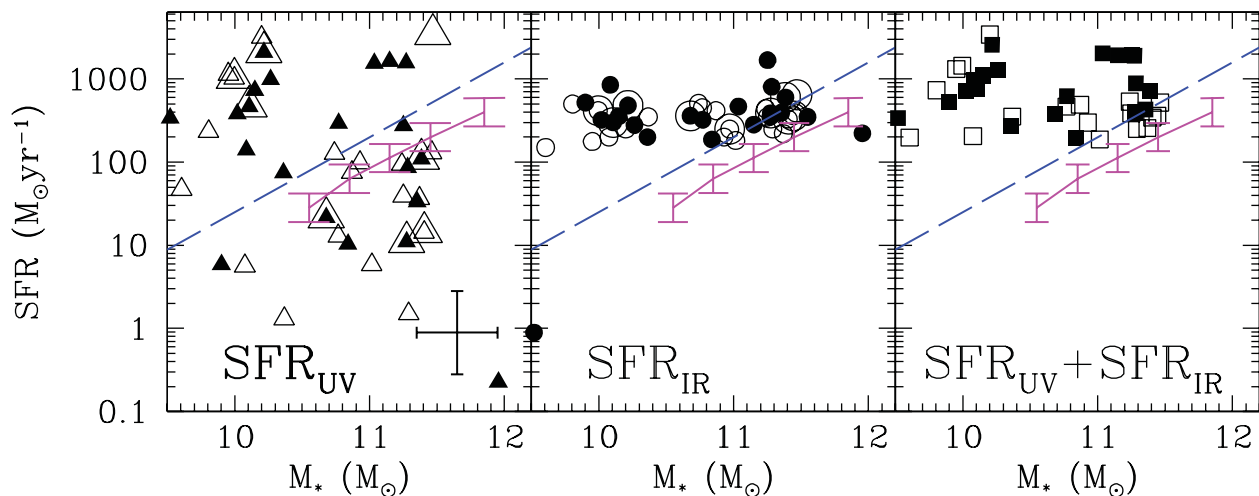
Figure 9. SFRs for AzTEC GOODS sources estimated from the rest-frame UV (SFR$_{UV}$) and IR (SFR$_{IR}$) as a function of stellar mass. Open and filled symbols represent photometric and spectroscopic redshifts, and those detected by the *Chandra* in the X-ray are identified with a larger symbol. A typical overall uncertainty for an object with photo-z is shown on the bottom right-hand corner of the left-hand panel. The mean SFR–M_* relation for the $z = 2.5$ model SMGs fuelled by cold flow (Davé et al. 2010) is shown by a solid line. Long dashed line is the observed mean SFR–M_* relation for the K-band selected galaxies (Daddi et al. 2007). The SMGs do not seem to follow either trend.

a lower limit. Given the poor statistics, it is difficult to conclude whether the presence of a luminous AGN is influencing the modelling of the rest-frame optical SEDs.

The rest-frame optical SED modelling also yields a UV-derived SFR (SFR$_{UV}$). The derived SFR$_{UV}$ for the AzTEC–GOODS sources cover a broad range: 1–2000 M$_\odot$ yr^{-1} – see the left-hand panel of Fig. 9. A surprising result is that the derived SFR$_{UV}$ is quite high, $\geq$100–1000 M$_\odot$ yr^{-1} for about 50 per cent of the cases. The observed SFR$_{UV}$ distribution is also nearly independent of stellar mass. The SFR$_{UV}$ distribution broadly overlaps the observed SFR–M_* relation for the K-band selected galaxies studied by Daddi et al. (2007, dashed line), but there is little evidence that these AzTEC sources follow the same SFR–M_* relation. The AzTEC–GOODS sources also do not follow the SFR–M_* relation predicted by the $z = 2.5$ model SMGs fuelled by cold flow accretion (Davé et al. 2010, solid line). Some of the galaxies with the highest SFR$_{UV}$ are detected in the X-ray by *Chandra*, raising the possibility that the UV light from the central AGN might contribute to these high values. However, not all *Chandra* detected sources are associated with a high SFR$_{UV}$, and neither the SFR$_{UV}$/SFR$_{IR}$ ratio nor the specific star formation rate (SSFR) discussed below offer any clear evidence to support this idea.

For comparison, IR-derived SFRs (SFR$_{IR}$) determined from modelling the IR SED are shown in the middle panel of Fig. 9. The SFR$_{IR}$ is uniformly high, $\geq$100–1000 M$_\odot$ yr^{-1}, with a much smaller scatter and completely independent of stellar mass. This is expected since these confusion-limited AzTEC surveys preferentially select sources with intrinsically large L_{IR}. We note that the 1.1 mm selection does not *guarantee* a high L_{IR} or SFR$_{IR}$ if cold dust ($T_d = 10$–20 K) emission dominates the millimetre spectrum. On the other hand, our SED modelling does not find any cold-dust-dominated sources with $L_{IR} < 10^{12}$ L$_\odot$. Since the IR luminosity accounts for the total amount of dust-processed UV radiation, a comparison of SFR$_{IR}$ with SFR$_{UV}$ should offer a crude measure of the geometry between the young stars and the obscuring dust. The large SFR$_{UV}$ derived for a large fraction of AzTEC–GOODS sources is particularly interesting in this regard, and this result may indicate that star formation activities and dust distribution in these SMGs are not as
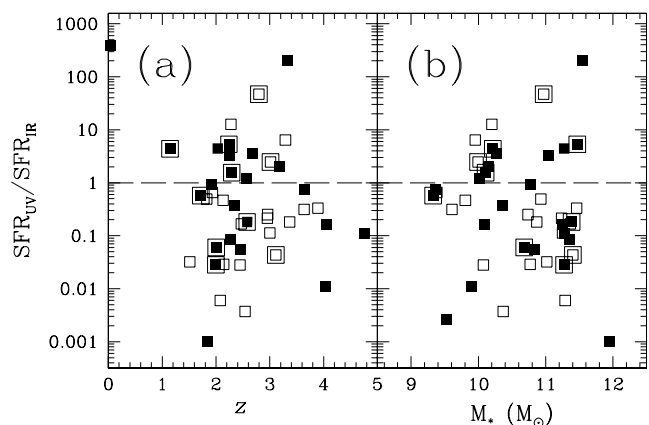
Figure 10. The ratio of SFR derived from the rest-frame UV (SFR$_{UV}$) and the rest-frame IR (SFR$_{IR}$) as a function of (a) redshift and (b) stellar mass (M_*). Galaxies with spec-z (photo-z) are shown in filled (empty) symbols, and those detected by the *Chandra* in the X-ray are identified with a larger square. The dashed line marks the SFR$_{UV}$ = SFR$_{IR}$ relation.

concentrated as in the local ULIRGs, where $L_{IR} \approx L_{bol}$ (see Sanders & Mirabel 1996).

To explore the relationship between SFR$_{UV}$ and SFR$_{IR}$ further, their ratios are plotted as a function of redshift and M_* in Fig. 10. This ratio varies widely from one source to another, spanning over five decades in total range, and it is independent of z and M_*. Finding a large number of sources with SFR$_{UV}$/SFR$_{IR} > 1$ is particularly puzzling for these galaxies with a large stellar mass. A misidentification of the counterparts is also a plausible explanation, but the observed distribution would require the failure of counterpart identification in a large fraction of cases. Either an underestimate of SFR$_{IR}$ or an overestimate of SFR$_{UV}$ (and possibly both) can provide an explanation, as the estimates of both SFR and M_* are subject to significant systematic uncertainties (e.g. see Maraston et al. 2010). If these galaxies represent young galaxies seen during their rapid mass build-up phase (see below), then the well-known mass–metallicity relation (Tremonti et al. 2004) and the attenuation

of UV light in the local universe may not be directly applicable. The presence of an X-ray source detected by *Chandra* is not correlated with the SFR_{UV}/SFR_{IR} ratio, and the presence of an X-ray emitting AGN does not seem to contribute directly to the derived SFR_{UV} in most cases.

5.2.3 Specific star formation rate and mass build-up history

Charting the star formation and stellar mass build-up history is one of the most powerful tests for galaxy evolution theories. For example, the emergence of red sequence galaxies that are massive and passively evolving around $z \sim 1$ and their increase in number with time are widely cited as important observational constraints that require additional complexities such as AGN feedback and 'dry' mergers (Bell et al. 2004, 2007; Faber et al. 2007). Statistical studies such as the Sloan Digital Sky Survey have shown that the bulk of stars now in massive galaxies formed at earlier epochs than stars in lower mass galaxies (e.g. Kauffmann et al. 2003), suggesting a strong link between galaxy mass and star formation history. A particularly useful quantity to examine in this regard is the SSFR (SFR per unit stellar mass; $SSFR \equiv SFR/M_*$). A systematic dependence of SSFR on galaxy mass and a rapid increase of SSFR with redshift have been established by several recent studies (Zheng et al. 2007; Damen et al. 2009). Given the large stellar masses ($M_* = [1–30] \times 10^{10}\,M_\odot$) and SFRs ($> 10^{2-3}\,M_\odot\,yr^{-1}$) for these $z = 2–4$ SMGs, examining their SSFR in the context of the observed trends with stellar mass and redshift may provide a valuable new insight into the physical mechanisms driving the SMG phenomenon and massive galaxy formation.

The computed SSFRs for the AzTEC–GOODS sources are shown in Fig. 11. An immediately noticeable trend is that the derived SSFRs are uniformly quite high, $SSFR \approx 1–100\,Gyr^{-1}$. Among the optically selected samples, galaxies with $SSFR \gtrsim 10–100\,Gyr^{-1}$ are generally associated lower stellar mass ($M_* \leq 10^{10}\,M_\odot$) galaxies undergoing a starburst episode. More massive galaxies in the local

universe are associated with one to two orders of magnitudes lower SSFR (Bauer et al. 2005; Feulner et al. 2005; Erb et al. 2006; Elbaz et al. 2007). The same trend also holds at higher redshifts as the K-band selected star-forming galaxies at $z \sim 2$ have on average SSFR $\approx 1\,Gyr^{-1}$ (Daddi et al. 2007), overlapping only at the bottom range of the SSFR associated with the AzTEC sources. Pannella et al. (2009) have also reported an average SSFR $\approx 5\,Gyr^{-1}$ and SFR $\approx 100\,M_\odot\,yr^{-1}$ for their $z \sim 2$ radio-identified star-forming galaxies with an average $M_* = 3 \times 10^{10}\,M_\odot$ at $z \sim 2$ (also see Dunne et al. 2009).

The SSFRs for the AzTEC–GOODS sources are significantly higher than those of similar stellar mass galaxies in the local Universe, and they appear to follow the same broad trend of rapidly increasing SSFR with redshift. The dotted line shown in Fig. 11 is the stellar mass-dependent SSFR evolution mapped by Damen et al. (2009) for massive galaxies with $M_* \geq 10^{11}\,M_\odot$, and it shows a rapid rise as SSFR $\propto (1 + z)^5$ between $z = 0$ and 2. The radio-derived SSFRs for star-forming galaxies with $M_* \sim 3 \times 10^{10}\,M_\odot$ derived by Pannella et al. (2009), shown in asterisks, extend this rapidly rising trend to $z \sim 2.5$. The AzTEC–GOODS sources extend this rise in SSFR further to $z \sim 4$, although there is significant scatter. As noted by Damen et al. and others, there is a mass dependence on the SSFR evolution, and the spread in M_* for the AzTEC sources likely contributes to some of the observed scatter.

The SSFRs derived for the AzTEC–GOODS sources provide the strongest evidence yet that SMGs are seen during the brief phase of rapid stellar mass build-up. The solid lines in Fig. 11 represent the inverse of the Hubble time, $1/t_H$: only galaxies with SSFRs above this line have sufficiently high SFRs to build up their current stellar masses within the Hubble time at their respective redshifts. Considering the SSFRs derived from fitting the FIR SEDs (right-hand panel of Fig. 11), all of the AzTEC–GOODS SMGs are located at or above this critical line. We cannot exclude the possibility that these SMGs are rejuvenated galaxies, undergoing another episode of extreme luminosity, but it would require an even earlier episode of rapid stellar mass build-up. Citing extremely high SFR and similar density, previous studies have made plausible arguments for identifying SMGs as progenitors of present day massive elliptical galaxies (e.g. Blain et al. 2004). Our new analysis of the SSFR allows us to demonstrate quantitatively that these SMGs are seen *during* a phase of rapid stellar mass build-up.

The absence of AzTEC sources with SSFR below the $1/t_H$ line in the right-hand panel of Fig. 11 is primarily the result of AzTEC survey depth – in fact, all existing confusion-limited surveys carried out with, e.g. AzTEC and *Herschel*, probe only the brightest end of the luminosity function. Much of the cosmic IR background (CIRB) is expected to arise from fainter sources below the confusion limit, and their number counts can offer an important constraint to the evolution model for SMGs (Granato et al. 2004; Baugh et al. 2005; Rowan-Robinson 2009). The location of the $1/t_H$ line in Fig. 11 leaves a fairly limited parameter space for a lower luminosity dust-obscured starburst population that can contribute significantly to the CIRB – e.g. SFR $\approx 20–100\,M_\odot\,yr^{-1}$ for a $(1–5) \times 10^{10}\,M_\odot$ galaxy at $z = 2$. A $z \gtrsim 2$ galaxy with $M_* \geq 10^{10-11}\,M_\odot$ can still appear with a SSFR below this $1/t_H$ line, but the presence of a large population of such galaxies would have an important consequence in that the formation epoch of those massive galaxies has to be pushed to a much earlier time. The decreasing t_H with redshift also requires an even larger SFR with increasing z, and in turn the submm/mm-detected fraction of galaxies with a stellar mass $M_* \geq 10^{10-11}\,M_\odot$ has to rise with increasing redshift. The high detection rate of optically selected $z \geq 4$ QSOs in the submm/mm continuum
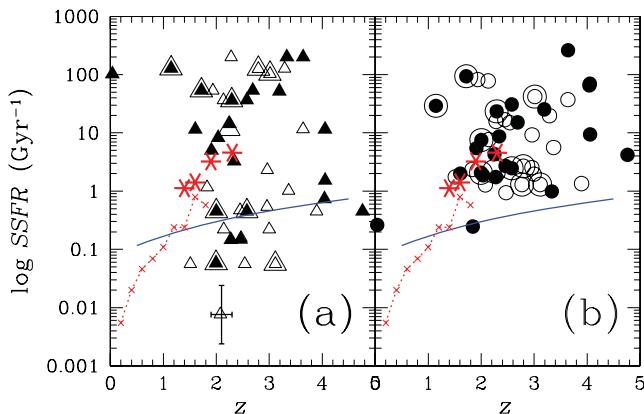

Figure 11. SSFR of AzTEC counterpart candidates derived from the (a) rest-frame UV and optical SED fitting and (b) far-IR SED fitting using Efstathiou et al. (2000) dusty starburst SED templates. Solid and empty symbols represent the sources with spectroscopic and photometric redshifts, respectively, and those detected by *Chandra* in the X-ray are identified with a larger symbol. A typical uncertainty is shown for one of the photo-z sources at the bottom of the left-hand panel. The asterisks represent the radio-derived SSFRs for star-forming galaxies with $M_* \sim 3 \times 10^{10}\,M_\odot$ derived by Pannella et al. (2009). The solid line represents the inverse of the Hubble time, and sources above this line are in a starburst mode. The dotted line connecting the crosses represents the average SSFR for massive galaxies with $M_* \geq 10^{11}\,M_\odot$ found by Damen et al. (2009).

(∼30 per cent; Carilli et al. 2001; Wang et al. 2007a, 2008), despite the selection bias against obscured systems, appears to be in line with this expectation.

The SSFR analysis of the AzTEC–GOODS sources also suggests an intriguing idea that there may be two classes of SMGs, possibly driven by two different modes of star formation or observed at two different phases. While the M_* for these SMGs span over a factor of 30 (see Fig. 8), the SFR_{IR} and $SFR_{UV} + SFR_{IR}$ show no dependence on M_* in Fig. 9. This is in contrast to the finding by Davé, Oppenheimer & Finlator (2011), where a tight M_*–SFR relation is a generic outcome of all of their cosmological hydrodynamic simulations incorporating galactic outflows. One way to interpret our observational results summarized in Fig. 9 is that only SMGs with $M_* \gtrsim 10^{10.5}$ have properties similar to the objects modelled by Davé et al., following the M_*–SFR relation predicted for SMGs (solid line in Fig. 9; Davé et al. 2010). AzTEC–GOODS sources with $M_* < 10^{10.5}$ may follow a different, currently unknown process that leads to 10 times larger SSFR. This is somewhat analogous to the mass-dependent SSFR seen among galaxies in the local universe ('red' and 'blue sequence') with a similar range of M_*, although with one to two orders of magnitudes lower SSFRs. A division by mass certainly seems somewhat arbitrary. On the other hand, these SMGs appear to show a sign of grouping by mass in the middle and right-hand panel of Fig. 11. A hint of bimodality in the histogram of M_* is also seen in Fig. 8. Future Large Millimeter Telescope (LMT) and Atacama Large Millimeter Array (ALMA) surveys of much larger samples with higher angular resolution and spectroscopic redshifts should provide a definitive test on this intriguing possibility.

6 AGN AND STARBURST ACTIVITIES

Determining the source of enormous luminosity associated with SMGs is an outstanding problem that has important implications on understanding the mass assembly history of galaxies. To probe the nature of the heavily obscured power source, optically thin tracers in the X-ray, IR or radio wavelengths are necessary. Here, we examine the properties of AzTEC sources identified in the GOODS-South and GOODS-North fields using several well-established diagnostic tests utilizing these optically thin tracers.

6.1 *Spitzer* IRAC colour–colour diagram

The first set of diagnostic tests to examine are the IRAC colour–colour diagrams that are commonly used for identifying heavily obscured AGN based on the colour combinations proposed by Lacy et al. (2004) and Stern et al. (2005) as shown in Figs 12 and 13, respectively. The majority of robustly identified AzTEC sources in both GOODS fields fall within the regions previously identified with power-law AGN in both plots. As argued in detail below, these results are not a direct consequence of using a *Spitzer* IRAC colour selection for identifying AzTEC counterpart sources. Interpreting these results should also require some care as a young starburst population at $z > 1$ has a characteristic red SED in this part of the spectrum and should fall within the same colour region (see Yun et al. 2008).

The sample size of AzTEC–GOODS sources plotted in Figs 12 and 13 is nearly three times larger than the sample previously analysed by Yun et al., and these new plots show more clearly that these AzTEC sources cluster densely around the theoretical colour tracks of 20–80 Myr old dusty starbursts at $z \gtrsim 2$ by Efstathiou et al. (2000). The dispersion in the model tracks and the observed colour
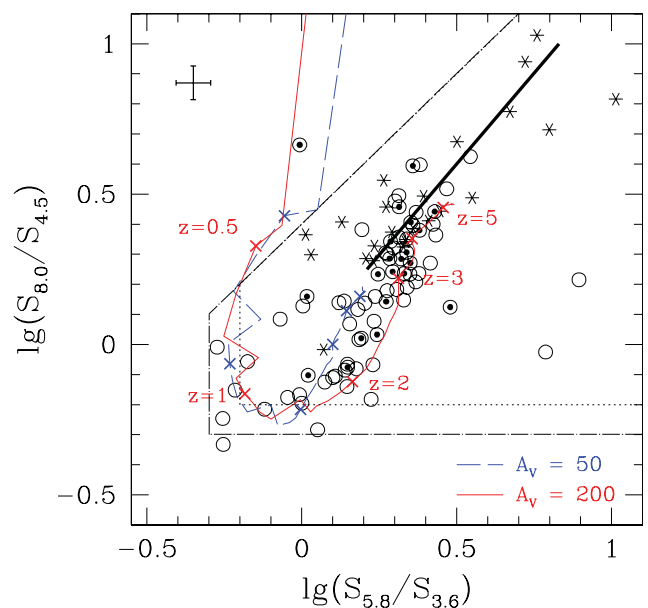
Figure 12. A $S_{8.0\,\mu m}/S_{4.5\,\mu m}$ versus $S_{5.8\,\mu m}/S_{3.6\,\mu m}$ IRAC colour diagnostic diagram for heavily obscured starbursts and AGNs based on the colour combinations proposed by Lacy et al. (2004). Areas occupied by dusty young starbursts as noted by Yun et al. (2008, see their fig. 1) are outlined by a dot–dashed line, while the area previously identified with power-law spectrum AGNs by Lacy et al. is outlined using a dotted line. The IRAC counterparts identified with the AzTEC sources in GOODS-South and GOODS-North with empty (undetected in X-ray) and dotted circles (detected in X-ray) cluster around the theoretical dusty starburst SED tracks with different amounts of dust extinction ($A_V = 50$ and 200; Efstathiou et al. 2000), as discussed by Yun et al. (2008). The thick solid line represents the theoretical track expected of purely power-law IR AGN, while asterisks are power-law AGN reported by Lacy et al. and Martinez-Sansigre et al. (2008). Typical uncertainties in the colours are shown by the cross in the upper left-hand corner.

are larger in Fig. 13, but the AzTEC sources again mostly occupy the region spanned by the starburst model tracks, rather than the area surrounding the IR power-law track. It is particularly noteworthy that AzTEC sources identified with a *Chandra* X-ray source (dotted circles) occupy largely the same area as those without X-ray detection (empty circles), and only a small fraction of sources (both with and without X-ray detection) overlap with the IR power-law AGN (asterisks; see Yun et al. 2008). Conversely, many of the AzTEC sources appearing among the power-law IR sources are undetected in the 2 and 4 Ms *Chandra* surveys (Alexander et al. 2003; Luo et al. 2008; Johnson et al. 2011). There is a weak trend of an increasing fraction of X-ray detected sources with redder colour. We can conclude from these diagnostic plots that nearly all of the AzTEC sources identified in the GOODS fields have IRAC SEDs consistent with that of a young starburst, while a small fraction ($\lesssim 20$ per cent) shows IR colours of a power-law AGN.

One thing to clarify is that the use of IRAC colours as a method to identify the AzTEC counterparts does not lead directly to these observed trends. The adopted colour selection, $[3.6\,\mu m] - [4.5\,\mu m] \geq 0.0$, imposes no restriction on the 5.8 and 8.0 μm photometry. This colour selection is also only one of *three* independent criteria we examine jointly, and the radio data contribute overwhelmingly to the secure counterpart identification. In fact, *none* of the robustly identified sources in Table 1 is based on the IRAC colour selection alone (see Section 2.1). This colour selection is not used to *reject* any counterpart candidates either, and indeed several robust counterparts shown in Fig. 13 have a
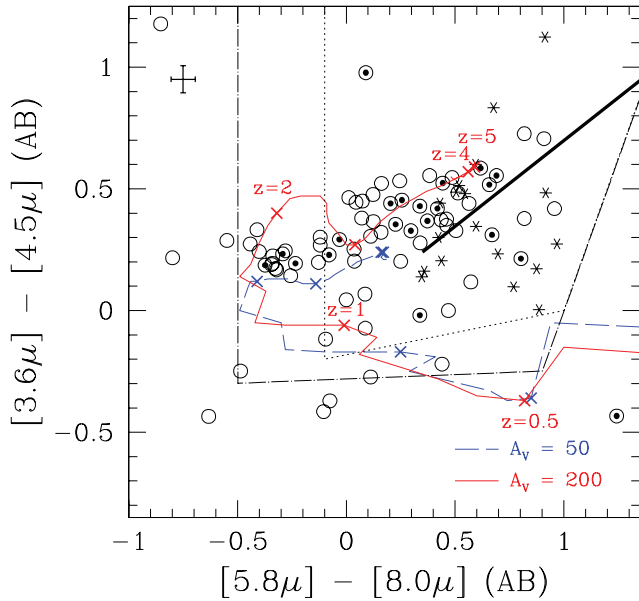
Figure 13. A $[3.6\,\mu m] - [4.5\,\mu m]$ versus $[5.8\,\mu m] - [8.0\,\mu m]$ IRAC colour diagnostic diagram for heavily obscured starbursts and AGN based on the colour combinations proposed by Stern et al. (2005), adopted from fig. 2 of Yun et al. (2008). All symbols and models shown are identical to those in Fig. 12.

blue IRAC colour ($[3.6\,\mu m] - [4.5\,\mu m] < 0.0$). In the context of the starburst SED model tracks shown, the colour selection of $[3.6\,\mu m] - [4.5\,\mu m] \geq 0.0$ effectively imposes a redshift bias against sources at $z \lesssim 1$ such as AzTEC/GS20. However, this bias is more than compensated by the radio and MIPS identification methods that systematically favour low-z candidate counterparts.

6.2 Optical–IRAC–MIPS colours

Another widely used AGN diagnostic diagram is the *Spitzer* mid-IR colour plot first introduced by Ivison et al. (2004). They noted that starburst and AGN colour tracks as a function of redshift are well separated in the plot of flux ratios $S_{24}/S_{8.0}$ versus $S_{8.0}/S_{4.5}$ due to contributions by a power-law AGN and polycyclic aromatic hydrocarbon (PAH) emission in the 24 μm band. By analysing *Spitzer* Infrared Spectrograph (IRS) data on 24 μm selected galaxies, Pope et al. (2008b) found that the main discriminatory information resides in the $S_{8.0}/S_{4.5}$ flux ratio, or the spectral slope in the rest-frame NIR band. This colour selection is similar to the earlier IRAC colour analysis proposed by Lacy et al. (2004) and Stern et al. (2005), and it is again subject to the same confusion with young starburst systems as noted by Yun et al. (2008) and others. The new AGN diagnostic condition of $S_{8.0}/S_{4.5} \geq 2$ proposed by Pope et al. (2008b) corresponds to $\lg(S_{8.0}/S_{4.5}) \geq +0.3$ in Fig. 12, and objects satisfying this criteria should also include dusty young starbursts at $z \leq 0.5$ and $z > 3$ as well as power-law IR AGN.

Our version of the Pope et al. (2008b) diagnostic test is shown in Fig. 14, which shows the plot of the MIPS 24 μm to optical *i*-band flux ratio versus $S_{8.0\,\mu m}/S_{4.5\,\mu m}$ IRAC band flux ratio for AzTEC sources in both GOODS fields. Among the 57 sources plotted, only 16 (28 per cent) have the $S_{8.0}/S_{4.5}$ flux ratio consistent with hosting an energetic AGN (right of the long dashed line). Again, X-ray detection (dotted circles) appears to have little bearing on whether an object falls on the starburst ('SB') side or the 'AGN' side. The source with the highest ratio $S_{8.0\,\mu m}/S_{4.5\,\mu m} = 4.6$ is AzTEC/GS20,
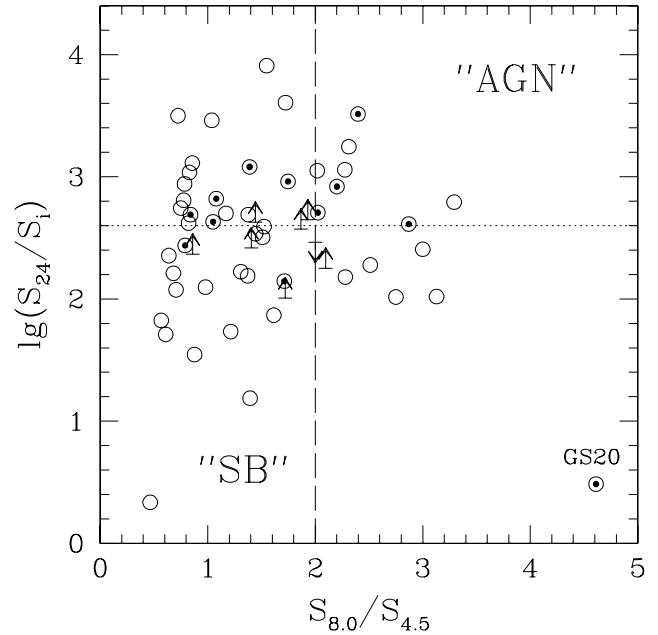
Figure 14. A diagnostic colour–colour diagram using MIPS 24 μm to optical *i*-band flux ratio versus $S_{8.0\,\mu m}/S_{4.5\,\mu m}$ IRAC band flux ratio. Symbols are identical to those in Fig. 12. The long dashed line at $S_{8.0}/S_{4.5} = 2$ is the dividing line for AGNs and starbursts as proposed by Pope et al. (2008b). The dotted line near $\lg(S_{24}/S_i) = 2.6$ is the equivalent division line for the $z \sim 2$ 'DOGs' with $F_\nu(24\,\mu m)/F_\nu(R) \gtrsim 1000$ – see Dey et al. (2008) and Fiore et al. (2008).

which is a $z = 0.0369$ galaxy whose $S_{8.0\,\mu m}/S_{4.5\,\mu m}$ ratio arises from the bright PAH line emission in the 8 μm band, rather than due to a power-law AGN – also see Fig. 12.

The choice of the flux ratio between the MIPS 24 μm and the optical *i* band for the vertical axis in Fig. 14 is motivated by the claim of a new class of faint MIPS 24 μm sources that were missed by earlier optical studies. These so-called 'dust-obscured galaxies' ('DOGs'; Dey et al. 2008; Fiore et al. 2008) represent a population of infrared bright galaxies that are extremely faint in the optical bands, characterized by $F_\nu(24\,\mu m)/F_\nu(R) \gtrsim 1000$. These $z \sim 2$ galaxies have similar projected density as SMGs and may account for as much as ~1/4 of the IR luminosity density at this redshift (Dey et al. 2008; Pope et al. 2008b). Evidence for both star formation and AGN activity has been reported for these objects. Based on their stacking analysis of the X-ray hardness ratio, Fiore et al. (2008) proposed that as many as 80 per cent of these DOGs host a Compton-thick AGN.

Adopting a mean colour of $r - i \approx +1.0$ for the radio-selected SMGs (e.g. Ivison et al. 2002), the '$F_\nu(24\,\mu m)/F_\nu(R) \gtrsim 1000$' definition for DOGs translates to '$\lg(S_{24\,\mu m}/S_i) \gtrsim 2.6$' in Fig. 14. Among the 12 X-ray detected secure AzTEC counterpart sources with sufficient optical and *Spitzer* data to be included in this analysis, nearly equal numbers of SMGs fall on either side of this division line. One significant difference is that nine X-ray detected AzTEC sources fall on the optically faint side (above the dotted line), while only three X-ray detected AzTEC sources (including the low-z source AzTEC/GS20) are found on the optically bright side. This trend is consistent with the suggestion by Fiore et al. that many of these DOGs host a Compton-thick AGN. However, there are just as many AzTEC sources undetected in the X-ray above the division line. Given that the observed X-ray emission can be largely accounted for by the starburst activity in many cases (see below

and Alexander et al. 2005), the significance of a higher frequency of X-ray detection among these optically faint SMGs is not entirely clear.

6.3 X-ray

The 2 and 4 Ms *Chandra* X-ray surveys of the two GOODS fields (Alexander et al. 2003; Luo et al. 2008; Johnson et al. 2011; Xue et al. 2011) are some of the deepest X-ray data available and thus offers the best opportunity to determine X-ray properties of all types of extragalactic sources. A cross-correlation of the AzTEC and *Chandra* X-ray catalogue has shown that 16 (out of 48) and eight (out of 40) AzTEC sources in the GOODS-South and GOODS-North fields have an X-ray source within 6 arcsec of the AzTEC centroid positions (Johnson et al. 2011). Given the low density of X-ray sources, these coincidences are highly statistically significant. On the other hand, only a subset of these X-ray sources are robust counterparts, and another physical link such as the clustering of massive galaxies (e.g. Almaini et al. 2003) must play a role.

The derived 2–10 keV X-ray luminosity of these *Chandra* sources favour the AGN origin for the observed X-ray emission. Examining the X-ray properties of faint radio sources in the *Hubble Deep Field*-North, Bauer et al. (2002) found that the linear correlation between X-ray luminosity and 1.4 GHz radio luminosity density of late-type galaxies extends to luminous X-ray detected emission-line galaxies at intermediate redshift, suggesting both the X-ray and radio processes are associated with star formation activities. Persic et al. (2004) have shown that the integrated emission from high-mass X-ray binaries (HMXBs) can offer a natural explanation for the observed correlation, and given their short lifetime the measured X-ray luminosity can offer an *instantaneous snapshot* of the ongoing SFR. Since HMXBs also display a characteristic hard X-ray spectrum, the hardness ratio of the observed X-ray emission does not provide a unique probe of AGN activity (e.g. Fiore et al. 2008, see Section 6.2). On the other hand, X-ray luminosity of these *Chandra* sources associated with AzTEC detection ranges between $L_X(2.0–10\,\mathrm{keV}) = 10^{42}$ and $10^{43}\,\mathrm{erg\,s^{-1}}$. When converted to a SFR using the relation given by Persic et al. (2004), their inferred SFR ranges between 10^3 and $10^4\,\mathrm{M_\odot\,yr^{-1}}$, exceeding the SFR derived from their UV and IR properties (see Fig. 9). A fainter X-ray source with 2–10 keV luminosity of $10^{42}\,\mathrm{erg\,s^{-1}}$ can be either a low-luminosity AGN or an SMG with a SFR $= 10^3\,\mathrm{M_\odot\,yr^{-1}}$, but any source with a higher X-ray luminosity would require a significant AGN contribution (see Johnson et al. 2011).

One intriguing trend found is that the fraction of robust AzTEC counterparts that are also *Chandra*-detected X-ray sources is higher for the brighter AzTEC sources. The 30 per cent (seven and eight out of 25) of the brightest AzTEC sources in the GOODS-South and GOODS-North fields are detected individually as a *Chandra* X-ray source, and an increasing AGN activity may be associated with the most luminous AzTEC sources. In the same vein, the number of candidate *Chandra* counterpart in the GOODS-South field did *not* change from the 2 to 4 Ms catalogue, and the greater depth of the X-ray data had curiously little impact. The higher frequency of X-ray counterpart in the GOODS-South field (16/48 versus 8/40) may reflect the cosmic variance in these two relatively small size fields. A more detailed discussion of the X-ray properties of AzTEC sources is presented elsewhere (Johnson et al. 2011).

The high detection rate for the AzTEC sources in the X-ray bodes well for coeval mass growth scenarios for the stellar component and the central supermassive black hole (SMBH) designed to explain the apparent correlation between the central black hole mass and stellar velocity dispersion ('M–σ relation'; Magorrian et al. 1998; Ferrarese & Merritt 2000; Gebhardt et al. 2000). For example, through detailed numerical modelling, Narayanan et al. (2010a,b) have shown that a rapid build-up of stellar mass and the growth of the central SMBH can be achieved through a merger-driven starburst, and can reproduce the observed properties of SMGs and dust-obscured QSOs. Winds driven by the starburst and the AGN activity can effectively disrupt the central concentration of gas and dust, driving the evolution of such objects from an SMG phase to a QSO phase (Narayanan et al. 2008).

A natural consequence of such a scenario is that a massive stellar galaxy with a maturing young stellar population would emerge unobscured as the central AGN begins to dominate the overall energetics. As the feedback process starts to clear out the obscuring dust and gas, the central AGN would also become more detectable in the X-ray, UV and optical bands, marking the beginning of the classical QSO phase. However, the X-ray detected AzTEC sources in the optical and NIR bands span the entire observed range of brightness, indistinguishable from the X-ray undetected sources in Fig. 6. The $i - K$ colours of the X-ray detected sources are also indistinguishable from the others, suggesting that either (1) the X-ray detection does *not* signal the emergence of the central AGN as the dominant energy source or (2) additional complexity is required in the SMG–QSO evolution model.

By analysing the properties of a sample of $z \approx 2$ SMGs exhibiting broad Hα and Hβ emission lines, Alexander et al. (2008) have estimated their black hole mass to be $\gtrsim 3$ times smaller than those found in comparable mass normal galaxies in the local universe, and $\gtrsim 10$ times smaller than those predicted for $z \approx 2$ luminous quasars and radio galaxies. Based on this evidence, they argued that the growth of the black hole lags that of the host galaxy in SMGs. We find only marginal evidence for AGN contribution to the NIR (Figs 12 and 13) and mid-IR (Fig. 14) SEDs for the robust AzTEC sources, even among those detected in the X-ray. The spectral decomposition and the analysis of the emission, absorption and continuum features in the *Spitzer* IRS spectra of SMGs by Pope et al. (2008a), Menéndez-Delmestre et al. (2009) and Murphy et al. (2009) have found that a starburst dominates the luminosity in the large majority of cases, even when the sample is selected to have AGN-like colours (Coppin et al. 2010b). A consistent trend emerging from these multiwavelength data analyses is that dust-obscured starburst activity can account for most of the luminosity in SMGs, with little or only a minor contribution from AGN.

7 SUMMARY AND DISCUSSION

Taking advantage of some of the deepest imaging and photometry data and extensive spectroscopic information in the GOODS-South field, we searched for counterparts to the 48 AzTEC sources found in the deep 1.1 mm wavelength survey by Paper I, using a P statistic analysis involving VLA 1.4 GHz, *Spitzer*/MIPS 24 μmm and IRAC catalogues, combined with cross-identification with LABOCA 870 μm sources. Robust ($P \leq 0.05$) and tentative ($0.05 < P \leq 0.20$) counterpart candidates are found for 27 and 14 AzTEC GOODS-South sources, respectively. Five of the sources (10 per cent) have two robust counterparts, supporting the idea that these SMGs are strongly clustered and/or confused. A spectroscopic redshift is available for 12 robust counterparts and 12 tentative counterparts, while photometric redshifts based on rest-frame UV-to-optical and radio-millimetric SED analysis are available for the remainder. Stellar mass (M_*) and SFR_{UV} are derived by modelling the observed optical and *Spitzer* IRAC photometry, while SFR_{IR}

is derived by analysing the IR, (sub)millimetre and radio photometry using theoretical templates. To improve the statistics of the subsequent analysis, we applied the same counterpart identification and SED analysis to the AzTEC 1.1 mm sources identified in the GOODS-North field (Perera et al. 2008; Downes et al. 2011).

Estimates of the redshift distribution of AzTEC-GOODS sources are constructed by combining spectroscopic redshifts with UV+optical and radio–millimetric photometric redshifts, and these two redshift distributions agree well with each other as shown in Fig. 4. Our analysis shows that 80 per cent of AzTEC sources are at $z \geq 2$, with a median redshift of $z_{med} \sim 2.6$, and there is a significant high-redshift tail with 20 per cent of AzTEC sources at $z \geq 3.3$. These distributions are quite different from the commonly cited SMG redshift distribution of Chapman et al. (2005), primarily at the low-redshift end. The SHADES survey redshift distribution by Aretxaga et al. (2007) is in better agreement with our redshift distribution derived from the AzTEC–GOODS surveys, and like ours, is missing the low-redshift tail seen in Chapman et al. (2005). Complete CO spectroscopic redshift surveys using the LMT and ALMA will be able to accurately determine the SMG redshift distribution by overcoming the large number of systematic biases inherent in all of these analyses.

An examination of the rest-frame UV and optical photometry for the securely identified AzTEC sources shows a nearly 10 mag (a factor of 10^4 in flux density) spread in the i- and K-band photometry and extremely red colours spanning $i - K$ colour between 0 and +6. There are a small minority of SMGs that are bright in the rest-frame UV bands, overlapping with star-forming galaxy population previously identified in the rest-frame UV searches. On the other hand, AzTEC–GOODS sources are on average quite red and faint, with a median brightness of $i = 25.3$ and $K = 22.6$, and a large fraction of AzTEC sources are entirely missed by previous surveys of star-forming galaxies. Examining the observed scatter in the $i - K$ colour, we deduce that there is at least a factor of 10 variation in the intrinsic rest-frame optical luminosity among these SMGs.

A Hubble diagram of the observed IRAC 3.6 μm flux density shows that these AzTEC–GOODS sources are some of the most luminous galaxies in the rest-frame optical bands at $z \geq 2$, offering a good explanation as to why nearly every SMG identified with interferometric observations shows a relatively bright IRAC counterpart. Modelling of the observed rest-frame UV and optical SEDs shows that the stellar masses are rather large, $M_* = (1–30) \times 10^{10} \, M_\odot$, with a surprisingly large $SFR_{UV} \gtrsim 100–1000 \, M_\odot \, yr^{-1}$ for about 50 per cent of these galaxies. In comparison, SFR_{IR} derived from modelling the IR to radio SED covers a relatively tight range of 200–2000 $M_\odot \, yr^{-1}$, independent of the redshift or stellar mass. Whether a galaxy has been detected in the X-ray by *Chandra* appears to have no influence on the derived M_*, SFR_{UV}, SFR_{IR} and SFR_{UV}/SFR_{IR} ratio, and the presence of an X-ray bright AGN appears to have relatively little influence on these quantities.

These AzTEC–GOODS sources have a SSFR 10–100 times higher ($SSFR \approx 1–100 \, Gyr^{-1}$) than similar stellar mass galaxies at $z = 0$, and they extend the previously observed rapid rise of SSFR with redshift ($SSFR \propto (1 + z)^5$; Damen et al. 2009) to $z = 2–5$. More importantly, *all* of the AzTEC-GOODS sources have a SSFR above the inverse Hubble time line, indicating that they have a current SFR high enough to have built up their entire stellar mass within the Hubble time at their observed redshift. This might be the best quantitative evidence yet that we are witnessing these galaxies during their rapid mass build-up phase. The flat SSFR as a function of redshift we deduce contradicts the model prediction of a tight M_*–SFR relation based on cosmological hydrodynamic sim-

ulations incorporating galactic outflows (Davé et al. 2010, 2011). However, AzTEC sources with $M_* \gtrsim 10^{10.5} \, M_\odot$ appear to follow this model prediction, and one plausible explanation is that a different mechanism is operating for the lower mass SMGs, leading to a 10 times higher SSFR. Alternatively, they are seen at a different phase of rapid mass build-up. Much of the CIRB is expected to be associated with fainter sources below the confusion limit of our AzTEC surveys, and their number counts can offer an important constrain to the evolution model for SMGs (Granato et al. 2004; Baugh et al. 2005; Rowan-Robinson 2009). It still remains to be shown whether these are young, lower mass galaxies seen in their rapid formation epoch or the simmering activities in more massive galaxies that have already undergone an SMG-like rapid build-up phase in even earlier epochs.

Lastly, we examine the evidence for luminous AGN in these systems using three different diagnostic tests: (1) the *Spitzer* IRAC colour–colour diagram, (2) optical–IRAC–MIPS colours and (3) X-ray luminosity. We find only marginal evidence for AGN contribution to the NIR (Figs 12 and 13) and mid-IR (Fig. 14) SEDs for the robust AzTEC sources, even among those detected in the X-ray. A consistent trend emerging from this multiwavelength data analysis and similar studies by other groups is that dust-obscured starburst activity can account for most of the luminosity in submm/mm-selected galaxies, with little or only a minor contribution from AGN.

NOTE ADDED IN PRESS

During the production of this article after the manuscript was accepted, I. Smail has alerted the authors that a paper by Wardlow et al. (2011) reporting a similar analysis of 74 LABOCA 870 μm sources in the Extended *Chandra Deep Field* has appeared in the journal. The redshift distribution and estimated stellar masses are similar to those reported here, including a population at a high-redshift tail (15 per cent of sources at $z > 3$).

REFERENCES

Akiyama M., 2005, ApJ, 629, 72
Alexander D. M. et al., 2003, AJ, 126, 539
Alexander D. M., Bauer F. E., Chapman S. C., Smail I., Blain A. W., Brandt W. N., Ivison R. J., 2005, ApJ, 632, 736
Alexander D. M. et al., 2008, AJ, 135, 1968
Almaini O. et al., 2003, MNRAS, 338, 303
Almeida C., Baugh C. M., Lacey C. G., 2011, MNRAS, 417, 2057
Aretxaga I., Hughes D. H., Chapin E. L., Gaztanaga E., Dunlop J. S., Ivison R. J., 2003, MNRAS, 342, 759
Aretxaga I. et al., 2007, MNRAS, 379, 1571
Austermann J. E. et al., 2010, MNRAS, 401, 160
Balestra I. et al., 2010, A&A, 512, A12

Barger A. J., Cowie L. L., Sanders D. B., Fulton E., Taniguchi Y., Sato Y., Kawara K., Okuda H., 1998, Nat, 394, 248

Barger A. J., Cowie L. L., Smail I., Ivison R. J., Kneib J.-P., 1999, AJ, 117, 2656

Barger A. J., Cowie L. L., Richards E. A., 2000, AJ, 119, 2092

Bauer F. E., Alexander D. M., Brandt W. N., Hornschemeier A. E., Vignali C., Garmire G. P., Schneider D. P., 2002, AJ, 124, 2351

Bauer A. E., Drory N., Hill G. J., Feulner G., 2005, ApJ, 621, L89

Baugh C. M., Lacey C. G., Frenk C. S., Granato G. L., Silva L., Bressan A., Benson A. J., Cole S., 2005, MNRAS, 356, 1191

Bell E. F. et al., 2004, ApJ, 608, 752

Bell E. F., Zheng X. Z., Papovich C., Borch A., Wolf C., Meisenheimer K., 2007, ApJ, 663, 834

Bertoldi F. et al., 2000, A&A, 360, 92

Bertoldi F. et al., 2007, ApJS, 172, 132

Biggs A. D. et al., 2011, MNRAS, 413, 2314

Blain A. W., Smail I., Ivison R. J., Kneib J.-P., Frayer D. T., 2002, Phys. Rep., 369, 111

Blain A. W., Chapman S. C., Smail I., Ivison R., 2004, ApJ, 611, 725

Borys C., Chapman S., Halpern M., Scott D., 2003, MNRAS, 344, 385

Borys C., Scott D., Chapman S., Halpern M., Nandra K., Pope A., 2004, MNRAS, 355, 485

Calzetti D., Armus L., Bohlin R. C., Kinney A. L., Koornneef J., Storchi-Bergmann T., 2000, ApJ, 533, 682

Capak P. et al., 2008, ApJ, 681, L53

Carilli C. L., Yun M. S., 1999, ApJ, 513, L13

Carilli C. L., Yun M. S., 2000, ApJ, 530, 618

Carilli C. L. et al., 2001, ApJ, 555, 625

Casey C. M., Chapman S. C., Smail I., Alaghband-Zadeh S., Bothwell M. S., Swinbank A. M., 2011, MNRAS, 411, 2739

Chapin E. L. et al., 2009, MNRAS, 398, 1793

Chapin E. L. et al., 2011, MNRAS, 411, 505

Chapman S. C., Richards E. A., Lewis G. F., Wilson G., Barger A. J., 2001, ApJ, 548, L147

Chapman S. C., Blain A. W., Smail I., Ivison R. J., 2005, ApJ, 622, 772

Chen Y., Lowenthal J. D., Yun M. S., 2010, ApJ, 713, 1385

Clements D. L. et al., 2008, MNRAS, 387, 247

Clements D. L., Dunne L., Eales S., 2010, MNRAS, 403, 274

Condon J. J., 1992, ARA&A, 30, 575

Cooray A. et al., 2010, A&A, 518, L22

Coppin K. et al., 2006, MNRAS, 372, 1621

Coppin K. et al., 2009, MNRAS, 395, 1905

Coppin K. et al., 2010a, MNRAS, 407, L103

Coppin K. et al., 2010b, ApJ, 713, 503

Cowie L. L., Sangaila A., Hu E. M., Cohen J. G., 1996, AJ, 112, 839

Cowie L. L., Barger A. J., Kneib J.-P., 2002, AJ, 123, 2197

Daddi E., Cimatti A., Renzini A., Fontana A., Mignoli M., Pozzetti L., Tozzi P., Zamorani G., 2004, ApJ, 617, 746

Daddi E. et al., 2007, ApJ, 670, 156

Daddi E. et al., 2009, ApJ, 694, 1517

Damen M., Labbe I., Franx M., van Dokkum P. G., Taylor E. N., Gawiser E. J., 2009, ApJ, 690, 937

Dannerbauer H., Lehnert M. D., Lutz D., Tacconi L., Bertoldi F., Carilli C., Genzel R., Menten K., 2002, ApJ, 573, 473

Dannerbauer H., Walter F., Morrison G., 2008, ApJ, 673, L127

Davé R., Finlator K., Oppenheimer B. D., Fardal M., Katz N., Keres D., Weinberg D. H., 2010, MNRAS, 404, 1355

Davé R., Oppenheimer B., Finlator K., 2011, MNRAS, 415, 11

Devlin M. J. et al., 2009, Nat, 458, 737

Dey A. et al., 2008, ApJ, 677, 943

Diaz-Sanchez A., Villo-Perez I., Perez-Garrido A., Rebolo R., 2007, MNRAS, 377, 516

Downes A. J. B., Peacock J. A., Savage A., Carrie D. R., 1986, MNRAS, 218, 31

Downes T. P., Welch D., Scott K., Austermann J., Wilson G. W., 2011, MNRAS, submitted

Dunlop J. S. et al., 2010, MNRAS, 408, 2022

Dunne L. et al., 2009, MNRAS, 394, 3

Dye S. et al., 2008, MNRAS, 386, 1107

Eales S., Lilly S., Gear W., Dunne L., Bond J. R., Hammer F., Le Fèvre O., Crampton D., 1999, ApJ, 515, 518

Eales S., Lilly S., Webb T., Dunne L., Gear W., Clements D., Yun M., 2000, AJ, 120, 2244

Eales S., Bertoldi F., Ivison R., Carilli C., Dunne L., Owen F., 2003, MNRAS, 344, 169

Efstathiou A., Rowan-Robinson M., 2003, MNRAS, 343, 322

Efstathiou A., Rowan-Robinson M., Siebenmorgen R., 2000, MNRAS, 313, 734

Elbaz D. et al., 2007, A&A, 468, 33

Erb D. K., Steidel C. C., Shapley A. E., Pettini M., Reddy N. A., Adelberger K. L., 2006, ApJ, 647, 128

Erickson N., Narayanan G., Goeller R., Grosslein R., 2007, in Baker A. J., Glenn J., Harris A. I., Mangum J. G., Yun M. S., eds, ASP Conf. Ser. Vol. 375, From Z-Machines to ALMA: (Sub)Millimeter Spectroscopy of Galaxies. Astron. Soc. Pac., San Francisco, p. 71

Faber S. M. et al., 2007, ApJ, 665, 265

Feigelson E. D., Nelson P. I., 1985, ApJ, 293, 192

Ferrarese L., Merritt D., 2000, ApJ, 539, L9

Feulner G., Gabasch A., Salvato M., Drory N., Hopp U., Bender R., 2005, ApJ, 633, L9

Fioc M., Rocca-Volmerange B., 1997, A&A, 326, 950

Fiore F. et al., 2008, ApJ, 672, 94

Fixsen D. J., Dwek E., Mather J. C., Bennett C. L., Shafer R. A., 1998, ApJ, 508, 123

Fox M. J. et al., 2002, MNRAS, 331, 839

Frayer D. T., Smail I., Ivison R. J., Scoville N. Z., 2000, AJ, 120, 1668

Gawiser E. et al., 2006, ApJS, 162, 1

Gebhardt K. et al., 2000, ApJ, 539, L9

Giavalisco M. et al., 2004, ApJ, 600, L93

Goldader J. D., Meurer G., Heckman T. M., Siebert M., Sanders D. B., Calzetti D., Steidel C. C., 2002, ApJ, 568, 651

Granato G. L., De Zotti G., Silva L., Bressan A., Danese L., 2004, ApJ, 600, 580

Greve T. R., Ivison R. J., Bertoldi F., Stevens J. A., Dunlop J. S., Lutz D., Carilli C. L., 2004, MNRAS, 354, 779

Greve T. R., Pope A., Scott D., Ivison R. J., Borys C., Conselice C. J., Bertoldi F., 2008, MNRAS, 389, 1489

Hainline L. J., Blain A. W., Smail I., Frayer D. T., Chapman S. C., Ivison R. J., Alexander D. M., 2009, ApJ, 699, 1610

Hatsukade B. et al., 2010, ApJ, 711, 974

Hayward C. C., Keres D., Jonsson P., Narayanan D., Cox T. J., Hernquist L., 2011, ApJ, submitted

Holland W. S. et al., 1999, MNRAS, 303, 659

Houck J. R. et al., 2004, ApJS, 154, 18

Huang J.-S. et al., 2009, ApJ, 700, 183

Hughes D. H. et al., 1998, Nat, 394, 241

Hughes D. H. et al., 2002, MNRAS, 335, 871

Ikarashi S. et al., 2011, MNRAS, 415, 3081

Iono D. et al., 2006, ApJ, 640, L1

Ivison R. J., Smail I., Barger A. J., Kneib J.-P., Blain A. W., Owen F. N., Kerr T. H., Cowie L. L., 2000, MNRAS, 315, 209

Ivison R. J. et al., 2002, MNRAS, 337, 1

Ivison R. J. et al., 2004, ApJS, 154, 124

Ivison R. J. et al., 2007, MNRAS, 380, 199

Ivison R. et al., 2010, A&A, 518, L31

Johnson S. P., Wilson G. W., Wang Q. D., Williams C. C., Scott K., Yun M. S., Lowenthal J., 2011, MNRAS, submitted

Kauffmann G. et al., 2003, MNRAS, 341, 33

Kaviani A., Haehnelt M. G., Kauffmann G., 2003, MNRAS, 340, 739

Kellermann K. I., Fomalont E. B., Mainieri V., Padovani P., Rosati P., Shaver P., Tozzi P., Miller N., 2008, ApJS, 179, 71

Kennicutt R. C., Jr, 1998, ARA&A, 36, 189

Keres D., Katz N., Weinberg D. H., Davé R., 2005, MNRAS, 363, 2

Kriek M. et al., 2008, ApJ, 677, 219

Lacki B., Thompson T., 2010, ApJ, 717, 196

Lacy M. et al., 2004, ApJS, 154, 166

Laidler V. G. et al., 2007, PASP, 119, 1325
Laurent G. T. et al., 2005, ApJ, 623, 742
Le Fevre O. et al., 2004, A&A, 428, 1043
Le Floc'h E. et al., 2005, ApJ, 632, 169
Lilly S. J., Eales S. A., Gear W. K. P., Hammer F., Le Fevre O., Crampton D., Bond J. R., Dunne L., 1999, ApJ, 518, 641
Luo B. et al., 2008, ApJS, 179, 19
Lutz D. et al., 2001, A&A, 378, 70
Lutz D., Valiante E., Sturm E., Genzel R., Tacconi L. J., Lehnert M. D., Sternberg A., Baker A. J., 2005, ApJ, 625, L83
Madau P., 1995, ApJ, 441, 18
Magnelli B., Elbaz D., Chary R. R., Dickinson M., Le Borgne D., Frayer D. T., Wilmer C. N. A., 2009, A&A, 496, 57
Magnelli B., Elbaz D., Chary R. R., Dickinson M., Le Borgne D., Frayer D. T., Wilmer C. N. A., 2011, A&A, 528, A35
Magorrian J. et al., 1998, AJ, 115, 2285
Maraston C., Pforr J., Renzini A., Daddi E., Dickinson M., Cimatti A., Tonini C., 2010, MNRAS, 407, 830
Martinez-Sansigre A., Lacy M., Sajina A., Rawlings S., 2008, ApJ, 674, 676
Menéndez-Delmestre K. et al., 2007, ApJ, 655, L65
Menéndez-Delmestre K. et al., 2009, ApJ, 699, 667
Michalowski M., Hjorth J., Watson D., 2010, A&A, 514, A67
Mignoli M. et al., 2005, A&A, 437, 883
Miller N. A., Fomalont E. B., Kellermann K. I., Mainieri V., Norman C., Padovani P., Rosati P., Tozzi P., 2008, ApJS, 179, 114
Murphy E. J., Chary R.-R., Alexander D. M., Dickinson M., Magnelli B., Morrison G., Pope A., Teplitz H. I., 2009, ApJ, 698, 1380
Narayanan D. et al., 2008, ApJS, 176, 331
Narayanan D., Hayward C. C., Cox T. J., Hernquist L., Jonsson P., Younger J. D., Groves B., 2010a, MNRAS, 401, 1613
Narayanan D. et al., 2010b, MNRAS, 407, 1701
Norris R. P. et al., 2006, AJ, 132, 2409
Pannella M. et al., 2009, ApJ, 698, L116
Pei Y. C., Fall S. M., Hauser M. G., 1999, ApJ, 522, 604
Perera T. A. et al., 2008, MNRAS, 391, 1227
Persic M., Rephaeli Y., Braito V., Cappi M., Della Ceca R., Franceschini A., Gruber D. E., 2004, A&A, 419, 849
Pope A., Chary R.-R., 2010, ApJ, 715, L171
Pope A. et al., 2006, MNRAS, 370, 1185
Pope A. et al., 2008a, ApJ, 675, 1171
Pope A. et al., 2008b, ApJ, 689, 127
Popesso P. et al., 2009, A&A, 494, 443
Retzlaff J., Rosati P., Dickinson M., Vandame B., Rite C., Nonino M., Cesarsky C. (GOODS Team), 2010, A&A, 511, 50
Rieke G. et al., 2004, ApJS, 154, 25
Rigopoulou D. et al., 2009, MNRAS, 400, 1199
Rowan-Robinson M., 2009, MNRAS, 394, 117
Rowan-Robinson M., 2010, MNRAS, 409, 2
Salimbeni S., Fontana A., Giallongo E., Grazian A., Menci N., Pentericci L., Santini P., 2009, in Giobbi G., Tornambe A., Raimondo G., Linongi M., Antonelli L. A., Menci N., Brocato E., eds, AIP Conf. Proc. Vol. 1111, Probing Stellar Populations Out to the Distant Universe. Am. Inst. Phys., New York, p. 207
Sanders D. B., Mirabel I. F., 1996, ARA&A, 34, 749
Scott S. E. et al., 2002, MNRAS, 331, 817
Scott K. S. et al., 2008, MNRAS, 385, 2225
Scott K. S. et al., 2010, MNRAS, 405, 2260 (Paper I)
Serjeant S. et al., 2003, MNRAS, 344, 887
Silverman J. D. et al., 2010, ApJS, 191, 124
Smail I., Ivison R. J., Blain A. W., 1997, ApJ, 490, L5
Smail I., Ivison R. J., Blain A. W., Kneib J.-P., 2002, MNRAS, 331, 495
Smail I., Chapman S. C., Blain A. W., Ivison R. J., 2004, ApJ, 616, 71
Smolcic V. et al., 2008, ApJS, 177, 14
Stern D. et al., 2005, ApJ, 631, 166
Strazzullo V., Pannella M., Owen F. N., Bender R., Morrison G. E., Wang W.-H., Shupe D. L., 2010, ApJ, 714, 1305
Swinbank K. et al., 2010, MNRAS, 405, 234

Szokoly G. P. et al., 2004, ApJS, 155, 271
Tacconi L. J. et al., 2008, ApJ, 680, 246
Tamura Y. et al., 2010, ApJ, 724, 1270
Treister E. et al., 2009, ApJ, 693, 1713
Tremonti C. A. et al., 2004, ApJ, 613, 898
Valiante E., Lutz D., Sturm E., Genzel R., Tacconi L. J., Lehnert M., Baker A. J., 2007, ApJ, 660, 1060
van Dokkum P. G. et al., 2008, ApJ, 677, L5
Vanzella E. et al., 2005, A&A, 434, 53
Vanzella E. et al., 2006, A&A, 454, 423
Vanzella E. et al., 2008, A&A, 478, 83
Vieira J. D. et al., 2010, ApJ, 719, 763
Wang W.-H., Cowie L. L., Barger A. J., 2004, ApJ, 613, 655
Wang R. et al., 2007a, AJ, 134, 617
Wang W.-H., Cowie L. L., van Saders J., Barger A. J., Williams J. P., 2007b, ApJ, 670, L89
Wang R. et al., 2008, ApJ, 687, 848
Wang W.-H., Cowie L. L., Barger A. J., Williams J. P., 2011, ApJ, 726, L18
Wardlow J. L. et al., 2011, MNRAS, 415, 1479
Webb T. M. et al., 2003a, ApJ, 587, 41
Webb T. M. A., Lilly S. J., Clements D. L., Eales S., Yun M., Brodwin M., Dunne L., Gear W. K., 2003b, ApJ, 597, 680
Weiss A. et al., 2009, ApJ, 707, 1201
Williams C. C. et al., 2011, ApJ, 733, 92
Wuyts S., van Dokkum P. G., Franx M., Forster S., Natascha M., Illingworth G. D., Labbe I., Rudnick G., 2009, ApJ, 706, 885
Xue Y. Q. et al., 2011, ApJS, 195, 10
Younger J. D. et al., 2007, ApJ, 671, 1531
Younger J. D. et al., 2008, MNRAS, 387, 707
Younger J. D. et al., 2009, ApJ, 704, 803
Yun M. S., Carilli C. L., 2002, ApJ, 568, 88
Yun M. S., Carilli C. L., Kawabe R., Tutui Y., Kohno K., Ohta K., 2002, ApJ, 528, 171
Yun M. S. et al., 2008, MNRAS, 389, 333
Zheng X. Z., Bell E. F., Papovich C., Wolf C., Meisenheimer K., Rix H.-W., Rieke G. H., Somerville R., 2007, ApJ, 661, L41

APPENDIX A: NOTES ON INDIVIDUAL SOURCES

AzTEC/GS1. There is one clear, robust counterpart (GS1a in Table 2), which is a radio source found 4.8 arcsec north of AzTEC/GS1 ($P_{1.4} = 0.045$). This faint radio source has an IRAC/MIPS counterpart ($P_{24\,\mu m} = 0.161$), which is also a *Chandra*/X-ray source. This source has a red IRAC colour with $[3.6\,\mu m] - [4.5\,\mu m] = +0.37$ ($P_{colour} = 0.133$), similar to the AzTEC sources identified using submillimetre interferometry (Younger et al. 2007; Yun et al. 2008). The 870 μm LABOCA source LESS J033211.3−275210 ($S_{870\,\mu m} = 9.2 \pm 1.2$ mJy) position is only 2.1 arcsec away from GS1a, and Biggs et al. (2011) also identify GS1a as the robust counterpart. No spectroscopic redshift is available for this extremely faint optical source ($i > 23.5$, $K > 22.9$), and it is likely a high-redshift ($z \geq 3$) source with $z_{opt} = 2.96 \pm 0.45$ and $z_{MR} = 3.56^{+0.66}_{-1.20}$.

AzTEC/GS2.1. There are two radio sources (GS2.1a and GS2.1b) within the 4.5 arcsec search radius, each with a high likelihood of being the AzTEC counterpart. The westernmost source GS2.1a with a red IRAC colour ($[3.6\,\mu m] - [4.5\,\mu m] = +0.38$) is a robust identification ($P_{1.4} = 0.001$). The 870 μm LABOCA source LESS J033219.0−275219 ($S_{870\,\mu m} = 9.1 \pm 1.2$ mJy) position is only 4.8 arcsec away from GS2.1a. The adjacent, second faint radio source GS2.1b is an extremely rare example of a faint radio source without any counterpart in the IRAC and MIPS images. Both radio sources are formally considered robust counterparts by our analysis and by Biggs et al. (2011). There are two additional faint radio sources just outside the search radius, making this an

exceptionally crowded field in the radio band. These two more distant radio sources have the same spectroscopic redshift of $z = 1.097$ (Le Fevre et al. 2004; Norris et al. 2006), and their blue IRAC colour, $[3.6\,\mu m] - [4.5\,\mu m] = -0.27$ suggests that they are indeed foreground sources. The catalogue position for the BLAST 250 μm source 59 (Dunlop et al. 2010) is located near the peak of the AzTEC/GS2 contours but between the two deconvolved components AzTEC/GS2.1 and AzTEC/GS2.2. A third potential counterpart, GS2.1c, identified by MIPS 24 μm detection is only 3.9 arcsec from the AzTEC centroid; however, it has a blue IRAC colour ($[3.6\,\mu m] - [4.5\,\mu m] = -0.32$) with a spectroscopic redshift of $z = 0.644$, and is likely a foreground object.

AzTEC/GS2.2. There are no radio sources within 15 arcsec of AzTEC/GS2.2. The MIPS 24 μm source GS2.2a is a potential counterpart with $P_{24\,\mu m} = 0.212$ with a blue IRAC colour ($[3.6\,\mu m] - [4.5\,\mu m] = -0.23$) and a spectroscopic redshift of $z = 1.046$ (Popesso et al. 2009). Therefore, it is likely a member of the foreground $z = 1.10$ cluster GCL J0332.2−2752 ($\sigma_v = 433\,\mathrm{km\,s^{-1}}$; Diaz-Sanchez et al. 2007) whose centre is located only ~20 arcsec to the north-east, at $\alpha = 03^h32^m17\fs5$ and $\delta = -27°52'32''$. This MIPS source is blended with a second IRAC source located 3 arcsec to the south-west, GS2.2b, which has a red IRAC colour ($[3.6\,\mu m] - [4.5\,\mu m] = +0.26$; $P_{colour} = 0.390$). GS2.2b is also a BzK galaxy and thus is an actively star-forming system. The IRAC source GS2.2c is another BzK galaxy with a red IRAC colour ($[3.6\,\mu m] - [4.5\,\mu m] = +0.10$) and is an interesting alternative counterpart, though $P_{colour} = 0.439$. The closest 870 μm LABOCA source LESS J033217.6−275230 ($S_{870\,\mu m} = 6.3 \pm 1.3$ mJy) position is 15 arcsec north-east of the AzTEC centroid, nearly centred on the $z = 1.1$ cluster. The position of AzTEC/GS2.2, however, is very uncertain as it is blended with AzTEC/GS2.1, so the counterpart identification is highly problematic.

AzTEC/GS3. The faint IRAC source GS3a ($S_{1.4\,\mathrm{GHz}} = 40.7 \pm 6.5\,\mu\mathrm{Jy}$; $P_{1.4} = 0.045$) is also a MIPS 24 μm source with a red IRAC colour ($[3.6\,\mu m] - [4.5\,\mu m] = +0.37$; $P_{colour} = 0.174$). The 870 μm LABOCA source LESS J033248.1−275414 ($S_{870\,\mu m} = 8.8 \pm 1.2$ mJy) is only 2.4 arcsec away from GS3a, leading Biggs et al. (2011) to conclude this source as a secure counterpart as well. Dunlop et al. (2010) also identified GS3a as the counterpart to the 250 μm BLAST source 593 and estimated a redshift $z > 2.5$ for this optically invisible source. Our radio-mm photometric redshift of $z_{MR} = 3.09^{+0.55}_{-1.11}$ supports this high-z hypothesis. There is a faint red IRAC source, GS3b, which is also a tentative detection that cannot be ruled out.

AzTEC/GS4. There is only one red IRAC source (GS4a; $P_{colour} = 0.070$) within the 6.5 arcsec search radius. It is a faint radio emitter ($S_{1.4\,\mathrm{GHz}} = 25.4 \pm 6.5\,\mu\mathrm{Jy}$, $P_{1.4} = 0.021$). There are two other radio sources within 17 arcsec from the AzTEC position, but GS4a is the only source falling within the error circle of the 870 μm LABOCA source LESS J033249.2−274246 ($S_{870\,\mu m} = 8.8 \pm 1.2$ mJy). Therefore GS4a is a robust counterpart for the AzTEC source although it is only a tentative counterpart for the LABOCA source (Biggs et al. 2011). This is another high-z candidate source with $z_{opt} = 3.37 \pm 0.25$ and $z_{MR} = 3.53^{+0.57}_{-1.27}$.

AzTEC/GS5. There is a single tentative counterpart within the 7.1 arcsec search radius from the AzTEC/GS5 position. However, the AzTEC contours are elongated in the east–west direction, joining the two VLA radio sources GS5a and GS5b. Both radio sources have red IRAC counterparts, and both sources may contribute to the AzTEC emission. The 870 μm LABOCA source LESS J033150.8−274438 ($S_{870\,\mu m} = 3.9 \pm 1.4$ mJy) is located only 4.1 arcsec away from GS5a (also a *Chandra* X-ray source), and

Biggs et al. (2011) and Chapin et al. (2011) also identify GS5a as the secure counterpart to the LABOCA source. Casey et al. (2011) reported a spectroscopic redshift of $z = 1.599$ for GS5a based on some absorptions features, and this redshift is further supported by the 9 h long integration VLT spectrum by Silverman et al. (2010).

AzTEC/GS6. The IRAC/MIPS source GS6b is located only 0.4 arcsec from the AzTEC/GS6 centroid. However, its blue IRAC colour ($[3.6\,\mu m] - [4.5\,\mu m] = -0.23$) and spectroscopic redshift of $z = 1.102$ (Stern et al., in preparation) suggest that GS6b is likely a foreground object. At a distance of 12.4 arcsec, the IRAC/MIPS source GS6a is located outside the 7.5 arcsec formal search radius for a counterpart, but it has very red IRAC colour ($[3.6\,\mu m] - [4.5\,\mu m] = +0.45$) and is a faint radio source ($S_{1.4\,\mathrm{GHz}} = 31.0 \pm 6.3\,\mu\mathrm{Jy}$; $P_{1.4} = 0.268$). Biggs et al. (2011) identify GS6a as the robust counterpart for the 870 μm LABOCA source LESS J033225.7−275228 ($S_{870\,\mu m} = 5.8 \pm 1.4$ mJy) located 6.2 arcsec away, and this galaxy is likely the primary counterpart to the AzTEC source as well.

AzTEC/GS7. The red IRAC/MIPS source GS7a is the only radio source within the 8.7 arcsec search radius ($S_{1.4\,\mathrm{GHz}} = 51.2 \pm 6.4\,\mu\mathrm{Jy}$; $P_{1.4} = 0.126$). Therefore, it is considered a tentative counterpart to AzTEC/GS7. The spectroscopic redshift of GS7a, which is also identified as a *Chandra* X-ray source, is $z = 2.676$, in excellent agreement with its radio-mm photometric redshift of $z_{MR} = 2.56^{+0.52}_{-0.92}$. The 870 μm LABOCA source LESS J033213.6−275602 ($S_{870\,\mu m} = 9.1 \pm 1.2$ mJy) is located only 4.2 arcsec away, and Biggs et al. (2011) also identify GS7a as a robust counterpart. A second possible counterpart, GS7b, is a red IRAC/MIPS source ($P_{24\,\mu m} = 0.151$, $P_{colour} = 0.168$) located on the other side of the AzTEC centroid and may contribute to the observed 1100 μm emission.

AzTEC/GS8. There is a single robust radio counterpart GS8a, 4.4 arcsec from the AzTEC centroid position with $P_{1.4} = 0.038$. The IRAC/MIPS counterpart GS8a also has a red IRAC colour ($[3.6\,\mu m] - [4.5\,\mu m] = +0.33$) and relatively bright MIPS 24 μm emission ($S_{24\,\mu m} = 620\,\mu\mathrm{Jy}$; $P_{24\,\mu m} = 0.203$). Both Chapin et al. (2011) and Biggs et al. (2011) have identified this $z = 2.252$ galaxy as the counterpart to the 870 μm LABOCA source LESS J033205.1−274652 ($S_{870\,\mu m} = 7.5 \pm 1.2$ mJy), located only 7.7 arcsec away from AzTEC position. The second IRAC/MIPS source GS8b located 2.9 arcsec from the AzTEC position, is also a plausible MIPS 24 μm counterpart ($P_{24\,\mu m} = 0.089$) with red IRAC colour and is also a *Chandra* X-ray source.

AzTEC/GS9. The single tentative radio counterpart ($S_{1.4} = 86.8 \pm 6.6\,\mu\mathrm{Jy}$; $P_{1.4} = 0.070$) is associated with a red IRAC/MIPS source GS9a, located 6.2 arcsec from the AzTEC centroid position. It is also a *Chandra*-detected X-ray source and should be considered a strong candidate for the AzTEC counterpart. Located only 3.5 arcsec away from the AzTEC centroid, the IRAC/MIPS source GS9b is an intriguing alternate counterpart candidate given its red IRAC colour ($[3.6\,\mu m] - [4.5\,\mu m] = +0.29$) and MIPS 24 μm emission. If GS9b is the primary source of 1100 μm continuum emission, then it is likely to be a high-redshift system as its radio non-detection requires $z_{MR} > 3.3$. Slightly further away is GS9c, also a tentative red IRAC source. No nearby source is found in the 870 μm LABOCA catalogue, but the LABOCA map shows a S/N = 3.0 peak (3.4 ± 1.2 mJy) at the position of GS9a.

AzTEC/GS10. There is a single robust radio counterpart to AzTEC/GS10, located 5.3 arcsec from the AzTEC centroid ($S_{1.4} = 89.3 \pm 6.4\,\mu\mathrm{Jy}$; $P_{1.4} = 0.053$). Its red IRAC/MIPS counterpart GS10a ($[3.6\,\mu m] - [4.5\,\mu m] = +0.14$) has a reported spectroscopic redshift of $z = 0.0338$ in the GOODS/ESO VIMOS DR1

catalogue (Popesso et al. 2009), but the same group revised its redshift to $z = 2.035$ using new data (Balestra et al. 2010). This revised spectroscopic redshift is in excellent agreement with our photometric redshift, $z_{MR} = 2.03^{+0.41}_{-0.75}$. Another red IRAC source GS10b ($[3.6\,\mu m] - [4.5\,\mu m] = +0.04$; $P_{colour} = 0.077$), located only 3.2 arcsec away from the AzTEC position, is not detected in the radio or by MIPS. The 870 μm LABOCA source LESS J033207.6−275123 ($S_{870\,\mu m} = 7.6 \pm 1.3$ mJy) is located only 4.3 arcsec away from GS10a, and it is also identified as a robust LABOCA counterpart by Biggs et al. (2011).

AzTEC/GS11. There is a single tentative VLA radio counterpart for this source located 6.5 arcsec from the AzTEC centroid ($S_{1.4} = 46.0 \pm 6.4\,\mu Jy$; $P_{1.4} = 0.081$), and it is also a *Chandra* X-ray source. Its IRAC/MIPS counterpart GS11a has a slightly blue colour ($[3.6\,\mu m] - [4.5\,\mu m] = -0.02$), but the VLT ISAAK K-band image (Retzlaff et al. 2010) shows that this IRAC source is a blend of an optically bright ($i = 21.7$) $z = 0.246$ foreground source and an optically faint source second source, which is the radio source. The 250 μm BLAST source 109, located ∼30 arcsec south-east of the AzTEC centroid, is undetected at longer wavelength bands and is identified with a $z = 0.124$ foreground disc galaxy (Dunlop et al. 2010). Our photometric redshift for GS11a, $z_{MR} = 2.50^{+0.52}_{-0.88}$, is completely inconsistent with this identification, and the proposed BLAST counterpart is unlikely to be related to the AzTEC source. No nearby source is found in the 870 μm LABOCA catalogue, but the LABOCA map shows a S/N ∼ 3 peak (3.5 ± 1.2 mJy) at the position of GS11a.

AzTEC/GS12. The most likely counterpart candidate is a faint radio, red IRAC source GS12a located 4.0 arcsec away from the AzTEC position with $[3.6\,\mu m] - [4.5\,\mu m] = +0.10$. This $z = 4.762$ galaxy was also identified as the counterpart to the LABOCA 870 μm survey source LESS J033229.3−275619 ($S_{870\,\mu m} = 5.1 \pm 1.4$ mJy) by Coppin et al. (2009) based on its proximity to the LABOCA position and the presence of a ∼3σ radio source. Redshifted CO emission at $z_{CO} = 4.755$ has been reported by Coppin et al. (2010a), lending further support for the counterpart identification.

AzTEC/GS13. There is a high concentration of IRAC/MIPS sources with spectroscopic redshifts between 1.0 and 1.6 in the region surrounding AzTEC/GS13. The most likely counterpart for AzTEC/GS13 is a red IRAC/MIPS source GS13a ($[3.6\,\mu m] - [4.5\,\mu m] = +0.24$), located only 2.1 arcsec away from the AzTEC centroid. This source is also a faint radio source with no known spectroscopic redshift. A second IRAC/MIPS source GS13b is a *Chandra* X-ray source at $z = 1.039$ (Mignoli et al. 2005), but its statistical likelihood of being the AzTEC counterpart is lower (see Table 1). A third candidate counterpart, GS13c, is a faint radio source, but it has a blue IRAC colour ($[3.6\,\mu m] - [4.5\,\mu m] = -0.25$) and is therefore likely a foreground source. The 250 μm BLAST source 193 is located ∼25 arcsec south of the AzTEC position. Although the low density of the AzTEC and BLAST sources make the chance coincidence of these two sources even at such a substantial separation small, few plausible candidates are found within the BLAST position error circle. No nearby source is found in the 870 μm LABOCA catalogue, but the LABOCA map shows a S/N ∼ 3 peak (3.6 ± 1.2 mJy) near the AzTEC centroid position.

AzTEC/GS14. There are no radio sources within the 9.0 arcsec search radius. The only tentative counterpart is a faint, red IRAC source GS14a ($[3.6\,\mu m] - [4.5\,\mu m] = +0.04$; $P_{colour} = 0.083$) located only 3.1 arcsec from AzTEC/GS14. Although no nearby source is found in the 870 μm LABOCA catalogue, the LABOCA map shows a S/N ∼ 3 peak (3.3 ± 1.2 mJy) nearly coincident with

this position. The previously unpublished redshift of $z = 3.640$ (Keck LRIS spectrum; Spinrad, private communication) for GS14a is consistent with its photo-z $z_{opt} = 3.50 \pm 0.30$ and the non-detection in the radio and the MIPS 24 μm bands, similar to the $z = 4.762$ AzTEC/LABOCA source GS12a.

AzTEC/GS15. There are several faint, red IRAC/MIPS sources within the 9.0 arcsec search radius, although they are individually not particularly compelling. The faint radio source GS15a, although 12.7 arcsec from the AzTEC centroid, is also a *Chandra* X-ray source and is located 1.4 arcsec from the centroid of the LABOCA 870 μm source LESS J033151.5−274552 ($S_{870\,\mu m} = 4.2 \pm 1.4$ mJy), and GS15a is the secure LABOCA counterpart (Biggs et al. 2011).

AzTEC/GS16. There are two faint radio sources within the counterpart search radius of 10.5 arcsec. The red IRAC/MIPS source GS16a ($[3.6\,\mu m] - [4.5\,\mu m] = +0.53$) is 6.1 arcsec away from the AzTEC position, and it is a tentative radio counterpart with $P_{1.4} = 0.072$. GS16a is also an X-ray source detected by *Chandra* and has a spectroscopic redshift of $z = 1.719$ (Silverman et al., in preparation). The second radio source GS16b is located slightly further away, 7.9 arcsec. Although it is a brighter MIPS 24 μm source, it has a blue IRAC colour ($[3.6\,\mu m] - [4.5\,\mu m] = -0.29$) and a spectroscopic redshift of $z = 1.017$ (Mignoli et al. 2005), suggesting it is a foreground source. No nearby source is found in the 870 μm LABOCA catalogue, but the LABOCA map shows a S/N ∼ 2 peak near the position of G16a.

AzTEC/GS17. Two plausible IRAC/MIPS sources are found within the 10.5 arcsec search radius. The IRAC/MIPS source GS17a is a faint radio source with $P_{1.4} = 0.007$, making it formally a robust identification. However, it has a blue IRAC colour with $[3.6\,\mu m] - [4.5\,\mu m] = -0.27$ and is thus likely a foreground object($z_{opt} = 1.01 \pm 0.10$). The IRAC/MIPS source GS17b is another robust identification based on the MIPS detection ($P_{24\,\mu m} = 0.026$) and red IRAC colour ($[3.6\,\mu m] - [4.5\,\mu m] = +0.19$, $P_{colour} = 0.021$), and this *Chandra* detected X-ray source has a photometric redshift of $z = 2.66$ (Silverman et al. 2010). Though slightly further from the AzTEC centroid, GS17c is an interesting alternative possibility: this red IRAC/MIPS source ($[3.6\,\mu m] - [4.5\,\mu m] = +0.36$) has optical colours satisfying the BzK criteria for star-forming galaxies at high redshifts. There is also a close pair of radio sources, GS17d and GS17e, located 12 arcsec north of the AzTEC position; though they are outside the nominal search radius, both have red IRAC colours and remain plausible counterparts to the AzTEC source. No nearby source is found in the 870 μm LABOCA catalogue, but the LABOCA map shows a S/N ∼ 3 emission peak between GS17b and the two radio sources GS17d and GS17e.

AzTEC/GS18. There are two faint radio sources within the 9.3 arcsec search radius of AzTEC/GS18. The closest IRAC/MIPS source GS18a is formally a robust counterpart owing to its proximity to the AzTEC position and its very red IRAC colour ($[3.6\,\mu m] - [4.5\,\mu m] = +0.47$, $P_{colour} = 0.113$). Additionally, GS18b is a $z = 2.688$ galaxy which is an X-ray source detected by *Chandra* (Akiyama 2005) and has a red IRAC colour ($[3.6\,\mu m] - [4.5\,\mu m] = +0.31$), making it a plausible candidate for the counterpart to AzTEC/GS18. A third radio-faint IRAC/MIPS source GS18c is a tentative candidate based on its MIPS 24 μm emission, but it has very blue colour ($[3.6\,\mu m] - [4.5\,\mu m] = -0.39$) and is likely a foreground object. The 870 μm LABOCA source LESS J033243.6−274644 ($S_{870\,\mu m} = 6.4 \pm 1.3$ mJy) is located ∼8.4 arcsec south of the AzTEC position, putting GS18a between the AzTEC and LABOCA centroids. Biggs et al. (2011) identified GS18a as a tentative (and only) counterpart to the LABOCA source.

This extremely faint optical source ($i = 28.1$, $K > 24.5$) is another high-z candidate with $z_{MR} = 3.00^{+0.56}_{-1.14}$.

AzTEC/GS19. A pair of radio sources, GS19a and GS19b (with $P_{1.4} = 0.102$ and $P_{1.4} = 0.143$, respectively), is strongly favoured as the counterparts to AzTEC/GS19 when all statistical measures are taken into account. They form a blended source in the MIPS 24 μm band, and both have red IRAC colours. It is possible that these two sources are physically related and both contribute to the AzTEC emission. No spectroscopic redshift is available for either sources while their photometric redshifts are quite similar ($z_{opt} = 1.83 \pm 0.35 \& 2.08 \pm 0.25$). At $z = 2.0$, their projected separation of 3.2 arcsec corresponds to 27 kpc. There is a third IRAC/MIPS counterpart, GS19c, that is a tentatively counterpart with a lower likelihood ($P_{24 \mu m} = 0.181$). No nearby source is found in the 870 μm LABOCA catalogue, but the LABOCA map shows a S/N ~ 2.4 emission peak near GS19a and GS19b.

AzTEC/GS20. The AzTEC contours are well centred and follow the light profile of the $z = 0.0369$ galaxy GS20a, which is also a bright and well resolved radio, MIPS 24 and 70 μm, and X-ray source. This source is quite blue ($[3.6 \,\mu m] - [4.5 \,\mu m] = -0.43$) and is obviously a bright foreground galaxy. It is the brightest BLAST 250 μm source within the GOODS-South survey field proper, and Dunlop et al. (2010) argue that this foreground galaxy is the correct counterpart for the BLAST source. It is possible that the 1.1 mm emission originates from the cold dust associated with this spiral galaxy (as seen in the *HST* images), but it is difficult to reproduce the entire measured SED from $\lambda = 1 \,\mu m$ to 20 cm using a reasonable set of assumptions on dust temperature, IR luminosity and SFR for this low-redshift galaxy. Instead, the AzTEC emission may originate from a background object, possibly lensed by this foreground galaxy, similar to AzTEC J100008.05+022612.2 imaged at high angular resolution by Younger et al. (2007).

AzTEC/GS21. The single tentative radio counterpart (GS21a) has $[3.6 \,\mu m] - [4.5 \,\mu m] = +0.24$ and a spectroscopic redshift of $z = 1.910$ (Vanzella et al. 2008). The position centroid of the BLAST 250 μm source 861 is displaced by ~ 7 arcsec to the north-east, but GS21a is still within the error-circle of the BLAST source. No nearby source is found in the 870 μm LABOCA catalogue, but the LABOCA map shows a S/N ~ 1.8 emission peak near GS21a. A second tentative counterpart GS21b is a red IRAC/MIPS galaxy located just 2.5 arcsec away from the AzTEC centroid.

AzTEC/GS22. The faint radio source GS22a, located 7.8 arcsec away from the AzTEC centroid, is the most likely counterpart ($S_{1.4} = 34.6 \pm 6.5 \,\mu Jy$). This galaxy is also a red IRAC/MIPS source ($[3.6 \,\mu m] - [4.5 \,\mu m] = +0.30$) and has a spectroscopic redshift of $z = 1.794$ (Wuyts et al. 2009). The 250 μm BLAST source 552 position centroid is ~ 10 arcsec east of the AzTEC position, and Dunlop et al. (2010) also identified the radio source GS22a (located ~ 7 arcsec away from the BLAST position) as the likely counterpart. A second red IRAC/MIPS candidate counterpart, GS22b, is closer to the AzTEC centroid and is an interesting alternative. No nearby source is found in the 870 μm LABOCA catalogue, but the LABOCA map shows a S/N ~ 3.1 emission peak near this red IRAC/MIPS source GS22b.

AzTEC/GS23. The faint radio source GS23a ($S_{1.4} = 23.4 \pm 6.5 \,\mu Jy$; $P_{1.4} = 0.030$) is a robust counterpart, and its red IRAC colour ($[3.6 \,\mu m] - [4.5 \,\mu m] = +0.45$) adds to the high likelihood of being the correct counterpart. A second tentative radio counterpart, GS23b is only slightly further from the AzTEC centroid, and it is a red IRAC/MIPS source with a spectroscopic redshift of $z = 2.277$ (Chapin et al. 2011). Both GS23a and GS23b are within the beam area of the 870 μm LABOCA source LESS J033221.3−275623

($S_{870 \,\mu m} = 4.7 \pm 1.4$ mJy) and the 250 μm BLAST source 158. Dunlop et al. (2010) and Biggs et al. (2011) have identified GS23b as the counterpart consisting of 'an extremely complex faint system' at optical wavelengths.

AzTEC/GS24. There is a single tentative faint radio counterpart within the 12.2 arcsec counterpart search radius, GS24a. This red IRAC/MIPS source is the most likely counterpart to AzTEC/GS24. The 250 μm BLAST source 104 straddles GS24a and a $z = 2.578$ type 2 QSO J033235.78−274916.82 (Rigopoulou et al. 2009, also detected at MIPS 70 μm), and both sources likely contribute to the 250 μm continuum. Dunlop et al. (2010) instead identified the $z = 0.547$ radio source located at the edge of the AzTEC and BLAST beam based on the radio P statistic. No nearby source is found in the 870 μm LABOCA catalogue, but the LABOCA map shows a S/N ~ 3 emission peak near the $z = 2.578$ type 2 IR QSO J033235.78−274916.82 and a secondary S/N ~ 2 emission peak near GS24a. The AzTEC contours are elongated in the north–south direction, and this may be another example of a blended source.

AzTEC/GS25. The red IRAC/MIPS source associated with radio emission GS25a is located only 6.8 arcsec away from the AzTEC centroid position. This galaxy, also detected in the X-ray by *Chandra*, has a spectroscopic redshift of $z = 2.292$ (Popesso et al. 2009). The 870 μm LABOCA source LESS J033246.7−275120 ($S_{870 \,\mu m} = 5.9 \pm 1.3$ mJy) is well centred on GS25a, and Biggs et al. (2011) also identify the same galaxy as the robust LABOCA counterpart.

AzTEC/GS26. AzTEC/GS26 has no radio counterpart within the 12.2 arcsec search radius of the AzTEC position, but there are five red IRAC sources. Of these, GS26a ($[3.6 \,\mu m] - [4.5 \,\mu m] = +0.22$; $P_{colour} = 0.237$) located 5.5 arcsec away is the most probable counterpart to this AzTEC source. GS26b and GS26c are other red IRAC sources located slightly further away (~ 7 arcsec). No nearby source is found in the 870 μm LABOCA catalogue, but the LABOCA map shows a S/N ~ 2.9 emission peak near the $z = 2.331$ MIPS galaxy J033216.3−274343.4 with a red IRAC colour ($[3.6 \,\mu m] - [4.5 \,\mu m] = +0.35$), located ~ 7.5 arcsec away from the AzTEC position.

AzTEC/GS27. The red IRAC/MIPS source GS27a ($[3.6 \,\mu m] - [4.5 \,\mu m] = +0.38$) is located 13.0 arcsec away from the AzTEC centroid, just within the counterpart search radius of 13.0 arcsec, and is associated with weak radio emission ($S_{1.4} = 23.6 \pm 6.5 \,\mu Jy$) from a $z = 2.577$ (Popesso et al. 2009) galaxy. However, formally this is not a secure identification ($P_{1.4} > 0.20$) owing to its large separation from the AzTEC centroid. Still, this is the most plausible counterpart within the proximity of AzTEC/GS27. No nearby source is found in the 870 μm LABOCA catalogue, but the LABOCA map shows a S/N ~ 3.1 emission peak near this red IRAC/MIPS source GS27a.

AzTEC/GS28. AzTEC/GS28 has no radio source within the 13.0 arcsec counterpart search radius. The red IRAC sources GS28a ($[3.6 \,\mu m] - [4.5 \,\mu m] = +0.55$; $P_{colour} = 0.073$) and GS28b ($[3.6 \,\mu m] - [4.5 \,\mu m] = +0.07$; $P_{colour} = 0.136$) are the most likely counterparts. No nearby source is found in the 870 μm LABOCA catalogue, but the LABOCA map shows an extended source with a S/N ~ 3.0 emission peak near the AzTEC source position, and this may be another blended source.

AzTEC/GS29. There are no compelling counterparts to AzTEC/GS29. The closest IRAC/MIPS source GS29a (3.8 arcsec away) is very blue ($[3.6 \,\mu m] - [4.5 \,\mu m] = -0.43$) and has a spectroscopic redshift of $z = 0.577$, so this is likely a foreground source. The next closest source GS29b is a $z = 2.340$ galaxy located 4.6 arcsec

away, but it is also blue ($[3.6\,\mu m] - [4.5\,\mu m] = -0.10$). There are two radio sources located just outside the 13.0 arcsec search radius, but they both have relatively high probabilities of being false associations. No nearby source is found in the 870 μm LABOCA catalogue, but the LABOCA map shows an extended source with two S/N $\sim$2-3 emission peaks near the red IRAC/MIPS sources J033158.65$-$274516.3 and J033200.13$-$274453.2.

AzTEC/GS30. The brightest MIPS 24 μm source within the counterpart search radius of 13.5 arcsec ($S_{24\,\mu m} = 459 \pm 6\,\mu Jy$; $P_{24\,\mu m} = 0.44$) is also a faint radio source ($S_{1.4} = 37.2 \pm 6.2\,\mu Jy$; $P_{1.4} = 0.082$) with a red IRAC colour ($[3.6\,\mu m] - [4.5\,\mu m] = +0.19$). Therefore, GS30a is a tentative but the most plausible counterpart for AzTEC/GS30. The spectroscopic redshift of this galaxy is yet unknown. A second radio source (GS30b) and a radio-faint IRAC source (GS30c) are also tentative counterparts to AzTEC/GS30, both with red IRAC colours. No nearby source is found in the 870 μm LABOCA catalogue, but the LABOCA map shows an extended source with a S/N = 2.9 centred on the AzTEC centroid position.

AzTEC/GS31. Both of the two bright MIPS 24 μm sources (GS31b) within the 13.6 arcsec search radius region are associated with faint radio emission. The western source GS31a however is closer (2.7 arcsec) to the AzTEC centroid, making it a robust counterpart candidate ($P_{1.4} = 0.015$). The eastern source GS31b is located 7.9 arcsec away and is a tentative counterpart ($P_{1.4} = 0.118$). It is possible that both sources contribute to the 1.1 mm emission detected by AzTEC. They both have *blue* IRAC colours ($[3.6\,\mu m] - [4.5\,\mu m] = -0.25$ and -0.36 for GS31a and GS31b, respectively) however, and the true counterpart may be a much fainter source located between or behind these sources. The spectroscopic redshift of GS31a is $z = 1.843$ (Wuyts et al. 2009). No nearby source is found in the 870 μm LABOCA catalogue, but the LABOCA map shows an elongated north–south structure with a S/N = 2.8 peak, similar to the AzTEC source morphology, and it is likely another blended source.

AzTEC/GS32. There are three radio counterparts within the 13.5 arcsec search radius of the AzTEC centroid, and all three are also MIPS 24 μm sources. The nearest radio source GS32a ($S_{1.4} = 30.3 \pm 6.8\,\mu Jy, P_{1.4} = 0.162$; and $S_{24\,\mu m} = 371.1 \pm 11.7\,\mu Jy$, $P_{24\,\mu m} = 0.421$), located 9.6 arcsec away from the AzTEC centroid, is the primary candidate by its proximity. The source GS32b is similarly bright in radio and MIPS 24 μm bands, but it is slightly further away, 10.5 arcsec, from the AzTEC centroid position. Both GS32a and GS32b are quite blue, however; we include GS32c, a faint radio galaxy with red IRAC colour, in the catalogue as an alternative, although it is located 13.4 arcsec from the AzTEC centroid. No nearby source is found in the 870 μm LABOCA catalogue, and no significant emission peak is found at this location in the LABOCA map.

AzTEC/GS33. The faint IRAC source GS33a located 7.4 arcsec from the AzTEC centroid position is associated with a weak radio source ($S_{1.4} = 28.6 \pm 6.2\,\mu Jy$). It is also a weak MIPS 24 μm source and has a red IRAC colour ($[3.6\,\mu m] - [4.5\,\mu m] = +0.34$; $P_{colour} = 0.390$). Therefore, this galaxy is a tentative candidate counterpart for AzTEC/GS33. No nearby source is found in the 870 μm LABOCA catalogue, but the LABOCA map shows an isolated emission peak with S/N $\sim$ 2.3 centred near GS33a.

AzTEC/GS34. There is a high density of IRAC sources in this field, but few are located in the immediate vicinity of the AzTEC centroid position. There are no robust or tentative counterparts to AzTEC/GS34: $P > 0.20$ for all sources within the 13.5 arcsec search

radius. No nearby source is found in the 870 μm LABOCA catalogue, but the LABOCA map shows an emission peak with a S/N $\sim$ 3.5 centred near the $z = 1.356$ (Silverman et al., in preparation) faint radio and MIPS source GS34a.

AzTEC/GS35. The red IRAC source GS35a, located 2.0 arcsec away from the AzTEC source centroid position, has a robust radio counterpart ($S_{1.4} = 41.3 \pm 6.7\,\mu Jy$; $P_{1.4} = 0.008$). Its MIPS emission ($P_{24\,\mu m} = 0.027$) and red IRAC colour ($[3.6\,\mu m] - [4.5\,\mu m] = +0.37$; $P_{colour} = 0.022$) make this galaxy a robust counterpart to the AzTEC source. Its spectroscopic redshift is unknown. The second red IRAC source GS35b located 4.9 arcsec away from the AzTEC position ($P_{colour} = 0.191$) is undetected at radio or MIPS 24 μm bands. No nearby source is found in the 870 μm LABOCA catalogue, and the LABOCA map shows an emission peak with a S/N $\sim$ 2.1 centred near the $z = 0.734$ radio-loud QSO J033227.00$-$274105.0.

AzTEC/GS36. No radio source is detected within the 13.5 arcsec counterpart candidate search radius, and the galaxy GS36a is the only IRAC source with a red IRAC colour, $[3.6\,\mu m] - [4.5\,\mu m] = +0.68$ ($P_{colour} = 0.304$). So this IRAC source is the most promising counterpart candidate, although it has a high probability of false association. Few other potential candidates are present in this field. No nearby source is found in the 870 μm LABOCA catalogue, and the LABOCA map does not show any significant emission peak within the search radius.

AzTEC/GS37. The red IRAC/MIPS source GS37a with $[3.6\,\mu m] - [4.5\,\mu m] = +0.08$ is associated with faint radio emission ($S_{1.4} = 20.5 \pm 6.4\,\mu Jy$), though it is not formally a tentative counterpart candidate for AzTEC/GS37. There is a single tentative red IRAC source 4.3 arcsec from the AzTEC centroid, which is possibly at high redshift ($z > 3$) given its non-detection at 1.4 GHz. No nearby source is found in the 870 μm LABOCA catalogue, but the LABOCA map shows a ridge of 2.1–2.7σ peaks running along the similar ridge found in the AzTEC map (including GS37a), suggesting this is likely another blended source.

AzTEC/GS38. There is a single tentative radio counterpart (GS38a; $P_{1.4} = 0.116$), which is also a *Chandra* X-ray source. It has a very blue IRAC colour ($[3.6\,\mu m] - [4.5\,\mu m] = -0.55$) and a spectroscopic redshift of $z = 0.735$ (Vanzella et al. 2008). Therefore, GS38a is likely a foreground object. No nearby source is found in the 870 μm LABOCA catalogue, but the LABOCA map shows a 2.3σ peak near the red IRAC/MIPS source GS38b, located 7.4 arcsec away from the AzTEC centroid ($P_{24\,\mu m} = 0.453$, $P_{colour} = 0.386$).

AzTEC/GS39. There is a single tentative radio counterpart (GS39a; $P_{1.4} = 0.083$) which is also a red IRAC source ($[3.6\,\mu m] - [4.5\,\mu m] = +0.55$). The position centroid of the 870 μm LABOCA source LESS J033154.4$-$274525 ($S_{870\,\mu m} = 3.8 \pm 1.4$ mJy) is offset from GS39a by only 4.9 arcsec. Biggs et al. (2011) also identify GS39a as a tentative LABOCA counterpart, and GS39a is a strong counterpart candidate for AzTEC/GS39. Another tentative counterpart, GS39b, is a MIPS source located only 2.8 arcsec from the AzTEC centroid, but given its blue colour, it is likely a foreground object.

AzTEC/GS40. There are no compelling counterparts to AzTEC/GS40. We list a single IRAC source within the 15.0 arcsec search radius. GS40a is 10.2 arcsec away, and is slightly blue with a high probability of being a false association. No nearby source is found in the 870 μm LABOCA catalogue, and the LABOCA map shows only a 2σ emission peak located $\sim$10 arcsec north-west of the AzTEC position.

AzTEC/GS41. The radio sources GS41a and GS41b are both promising counterparts to AzTEC/GS41 with $P_{1.4} = 0.120$ & 0.132.

They are also red IRAC sources with [3.6 μm] − [4.5 μm] = +0.23 and +0.30 although they are just far enough away from the AzTEC centroid to make them tentative counterparts only. Two other red IRAC sources GS41c and GS41d are slightly closer to the AzTEC centroid and are tentative counterparts as well. The centroid of the 870 μm LABOCA source LESS J033302.5−275643 ($S_{870\,\mu m} = 12.0 \pm 1.2$ mJy) is located closest to GS41b and GS41d, and Biggs et al. (2011) identify GS41b as the robust counterpart to the LABOCA source.

AzTEC/GS42. There are no radio counterparts within the 6.9 arcsec search radius of AzTEC/GS42. The only tentative counterpart is GS42a, a red IRAC source ([3.6 μm] − [4.5 μm] = +0.04) that is also well matched to the position of the LABOCA source LESS J033314.3−275611 ($S_{870\,\mu m} = 14.5 \pm 1.2$ mJy). The AzTEC contours are extended in the north–south direction, and Weiss et al. (2009) modelled this source with a second, fainter component (LESS J033313.0−275556, $S_{870\,\mu m} = 4.3 \pm 1.4$ mJy). Biggs et al. (2011) identified adjacent red IRAC/MIPS source J033314.41−275612.0 as the robust LABOCA counterpart.

AzTEC/GS43. The only tentative counterpart is a red IRAC source GS43a, which has a red IRAC colour ([3.6 μm] − [4.5 μm] = +0.23) and is also centred on the 870 μm LABOCA source LESS J033302.9−274432 ($S_{870\,\mu m} = 6.7 \pm 1.3$ mJy). Since this object is undetected in the radio and MIPS 24 μm, it is also likely a high-redshift object ($z_{MR} > 4.1$). Biggs et al. (2011) did not find any robust or tentative counterpart for the LABOCA source. The AzTEC contours are significantly elongated in the east–west direction, suggesting this is a blend of more than one source. Weiss et al. (2009) model this source with a fainter second component, LESS J033303.9−274412 ($S_{870\,\mu m} = 5.3 \pm 1.4$ mJy).

AzTEC/GS44. There is only one VLA radio source found within the 10.4 arcsec search radius centred on the AzTEC peak position. This source GS44a has a flat IRAC colour, [3.6 μm] − [4.5 μm] = −0.07 and is a modest MIPS 24 μm source with $S_{24\,\mu m} = 143.1 \pm 9.3$ μJy. The 870 μm LABOCA source LESS J033240.4−273802 ($S_{870\,\mu m} = 5.0 \pm 1.4$ mJy) is found within the AzTEC search radius, but its centroid is offset from GS44a by 12 arcsec, just outside the nominal beam area of LABOCA. Another radio source J033239.14−273810.5 at $z = 0.830$ (Le Fevre et al. 2004) is a better candidate for the LABOCA counterpart, but this radio source is located 24 arcsec away from the AzTEC centroid, which is well outside the nominal search radius for the AzTEC source. We list the LABOCA flux in the table, but note the large separation between this source and GS44a.

AzTEC/GS45. Two red IRAC/MIPS sources (GS45b and GS45c) are found within 2 arcsec of the AzTEC centroid, and they are the most likely candidate counterparts to the AzTEC source, primarily by their proximity. The 870 μm LABOCA source LESS J033218.9−273738 ($S_{870\,\mu m} = 8.1 \pm 1.2$ mJy) is found within the AzTEC search radius, half way between GS45b and GS45a, the latter of which is a bright MIPS 24 μm source and a VLA radio continuum source with a rather blue IRAC colour ([3.6 μm] − [4.5 μm] = −0.32). A higher resolution *K*-band image shows that the brighter radio peak is associated with a fainter component, suggesting this is a blended source. GS45b is 5.8 arcsec away from the LABOCA centroid, and it is a robust counterpart for both AzTEC and LABOCA sources (Biggs et al. 2011).

AzTEC/GS46. No radio source is found within the 13.0 arcsec search radius. The IRAC/MIPS source GS46a located 6.2 arcsec away from the AzTEC centroid is the tentative counterpart based on the combination of its red IRAC colour ([3.6 μm] − [4.5 μm] = +0.17; $P_{colour} = 0.255$) and MIPS 24 μm emission ($P_{24\,\mu m} = 0.226$). The LABOCA source LESS J033157.2−275633 ($S_{870\,\mu m} = 4.8 \pm 1.4$ mJy) is located 23 arcsec from GS46a and thus also far from the AzTEC centroid. We list the LABOCA flux in the table but note this large separation.

AzTEC/GS47. The faint VLA 1.4 GHz radio source GS47a ($S_{1.4} = 43.2 \pm 7.0$ μJy, $P_{1.4} = 0.105$) is found 7.6 arcsec away from the AzTEC centroid, and it is also a red IRAC source ([3.6 μm] − [4.5 μm] = +0.46) as well as a MIPS 24 μm source. The 870 μm LABOCA source LESS J033208.1−275818 ($S_{870\,\mu m} = 7.3 \pm 1.2$ mJy) coincides in position with AzTEC/GS47 within 3.4 arcsec of each other, making it a robust LABOCA counterpart as well (Biggs et al. 2011).

This paper has been typeset from a TeX/LaTeX file prepared by the author.